

COLLOIDAL DYNAMICS IN THE PRESENCE OF
OSCILLATORY ELECTROPHORETIC FORCES

EDWARD HAYDEN

Colloidal Dynamics In The Presence Of Oscillatory Electrophoretic Forces

by

© Edward Hayden

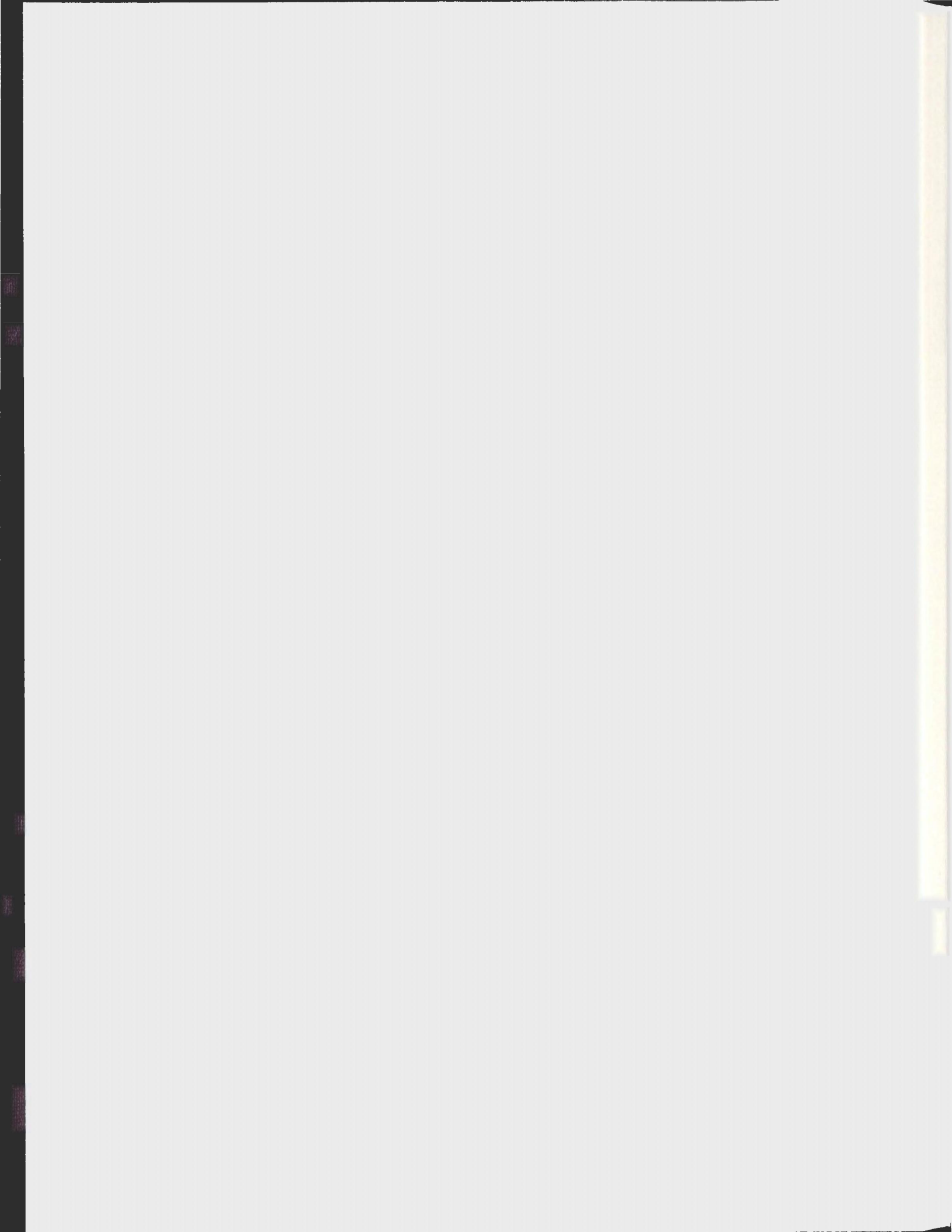
A thesis submitted to the
Department of Physics and Physical Oceanography
in partial fulfillment of the
requirements for the degree of
Master of Physics

Department of Physics and Physical Oceanography
Memorial University of Newfoundland

July 2013

St. John's

Newfoundland and Labrador



Abstract

The understanding of self-assembly and self-organization processes of colloidal particles are topics that in recently years have received greater attention in physics, in materials science, and in biology. Colloidal systems are often used as “big atoms” to study the fundamental physics of formation of crystals. In this thesis, electric fields at varying frequencies and amplitudes were applied to a charged colloidal system. Variation of the electric field amplitude will change the strength of the self-assembly and self-organization processes. At high frequencies and field strengths, the colloids experience a dipolar inter-particle interaction that will affect the equilibrium structure. At low frequencies, however, the colloids will experience both dipolar and non-equilibrium time-dependent electrophoretic forces.

The main purpose of this work was to explore this interplay between dipolar interactions and electrophoretic forces, and study how self-assembly and dynamics is affected by this interplay. From this study, we found a dynamical phase diagram that demonstrates the relationship between structure formation and particle dynamics as the frequency and field strength changes.

Acknowledgements

I would first and foremost like to thank my family for their support, constant encouragement, and for never saying that I can not do something, throughout my masters degree, for that I thank them. I would also like to thanks my friends for their assistance in both furthering of my procrastination skills and with helping me with my own work, for all of the interesting conversations we had, and for all the distractions they gave me throughout my Masters. I also would like to thank those who got me interested in physics and math, my high school physics teacher, Angelina Thornhill, and my high school math teacher, Rouse Brake. Without their patience and encouragement I would never had considered doing a Physics degree in the first place.

I would like to thank our entire research group for a good time, plenty of useful advice, answering all of my dumb questions, and giving me distractions when I needed them. Tyler Downey for helping me with some last minute image editing of high speed data, and for helping me manually track some particles for the tracking software, which was a FUN time. Corey Kelly for help with me with IDL assistance and for programming some clustering code.

And last but not least I would like to thank my supervisor, Dr. Anand Yethiraj. For his wealth of knowledge, for encouraging me, for introducing me to a field of physics I might have never known, for helping me with some last minute graphing and for his guidance and help on this project, which was monumental to completing it.

Contents

Abstract	ii
Acknowledgements	iii
List of Tables	ix
List of Figures	x
1 Introduction	1
1.1 Motivation for Study	1
1.2 Summary of Masters Work	3
1.3 Scope of Thesis	3
2 Background and Theory	5
2.1 Introduction	5
2.2 Colloidal Dispersions	5
2.3 The Reynolds Number	8
2.4 Brownian Motion	9
2.5 Stokes, Einstein and Sutherland	10

2.5.1	Stokes Law	10
2.5.2	The Stokes-Einstein-Sutherland Relation	10
2.5.3	Gravitational Height	12
2.5.4	Stokes Time	12
2.6	Bjerrum and Debye length	13
2.7	Rheometer	14
2.8	Mean Square Displacement and the Diffusion Coefficient	15
2.9	Anomalous Diffusion	16
2.10	Hydrodynamic Interactions	21
2.11	Faxén's Law	21
2.12	Induced Dipole Interactions	22
2.13	Attractive Forces	23
2.13.1	London-Van Der Waals Force	23
2.13.1.1	Hamaker Theory	23
2.14	Electro-kinetic Effects	25
2.14.1	Electrophoresis	25
2.14.2	Electro-osmosis	25
2.14.3	Dielectrophoresis	26
3	Experimental Methods	27
3.1	Introduction	27
3.2	Electrode Geometry and Electric Field Lines	27
3.3	Designs and Construction of Electric Field Cells	30
3.3.1	Electric Field sample Cell Design 1	30

3.3.2	The Zero Field Sample Cell	31
3.3.3	Electric Field Sample Cell Design 2	32
3.3.4	Electric Field Sample Cell Design 3	34
3.4	Filling the Electric Field Cell	35
3.4.1	Colloidal Suspension	35
3.5	The Control Hardware	37
3.5.1	Optical Microscopy	37
3.6	Particle Tracking Software	41
4	Results	45
4.1	Introduction	45
4.2	Viscosity Measurement	45
4.3	Stokes-Einstein-Sutherland Diffusion Coefficient	46
4.4	Colloidal Dynamics in Electric Fields	47
4.5	Sample EH01: Area Fraction $\alpha = 0.082$	48
4.5.1	EH01: Zero Field	48
4.5.2	EH01: $f = 250$ mHz	51
4.5.3	EH01: $f = 500$ mHz	56
4.5.4	EH01: $f = 1$ Hz	59
4.5.5	EH01: $f = 5$ Hz	61
4.5.6	EH01: $f = 10$ Hz	63
4.6	Sample EH02: Area Fraction $\alpha = 0.074$	66
4.6.1	EH02: Zero Field	66
4.6.2	Unwanted Particle Drift at High Voltages	71

4.6.3	EH02: $f = 250$ mHz	73
4.6.4	EH02: $f = 500$ mHz	75
4.6.5	EH02: $f = 1$ Hz	78
4.6.6	EH02: $f = 5$ Hz	81
4.6.7	EH02: $f = 10$ Hz	84
4.6.8	EH02: $f = 100$ Hz	88
5	Discussion and Conclusions	92
5.1	Introduction	92
5.2	Electrophoretic Mobility	92
5.3	Pair correlation functions at zero field for Samples EH01 and EH02	95
5.4	Dynamical Phase Diagram	97
5.4.1	Region I: Normal Diffusion	99
5.4.1.1	Stokes-Einstein-Sutherland Diffusion	100
5.4.2	Region II: Transition from Normal to Super-Diffusion	101
5.4.3	Region III: Transition from Sub-Diffusive to Super-Diffusive Behaviour	103
5.4.4	Region IV: Sub-Diffusive Behaviour	104
5.4.5	Region V: Anisotropic normal and sub-diffusive behaviours	104
5.4.6	Region VI: Sub-Diffusive Behaviour at Intermediate Times.	105
5.5	Conclusion	105
5.6	Future Work	107
	Bibliography	108

A Image Orientation Corrections	114
A.1 Results of Angle Measurements	117

List of Tables

2.1	Table of the types of colloidal systems that are encountered in everyday life (refer to section 2.2)	7
3.1	Refractive index (n), and density (ρ) of the solvents and colloids. . .	36
3.2	Table of Mean Displacements Corrected Equations	43

List of Figures

2.1	Schematic design for the cone and plate rheometer.	14
2.2	A sample sketch of the three types of diffusive behaviour. The red line shows super-diffusive behaviour with a slope, γ , equal to 2. The blue line shows normal-diffusive behaviour with γ equal to 1, and the purple line shows sub-diffusive behaviour with γ equal to $\frac{1}{2}$	17
2.3	Cartoons of the behaviour of $\log(\text{Mean square displacement})$ versus $\log(\text{time})$ for a system of particles in two circumstances. (a) This behaviour is often seen in molecular dynamics computer simulations where the short-time super diffusive behaviour is ballistic motion ($\gamma = 2$, red line) and there is normal diffusion at longer times ($\gamma = 1$, blue line). (b) The sequence shown often occurs in the case of diffusion in a crowded environment: normal diffusion at short times, caging at intermediate times (characterized by the purple line with $\gamma < 1$), and escape at longer times.	18

3.1	Schematic design of a field cell with electric field parallel to the substrate and perpendicular to gravity. The green colour denotes the bottom glass, yellow denotes the spacing electrodes, and cyan denotes the top plate. (Not drawn to scale.)	28
3.2	Electric vector fields for schematic design of a field cell with electric field parallel to the substrate and perpendicular to gravity. The blue colour is the glass slides, and green are the electrodes. The pink lines are the vector field lines and the red arrows are the electric vectors.	29
3.3	Design 1 for an electric field cell.	30
3.4	A Design for a cell which did not have electrodes within it but was used for studying dynamics at zero fields as well as for testing the tracking code used in this experimental work. The black lines are guide lines, and are only used in the placement of the capillary tube.	32
3.5	Design 2 for an electric field cell. The black lines are guide lines, and are only used in the placement of the electrodes and the capillary tube.	33
3.6	Design 3 for an Electric Field Cell. This design was used for the electric field experiments reported in this thesis	34
3.7	Experimental set-up for the applied AC electric field. A function generator output is connected to both one channel on a oscilloscope and to a wideband amplifier. The output of the amplifier is connected to both a second channel on the oscilloscope by a divide by 10 probe and to the sample cell	38
3.8	The Nikon Eclipse 80i C1+SHV confocal microscope with a Qimaging QICAM fast1394 12-bit monochrome camera (mounted on the rear port).	40

4.1	Stress versus strain relationship for solvent mixture at $T = 22^{\circ}\text{C}$ of 67.5% CHB (cyclohexyl bromide) and 32.5% decalin(decahydronaphthalene) used in the electric field studies. Shown also are the linear fits, and the viscosities fom the fitted slopes.	46
4.2	EH01, zero field. At zero field, the dynamics is diffusive: if one writes $MSD = t^{\gamma}$, then a linear fit to $\log(MSD)$ vs $\log(t)$ yields a slope $\gamma = 1.04 \pm 0.01$ consistent with $\gamma = 1$	49
4.3	(a) EH01, zero field. Pair correlation function shows a peak at $r/\sigma \sim 2$. The height of this peak is 1.4 indicating weak structuring.(b) EH01, zero field. Mean square displacement ($\langle X^2 \rangle$, $\langle Y^2 \rangle$) versus time is linear, and yields an experimental diffusion coefficient of $D_{NF}^{EH01} = 0.048 \pm 0.002\mu\text{m}^2/\text{s}$	50
4.4	(a) EH01, $f= 250\text{mHz}$ with voltages ranging from 7 to 60V. Results at each voltage are offset upwards from the previous voltage by 1 unit.(b) EH01, $f= 250\text{mHz}$ with voltages ranging from 7 to 60V, $\langle Y^2 \rangle$ data only. Results at each voltage are offset upwards from the previous voltage by 1 unit.	53
4.5	(a) EH01, $f= 250\text{mHz}$ with voltages ranging from 7 to 60V (or electric field amplitudes E_0 from 7 to 60 V/mm). The pair correlation function shows a peak at $r/\sigma \sim 4$. The height of this peak ranges from 1.4 to 4.0, indicating weak structuring at low fields but getting stronger at higher fields. (b) EH01, $f= 250\text{mHz}$. Montage of area from single frames of tracked data at 7V, 20V and 60V.	54

4.6	EH01, $f = 250\text{mHz}$ with 7V/mm . $\langle Y^2 \rangle$ versus time is linear, and yields an experimental diffusion coefficient of $D_{250\text{mHz}}^{EH01} = 0.043 \pm 0.001 \mu\text{m}^2/\text{s}$. The dynamics along the field direction, if analysed stroboscopically (looking only at the minima) is also diffusive with almost the same behaviour.	55
4.7	EH01, 500mHz at electric fields of 8 V/mm . The 8 V/mm results show normal behaviour in Y with weak oscillatory behaviour in X.	57
4.8	(a) EH01, $f = 500\text{mHz}$, $E_0 = 8$ and 30 V/mm . The pair correlation function shows a peak between $r/\sigma \sim 2$ for 4 V/mm , but shifts to $r/\sigma \sim 3.5$ for 30 V/mm . At the same time the peak height changes dramatically from about 1.4 to over 5 indicating a significant increase in structuring. (b) Frames from sample EH01 at 500mHz at 8 V and 30 V , showing the onset of chain formation and well-formed chains respectively.	58
4.9	EH01, $f = 500\text{mHz}$ with 8V/mm . $\langle y^2 \rangle$ versus time is linear, and yields an experimental diffusion coefficient of $D_{500\text{mHz}}^{EH01} = 0.0611 \pm 0.0003 \mu\text{m}^2/\text{s}$	59
4.10	EH01, 1Hz at electric fields of 10 V/mm . The results show linear behaviour in Y, with $\gamma = 0.8$, less than the $\gamma = 1$, normal diffusion behaviour.	60
4.11	EH01, 1Hz at electric fields of 10 V/mm . Pair correlation function shows a peak at $r/\sigma \sim 2$. The height of this peak is at 1.7, indicating weak structuring.	60

4.12	EH01, $f = 5\text{Hz}$, $E_0 = 16\text{ V/mm}$. $\langle Y^2 \rangle$ shows a single sub-diffusive behaviour at all times, while $\langle X^2 \rangle$ shows a transition from sub-diffusive behaviour at short times to somewhat less sub-diffusive behaviour at long times.	61
4.13	EH01, $f = 5\text{ Hz}$, $E_0 = 16\text{ V/mm}$. Pair correlation function shows a peak at $r/\sigma \sim 2$. The height of this peak is at 3.3, indicating that this peak correlates to the formation of chains. The existence of structuring is inferred from that fact that the first peak is around 3.2, with visible secondary and third peaks.	62
4.14	EH01, $f = 10\text{Hz}$ at electric fields of 17 and 30 V/mm. The 17 V/mm results exhibit sub-diffusive behaviour at all times with $\gamma = 0.8$. The 30 V/mm results (offset upward by 1 unit) show the $\langle Y^2 \rangle$ data exhibit sub-diffusive behaviour at all times while $\langle X^2 \rangle$ appears to have two linear regimes, at short times is sub-diffusive and at long times is super-diffusive.	64
4.15	(a) EH01, $f = 10\text{ Hz}$ at electric fields of 17 and 30 V/mm. Pair correlation function shows a peak at $r/\sigma \sim 2$. The height of this peak increases as field increase, indicating that the chain stiffness increases.(b) Frames from sample EH01 at 10Hz at 17 V and 30 V, showing the onset of chain formation and well-formed chains respectively.	65
4.16	EH02, zero field. At zero field, the dynamics is diffusive: if one writes $MSD = t^\gamma$, then a linear fit to $\log(MSD)$ vs $\log(t)$ yields a slope $\gamma = 1.004 \pm 0.002$ which is consistent with $\gamma = 1$. $\langle X^2 \rangle$ is offset by 0.25 for better visualization.	68

4.17	EH02, zero field. Pair correlation function shows no peak, indicative of fluid-like structure expected for dilute colloidal suspensions.	69
4.18	EH02, zero field. Mean square displacement ($\langle X^2 \rangle$, $\langle Y^2 \rangle$) versus time is linear, and yields an experimental diffusion coefficient of $D_{NF}^{EH02} = 0.0394 \pm 0.0002 \mu\text{m}^2/\text{s}$. $\langle X^2 \rangle$ is offset by 0.25.	70
4.19	The average of several frames sampled stroboscopically at the frequency of the applied field yields information about drift. Solid white circles are roughly static due to the stroboscopic sampling which renders the oscillatory motion invisible. Any left over drift manifests itself as a blurred particle track. This drift was observed to occur for experimental conditions (applied voltage and frequency) to the right of the red line.	72
4.20	EH02, 250 mHz at electric fields of 7 V/mm. The results show linear behaviour in Y	74
4.21	EH02, 250 mHz at electric fields of 7 V/mm. Pair correlation function shows no peak, indicating no structuring of colloids.	74
4.22	EH02, $f = 250\text{mHz}$ with 7V/mm . $\langle Y^2 \rangle$ versus time is linear, and yields an experimental diffusion coefficient of $D_{250\text{mHz}}^{EH02} = 0.039 \pm 0.0002 \mu\text{m}^2/\text{s}$	75
4.23	EH02, 500 mHz at electric fields of 7 and 30 V/mm. The results show linear behaviour in Y at 7 V/mm. . At 30 V/mm, the MSD appears to show a subtle $\gamma > 1$ behaviour.	76
4.24	EH02, 500 mHz at electric fields of 7 and 30 V/mm. Pair correlation function shows no peak, indicating no structuring of colloids.	77

4.25	EH02, $f = 500\text{mHz}$ with 7V/mm . $\langle Y^2 \rangle$ versus time is linear, and yields an experimental diffusion coefficient of $D_{500\text{mHz}}^{EH02} = 0.039 \pm 0.0001\mu\text{m}^2/\text{s}$	77
4.26	EH02, 1 Hz at electric fields ranging from 7 to 30 V/mm.	79
4.27	EH02, 1 Hz at electric fields ranging from 7 to 30 V/mm. $\langle Y^2 \rangle$ data only. Each voltage offset from the previous voltage by 0.25 unit. . . .	79
4.28	EH02, 1 Hz at electric fields ranging from 7 to 30 V/mm. Pair correlation function shows no peak at low voltages only at the highest voltage.	80
4.29	EH02, $f = 1\text{Hz}$ with 7V/mm . $\langle y^2 \rangle$ versus time is linear, and yields an experimental diffusion coefficient of $D_{1\text{Hz}}^{EH02} = 0.036 \pm 0.0001\mu\text{m}^2/\text{s}$	80
4.30	(a) EH02, 5 Hz at electric fields ranging from 7 to 70 V/mm. The dynamics along X shows oscillatory motion superimposed on diffusive dynamics at short times; this diffusive dynamics is seen for all times along Y. At high fields and long times, the motion along X is faster than diffusive.(b) EH02, 5 Hz at electric fields ranging from 7 to 70 V/mm. $\langle Y^2 \rangle$ data only. Each voltage offset from the previous voltage by 0.25 unit. The dynamics along $\langle Y^2 \rangle$ is seen to be diffusive at all field amplitudes.	82
4.31	(a) EH02, 5Hz with electric fields ranging from 7 to 70 V/mm. Pair correlation function shows a peak at $r/\sigma \sim 2$. The height of this peak is ranges from 1.2 to 1.9, indicating some structuring only at the highest field (70V/mm). (b) Frames from sample EH02 at 5Hz at 7 V and 70 V, showing the onset of chain formation and formed chains respectively.	83

4.32	EH02, $f = 5\text{Hz}$ with 7V/mm . $\langle Y^2 \rangle$ versus time is linear, and yields an experimental diffusion coefficient of $D_{5\text{Hz}}^{EH02} = 0.0332 \pm 0.0001\mu\text{m}^2/\text{s}$.	84
4.33	(a)EH02, 10 Hz at electric fields ranging from 7 to 100 V/mm . At these largest fields, and at long times, the dynamics is faster than diffusive along the field direction, and to a lesser extent, perpendicular to the field direction as well. (b) EH02, 10 Hz at electric fields ranging from 7 to 100 V/mm . $\langle Y^2 \rangle$ data only. Each voltage offset from the previous voltage by 0.25 unit. At short times, the dynamics is diffusive. At the largest fields, and at long times,the dynamics is faster than diffusive.	86
4.34	EH02, 10Hz with voltages ranging from 7 to 100 . Pair correlation function shows a peak at $r/\sigma \sim 2$. The height of this peak is ranges from 1.2 to 2.3 . indicating that is weak structure at the lower voltages but at the higher voltage there is much stronger structure.	87
4.35	EH02, $f = 10\text{Hz}$ with 7V/mm . $\langle y^2 \rangle$ versus time is linear, and yields an experimental diffusion coefficient of $D_{10\text{Hz}}^{EH02} = 0.035 \pm 0.0003\mu\text{m}^2/\text{s}$.	88
4.36	EH02. 100 Hz at electric fields ranging from 7 to 70 V/mm , shows simple diffusive behaviour both along and perpendicular to the field for all applied voltages.	89
4.37	(a) EH02, 100 Hz at electric fields ranging from 7 to 70 V/mm . Pair correlation function shows no peak, indicating no structuring of colloids. (b) EH02, $f= 100\text{Hz}$. Montage of area from single frames of tracked data at 7V , 30V and 70V . Shows no chainlike structures even at the highest fields.	90

4.38	EH02, $f = 100\text{Hz}$ with $7\text{V}/\text{mm}$. $\langle Y^2 \rangle$ versus time is linear, and yields an experimental diffusion coefficient of $D_{100\text{Hz}}^{EH02} = 0.038 \pm 0.0002\mu\text{m}^2/\text{s}$.	91
5.1	(a) Electrophoretic mobility for samples EH01 and EH02 for a range of frequencies ranging from 250mHz to 100Hz . (b) The small-amplitude electrophoretic response (shown for samples EH01 and EH02) showed no strong trend as a function of frequency. The average values reported are $3.7 \pm 0.1 \times 10^{-10}\text{m}^2/\text{Vs}$ and $5.9 \pm 0.1 \times 10^{-10}\text{m}^2/\text{Vs}$ respectively and compare with values ranging from 4.0×10^{-10} to $6.0 \times 10^{-10}\text{m}^2/\text{Vs}$ reported previously in a similar system [1]	94
5.2	Shown are 2D pair correlation functions corresponding to samples EH01 and EH02 (circle and square symbols, respectively, data for EH02 is shifted down by 1 unit for clarity) along with calculated pair correlations for the shown values of ionic concentration (c), particle charge(Q), and particle (area) fraction ϕ	95
5.3	(a)Sample EH01 image. Particle area fractions of $\alpha = 0.082$. (b) Sample EH02 image. Particle area fractions of $\alpha = 0.076$	96
5.4	Dynamical Phase Diagram for samples EH01 and EH02. This diagram shows normal diffusive behaviour at low field strengths for all frequencies and also at high frequencies for all field strengths studied. A range of anomalous diffusive behaviours are observed in the low frequency regime but at higher field strengths.	98

5.5	Montage of 5 frames about 0.8 seconds apart of a small region of tracked data of sample EH01. The red ellipses highlight particles undergoing normal diffusion behaviour due to Brownian motion.	99
5.6	Plot of the diffusion coefficient for Stokes-Einstein-Sutherland (black line), EH01 (blue squares), and EH02 (red circles)	100
5.7	Montage of 3 frames 10 seconds apart, of a small region of tracked data of sample EH02 at 5Hz, 70 V/mm. The purple circles highlight chains that are breaking and forming new chains.	102
5.8	Montage of 5 frames at 1 second apart, of a small region of tracked data of sample EH01 at 10Hz, 30 V/mm. The red circles highlight tracked particles in a chain that attaches to another chain.	103
5.9	Montage of 5 frames at .4 seconds apart, of a small region of tracked data of sample EH01 at 5Hz, 16 V/mm, highlighting particles within chains.	104
A.1	Samples figure for the rotation angle problem.	115
A.2	Plot of $\log(\text{MSD})$ vs $\log(\text{time})$, where all the data sets lie on top of the non-rotated data.	117

A.3 In principle, the electric field (E) should be parallel to \hat{x} , but could be rotated by a small amount. A test to determine the true direction of the E , by rotating the frame of reference. The data that was used was at a frequency of 250mHz at 20 voltages. The inserts in both (A),(B) are blown up areas of the black squares. The dotted lines corresponds to negative of the degrees. A) As the degree increases, MSD along x decreases. B) As the degree increases, MSD along y increases. 119

Chapter 1

Introduction

1.1 Motivation for Study

The understanding of self-assembly and self-organization processes of colloidal particles are topics that in recently years have received greater attention in physics, in materials science, and in biology [2, 3]. Colloidal systems are often used as “big atoms” to study the fundamental physics of formation of crystals [4]. The self assembly of colloidal systems also has potential materials science applications in producing inexpensive photonic crystals and as electrorheological fluids [5, 6]. Finally colloidal systems have been used as an analog for cluster formation in globular proteins [7].

The focus in many of these studies has been on when the system is in a equilibrium state. Self-assembly in a non-equilibrium system has received much less attention but it is nevertheless more relevant for many applications of colloidal systems [8, 9]. In the colloidal context, one simple example of an equilibrium system would be colloidal particles dispersed in a solvent, where the particles are continuously in motion due

to Brownian motion. Another example is that of dipolar colloidal particles in a suspension upon which is imposed a high-frequency AC (alternating current) electric field. This results in an inter-particle dipole-dipole interaction [10].

One example of non-equilibrium self assembly would be when there are time-dependent or time-independent body forces on the particles (two examples are gravity and electrophoresis) [9]. By studying these non-equilibrium systems, new and interesting phenomena might be observed which may lead to a better understanding of self-assembly and self-organization processes of colloidal particles.

In this thesis, electric fields at varying frequencies and amplitudes will be applied to a colloidal system (refer to 3.4.1 for more detail on the colloidal suspension used). Variation of the electric field amplitude will change the strength of the self-assembly and self-organization processes. At low electric field the forces will be weak, and at higher electric field the forces should be strong. In a high-frequency AC electric field, the dipolar interactions can be considered to be time-averaged, which results in time-independent inter-particle forces that are derivable from a potential. As a result of this, these inter-particle forces are considered to simply modify the inter-particle interactions in an equilibrium colloidal system. On the other hand, the electrophoretic forces, which can occur in either direct current (DC) or low-frequency AC electric fields, are regarded to be time-dependent forces. Thus these forces may be considered truly non-equilibrium.

The main purpose of this work will be to explore this interplay between dipolar interactions and electrophoretic forces, and study how self-assembly is affected by this interplay. A colloidal model system where one can explore the interplay between equilibrium and non-equilibrium forces is also potentially useful because it could help

shed light on complex problems such as dynamics in glass-forming systems.

1.2 Summary of Masters Work

In this work, there will be an application of a linear external AC electric fields at varying frequencies and varying voltages to a electric field cell. Within this electric field cell, particles will be suspended of a specified shape with the electrodes in a certain orientation. The behaviour of the particles will be observed by a camera as the electric field is changed.

1.3 Scope of Thesis

Chapter 1 has introduced the motivation behind the research done for this thesis. This chapter also contains the scope of the thesis.

Chapter 2 outlines some of the theory relating to dynamics (flow and diffusion) in colloidal suspensions, interaction forces in colloids, the effects of surfaces, and finally, the effect of external electric fields.

Chapter 3 presents the experimental set-up and the electric field cell design. In addition, the preparation of the colloidal suspension, as well as a description of the image acquisition and image processing techniques used, will be presented.

Chapter 4 presents results from the electric field experiments; as well as the results from the rheometer for finding the viscosity of the solvent.

Chapter 5 discusses the results of this research. This chapter will also contain the conclusion of the thesis and suggests some future ideas for this research.

In Appendix A there is the discussion on how angled electrodes are handled with a sample data set.

Chapter 2

Background and Theory

2.1 Introduction

This chapter will define what colloids are and outline some of the theory relating to dynamics (flow and diffusion) in colloidal suspensions. Also interaction forces in colloids, the effects of surfaces, and finally, the effect of external electric fields will be discussed.

2.2 Colloidal Dispersions

One important area of study in soft condensed matter involves the study of structure formation in colloidal suspensions. One of the main reasons for this is that colloidal suspensions can be thought of as a micrometer-scale model system for atoms [4]. Also the structure formation of colloidal suspensions is analogous to thermodynamic phase transitions in atomic systems [4, 5].

A colloidal dispersion is a mixture in which particles of one species are dispersed

throughout a second medium [9]. If the particles are evenly dispersed throughout the medium then it is considered to be a stable colloidal system. The typical size of colloidal particles ranges from tens of nanometers to a few micrometers in diameter. Although colloidal particles in nature tend to be very irregularly shaped objects and are also very polydisperse in size, it is very useful in experimental studies to have simple well-defined shapes and narrow size distributions. The most common colloid shape that is used for scientific purposes are spherical colloids but shapes such as rod-like, disk-like and plate-like are also studied (section 1.4 of [9]). For example, bentonite clay, found in western Canada is a natural source of plate-like colloidal particles (section 1.4.5 of [9]).

Over the years, a combination of advanced optical microscopy techniques [11], as well as image processing methods have been created in connection to the study of structure formation in colloidal suspensions. These advances have helped in getting a better understanding of structure formation in suspensions. Also, techniques have been developed to synthesize fluorescent-labelled colloidal spheres that enable the acquisition of images in three dimensions with the possibility of single-particle tracking [12, 13].

Attractive forces within the medium, such as van der Waals forces, can cause the particles within the colloidal suspensions to aggregate, while other forces such as repulsive electrostatic inter-particle forces tend to stabilize the suspensions. This type of stabilization is known as charge stabilization [9]. In addition, particles with polymer chains attached to their surface prevent other particles from approaching close to them. This is known as steric stabilization. Both charge and steric stabilization help keep colloidal particles suspended in a solvent. However, over time, even stable

colloidal particles will sediment under the influence of gravity. For many of these colloidal dispersions the stability or phase behaviour can be altered dramatically by modest changes in the composition of the dispersion [14].

Colloidal dispersions can be divided into two classes [9]. The first class is referred to as lyophilic which is solvent loving. The other class is referred to as lyophobic which is solvent hating. The classification can be made from the ease with which the system can be re-dispersed if it is allowed to dry out (section 1.3 of [9]).

Table 2.1 shows some examples of colloidal systems that are used in everyday life and the technical name of each colloidal dispersion (section 1.1 of [9]).

Table 2.1: Table of the types of colloidal systems that are encountered in everyday life (refer to section 2.2)

Disperse Phase	Solvent	Notation	Technical Name	Example
Solid	Gas	S/G	Aerosol	Smoke
Liquid	Gas	L/G	Aerosol	Fog
Solid	Liquid	S/L	Dispersion	Ink, Paint
Liquid	Liquid	L/L	Emulsion	Milk
Gas	Solid	G/S	Foam	Fire-extinguisher foam
Solid	Solid	S/S	Solid Dispersion	Ruby Glass
Liquid	Solid	L/S	Solid Emulsion	Ice Cream
Gas	Solid	G/S	Solid Foam	Insulating foam

2.3 The Reynolds Number

In the year 1851 physicist George Gabriel Stokes introduced the concept of a number which would describe the amount of turbulence within a fluid flow [9]. But it was not until around the year 1883 when physicist Osborne Reynolds (whom the number was named after) popularized its use [9, 15]. The concept of the Reynolds number allows fluid flow to be easily classified as laminar (absolutely steady flow) or turbulent (flow with unsteady fluctuations) [9].

Under this classification of flows, any flow with a Reynolds number less than 2,300 is laminar, while flow with values above 4,000 are turbulent [15]. The range between these two regions is considered to be the transition region. The Reynolds number (Re) can be defined as:

$$Re = \frac{\rho va}{\eta} \quad (2.1)$$

where ρ is the density of the solvent, v is the velocity of the relevant object, with a radius a , and η is the viscosity of the solvent.

The colloidal particles used in this thesis are 2 μm diameter PMMA (poly(methyl methacrylate)) colloids, in a solvent medium consisting of CHB (cyclohexyl bromide) and decalin (decahydronaphthalene) (refer to section 3.4.1 for more details). This solvent mixture is special in that it can be used to match the density and the refractive index of the particles. The density of the solvent is 1184.9 kg/m^3 , with a viscosity of 2.11 $\text{mPa} \cdot \text{s}$. Putting this value into equation 2.1 we get:

$$Re = \frac{(1184.9 \text{ kg}/\text{m}^3)(1 \times 10^{-6} \text{ m})v}{2.11 \times 10^{-3} \text{ Pa} \cdot \text{s}} = 0.561 v \quad (2.2)$$

For colloidal speeds ranging from $1 \mu/s$ (which is physically relevant) to $100 \mu/s$ (which is larger than any likely colloidal motion) the Reynolds number ranges from 5.6×10^{-7} to 5.6×10^{-5} . Thus the fluid flow within the cell should always be laminar.

2.4 Brownian Motion

Around the year 1827 a well-known botanist, Robert Brown, was studying the sexual reproduction of plants [16]. In particular he was interested in the particles that were contained in grains of pollen. He found that the pollen grains were filled with oblong granules about 5 microns long and that these granules seem to be in a constant “jittery” motion. After seeing this a few times, he then repeated the experiment using particles of dust instead of the oblong granules, and thus was able to rule out that the motion was caused because the pollen particles were ‘alive’, although he could not explain the motion that both the oblong granules and the particles of dust had undergone [16]. It was not till around 1905 that both Albert Einstein and William Sutherland, independently of each other, proposed the theory that still used today for this constant jittery random motion of objects in a fluid that Robert Brown saw [17, 18].

Specifically, Albert Einstein predicted that this constant jittery random motion of a particle in a fluid at a thermodynamic temperature T is characterized by the thermal excitation of the solvent molecules [15]. This thermal excitation makes them continually collide with any objects in their vicinity causing this random motion with an associated energy on the order of $\sim k_B T$ (where k_B is Boltzmann’s constant). This constant jittery random motion is known as Brownian motion. It becomes quite

noticeable as we examine increasingly smaller and smaller systems. Because the motion is a result of the thermal excitation of the solvent molecules, it is unavoidable at all non-zero temperatures.

2.5 Stokes, Einstein and Sutherland

2.5.1 Stokes Law

In 1851, George Gabriel Stokes derived an expression, now known as Stokes' law, for the frictional drag (resistance) exerted on spherical objects with very small particles (in other words, very small Reynolds numbers) in a continuous viscous fluid. This expression can be written as (section 4.8.1 of [9]):

$$F_N = bv = 6\pi\eta av \quad (2.3)$$

Here F_N is the frictional drag (resistance), b is the linear drag coefficient on the particle, η is the fluid viscosity, a is the radius of the spherical object, and v is the particle's velocity.

Thus by measuring the force and the velocity, and knowing the size of the sphere, Stokes' law can be used to calculate the viscosity of the fluid (section 4.8.1 of [9]).

2.5.2 The Stokes-Einstein-Sutherland Relation

The equilibrium thermal excitation of colloidal particles in a solution is directly related to the local time dependent friction drag (resistance) and thus to the linear viscous properties of the surrounding fluid [19]. The relation that relates these thermal

fluctuations to the (Stokesian) viscous drag for spherical colloidal particles is due to Einstein [17] and Sutherland [18] and may be written as:

$$D = \frac{k_B T}{b} = \frac{k_B T}{6\pi\eta a} \quad (2.4)$$

Here D is the colloid diffusivity, b is the linear drag coefficient on the particle, η is the viscosity, and a is the radius of a colloid [19].

This relationship is valid for equilibrium thermal excitation of a Newtonian fluid [9]. However it has been shown theoretically and experimentally that this relation can be generalized to treat non-Newtonian materials, as well as materials that are not in equilibrium [15]. Within this generalization, the viscosity of the surrounding Newtonian fluid is replaced by the complex viscosity of a surrounding viscoelastic soft material. The limits and the validity of this generalization are however open questions [19].

In certain cases this unstoppable motion of the object of interest can cause practical difficulties [9, 15]. For example, a common issue in microscopy is particles diffusing from the field of view or out of the plane of focus. If one wishes to get a high resolution images of a particle, one has to maximize the image relative to the field of view, but in doing so one minimizes the amount of time it can be imaged before disappearing from one's field of view, thereby setting an upper limit on time scales. One must therefore strike a balance between the quality of data collected and time range over which we collect data.

2.5.3 Gravitational Height

In this work, the entire colloidal sediment was confined to a single layer, effectively a two dimensional plane near the top surface of this three dimensional system. This assumption could be made assuming that most particles have risen due to the mismatch in densities.

One can define a gravitational height:

$$h_{grav} = \frac{k_B T}{\frac{4}{3}\pi a^3 \Delta\rho g} \quad (2.5)$$

where g is the gravitational acceleration, a is the particle radius, $\Delta\rho$ is the density mismatch between the particles and the fluid, T is the temperature of the solution, and k_B is the Boltzmann constant.

Now from section 3.4.1 the $\Delta\rho$ is $0.05 \frac{\text{g}}{\text{cm}^3}$, and the temperature is taken to be 294K. Then from equation 2.5, $h_{grav} = 1.976 * 10^{-6}\text{m}$. Thus,

$$\frac{h_{grav}}{2a} = \frac{1.976 \times 10^{-6}\text{m}}{2(1 \times 10^{-6}\text{m})} = 0.988 \sim 1 \quad (2.6)$$

This implies that at steady state after sedimentation has taken place, most colloids will be within 1 particle diameter of the lowest energy state at the top of the electric field cell. Therefore the system is at least quasi-two-dimensional.

2.5.4 Stokes Time

Another consideration is how long one must wait for the system to reach this quasi-two-dimensional state.

Solving equation 2.3 for the velocity,

$$v_s = \frac{f_N}{6\pi\eta a} = \frac{2\Delta\rho a^2 g}{9\eta} \quad (2.7)$$

where v_s is the Stokes velocity, and has the value

$$v_s = 4.54 \times 10^{-8} \text{ m/s} \quad (2.8)$$

Now from this Stokes velocity we can find a Stokes time, a time which it would take for the particles to sediment. This time is equal to:

$$T_s = \frac{l}{v_s} \quad (2.9)$$

where l is the length from middle of the sample to the top or bottom plate (around $50 \mu\text{m}$). Thus, $T_s = 18.65$ minutes. In our experience, after the experiment was set-up, we needed to wait 15 minutes for the particle density profile to reach a steady state, with most particles close to the top electrode.

2.6 Bjerrum and Debye length

The Debye length is a parameter that is often used in the study of plasmas or electrolytes. This parameter is a measurement of how far the electrostatic effects persist within a fluid [20]. The Bjerrum length is a distance at which the electrostatic effect between two particles compares to the thermal energy [20]. The Bjerrum length is:

$$\ell_B = e^2 / (4\pi\epsilon\epsilon_0 k_B T) \quad (2.10)$$

For the dielectric constant of the solvent used in our experiments ($\epsilon = 6.05$ from a

linear combination of cyclohexyl bromide (CHB) and decalin (decahydronaphthalene), dielectric constants from [21]) $\ell_B = 103 \pm 10\% \text{\AA}$.

2.7 Rheometer

A rheometer is a device that measures the visco-elastic properties of fluids. In this thesis, we will vary the rate of shear deformation, known as the shear rate $\dot{\gamma}$, and measure the resulting shear stress σ . For a simple Newtonian liquid, the shear stress is proportional to the shear rate:

$$\sigma = \eta \dot{\gamma} \quad (2.11)$$

where η is the viscosity of the fluid. For our measurements, we use a cone and plate rheometer. Figure 2.1 shows a schematic design of the cone and plate rheometer.

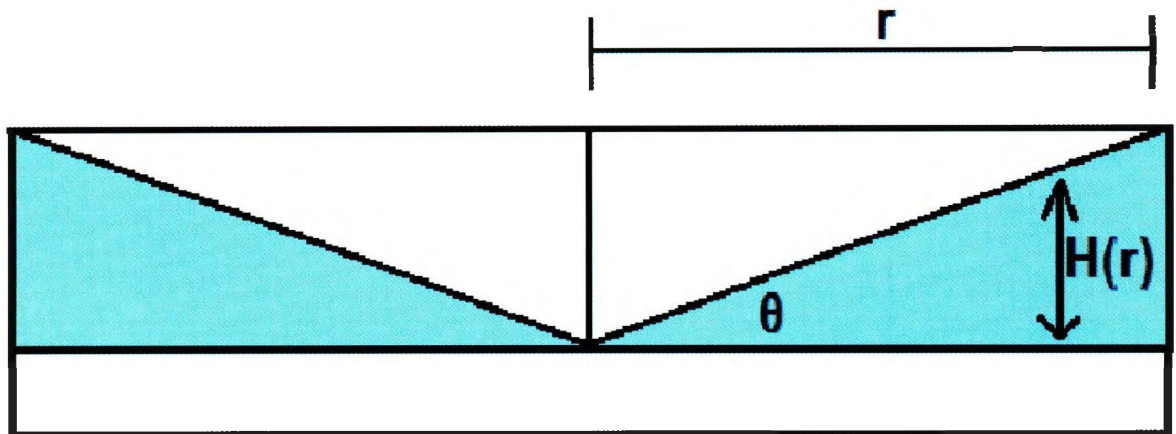


Figure 2.1: Schematic design for the cone and plate rheometer.

This type of rheometer geometry is a clever design to ensure that the shear rate

($\dot{\gamma} = H(r)/v(r)$, where r is the radius of the cone, and $H(r)$ is the height at a distance r from the tip of the cone) is constant throughout the cell.

2.8 Mean Square Displacement and the Diffusion Coefficient

The mean squared displacement (MSD) is the most common measure of Brownian motion in colloids ([22], [9], section 4.9.2). Albert Einstein and Marian Smoluchowski made this connection independently of each other in their papers on Brownian motion in 1905-1906. An equation relating this became known as the Einstein-Smoluchowski equation. The mean squared displacement of an isolated spherical particle in one dimension is ([9], section 1.5.4):

$$MSD = \langle (x(t) - x(0))^2 \rangle = 2 \left(\frac{k_B T}{b} \right) t = 2Dt \quad (2.12)$$

where k_B is Boltzmann's constant and b is the linear drag coefficient on the particle, t is the time, and D is the diffusion coefficient of the particle (refer to section 2.5.2) ([9], section 1.5.4).

Thus, in a plot of MSD versus *time*, the slope of the line will be equal to two times the diffusion coefficient. When $MSD \propto t$, the dynamics is said to be diffusive, because of the slope yields the diffusion coefficient. It is often useful to take the logarithm of both the MSD and time, thus equation 2.12 becomes:

$$\log(MSD) = \log(2Dt) \quad (2.13)$$

$$\log(MSD) = \log(2D) + \log(t) \quad (2.14)$$

Thus for a plot of $\log(MSD)$ versus $\log(t)$, the slope of the line should be equal to one for normal diffusion, with the y-intercept equal to $\log(2D)$. If the slope of the $\log(MSD)$ versus $\log(t)$ plot is not equal to one then the diffusion can be considered to be anomalous.

2.9 Anomalous Diffusion

One could generalize diffusion and write that the $MSD \sim t^\gamma$ [9]. Thus, when the slope (γ) of a plot of $\log(MSD)$ versus $\log(t)$ is less than one, then the dynamics is considered to be sub-diffusive. When γ is greater than 1, then the diffusion is termed as super-diffusive. A trivial cause for γ greater than 2 is ballistic motion at very short times. This is often seen in molecular dynamics computer simulations, where there is no solvent [23].

In these simulations, the diffusive regime arises after several collisions with other colloidal particles. This ballistic regime is not seen in colloidal experiments, where there is a viscous solvent and the particles undergo Brownian motion [23].

Apart from ballistic motion, deviations from simple diffusion are characteristic of systems exhibiting glassy behaviour [3, 24]. To get a better idea of three types of dynamics in a $\log(MSD)$ versus $\log(t)$ plot, a sample plot with the three types is shown in figure 2.2. Within this figure, the red line shows super-diffusive behaviour with a slope equal to 2. The blue line shows normal-diffusive behaviour with a slope equal to 1. And the purple line shows sub-diffusive behaviour with a slope equal to

half.

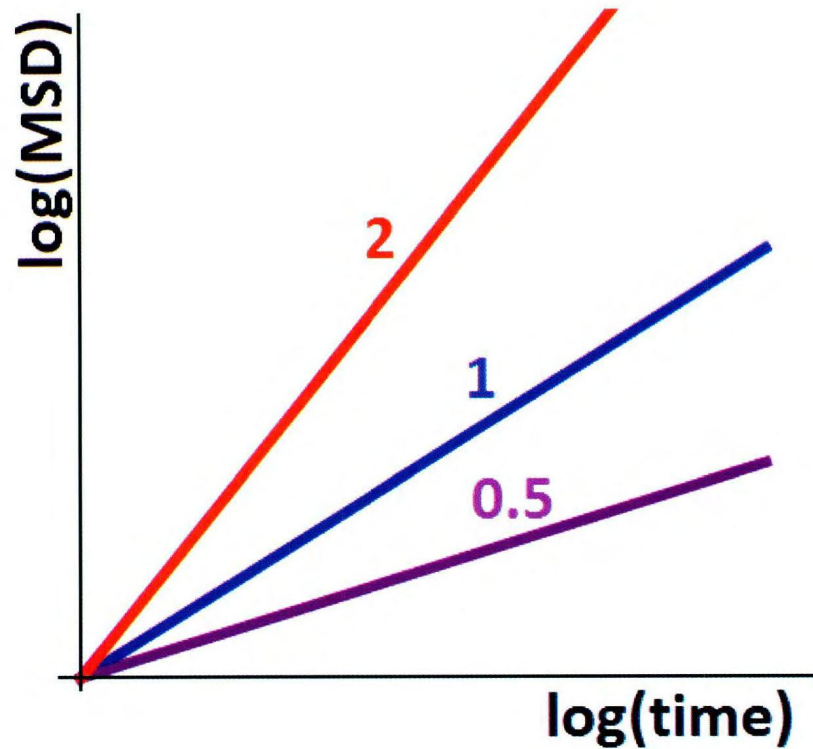
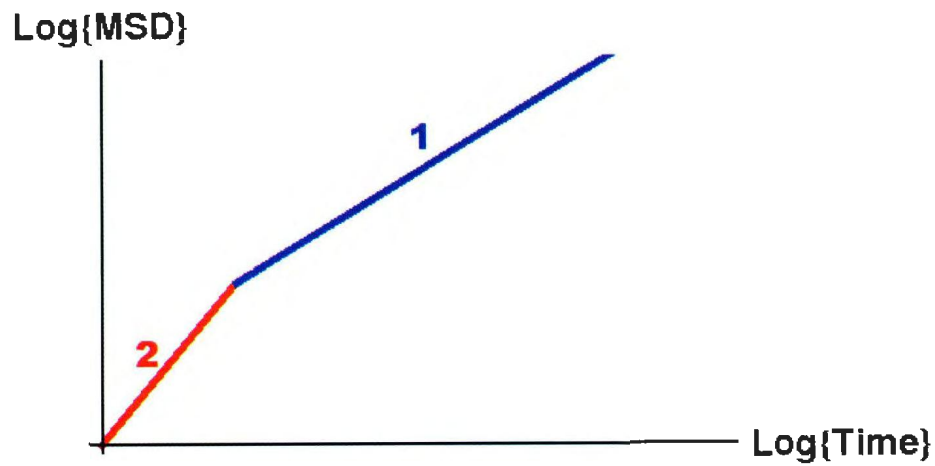
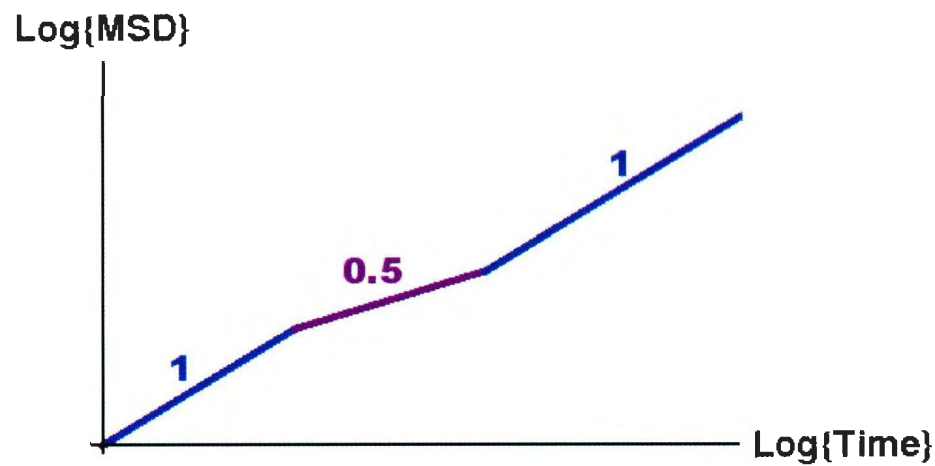


Figure 2.2: A sample sketch of the three types of diffusive behaviour. The red line shows super-diffusive behaviour with a slope, γ , equal to 2. The blue line shows normal-diffusive behaviour with γ equal to 1, and the purple line shows sub-diffusive behaviour with γ equal to $\frac{1}{2}$.

Figure 2.3 shows an schematic cartoons of the behaviour of $\log(\text{MSD})$ versus $\log(\text{time})$ for a system of particles in two circumstances. Figure 2.3(a) shows an schematic cartoon of a system of particles undergoing behaviour that is often seen in molecular dynamics computer simulations where the short-time super diffusive behaviour is ballistic motion (slope = 2, red line) and there is normal diffusion at longer times (slope = 1, blue line). Figure 2.3(b) shows an schematic cartoon of a



(a)



(b)

Figure 2.3: Cartoons of the behaviour of $\log(\text{Mean square displacement})$ versus $\log(\text{time})$ for a system of particles in two circumstances. (a) This behaviour is often seen in molecular dynamics computer simulations where the short-time super diffusive behaviour is ballistic motion ($\gamma = 2$, red line) and there is normal diffusion at longer times ($\gamma = 1$, blue line). (b) The sequence shown often occurs in the case of diffusion in a crowded environment: normal diffusion at short times, caging at intermediate times (characterized by the purple line with $\gamma < 1$), and escape at longer times.

sequence that often occurs in the case of diffusion in a crowded environment: normal diffusion at short times, caging at intermediate times (characterized by the purple line with slope less than 1) , and escape at longer times.

Most studies of colloidal self assembly have focused on equilibrium behaviour. But some work has been done in recent years in the non-equilibrium state. Hunter et al [3] review the current status in the field of glassy colloidal systems, while the study of colloidal systems in the presence of external forces has been reviewed by Lowen et al [25] and Yethiraj et al [26]. Fraden et al [27] showed early on that colloidal particles in an electric field form stable clusters along the electric field lines. Enhanced dynamics has also been seen in anisotropic rod-like colloidal systems (Höfling et al [28]). The work found that the evolution of the average cluster size agrees with the Smoluchowski equation and that at short times the colloidal clusters grow in length linearly.

A recent study on a steady state system was carried out by Jordanovic et al [23]. In this work, the researchers used molecular dynamics simulations to investigate the translational dynamics of particles with dipolar interactions in homogenous external fields. This research investigated the motion parallel and perpendicular to the field for a broad range of parameters, such as different concentrations, dipolar coupling strengths and field strengths. Graphs of the logarithm of the mean square displacement (MSD) versus the logarithm of the time for computer simulations of a reduced density colloidal suspension were obtained for both moderate and strong dipolar coupling parameters (λ). These two cases showed that for short periods of time (less than one second), there was an initial ballistic regime where the displacement increases linearly with time. Thus the $\log(MSD)$ versus $\log(t)$ plot has $\gamma = 2$. Also

for both cases they observed that for longer time-scales (greater than 10 seconds), there is a diffusive ($\gamma = 1$) regime. For this intermediate time, moderate and strong couplings show different behaviours. For moderate coupling parameters ($\lambda = 3$) the ballistic regime directly goes into the diffusive regime (as shown in the schematic graph, figure 2.3(b)). For strongly coupled parameters the ballistic regime goes into a sub-diffusive regime (i.e. $\gamma < 1$) before the dynamics becomes diffusive again at long times.

The same work also examines dynamics for higher-density colloidal suspensions with strong dipolar coupling parameters. The diffusive regime in molecular dynamics is reached after the particles have undergone numerous collisions with other particles. It was also found that as the densities increase the sub-diffusive regime increased in size.

This study found for the first time, from molecular dynamics simulations, that the formation of chain-like clusters in the presence of an external electric field coincides with a crossover from normal to anomalous dynamics as the field strength increases. The anomalous dynamics involves sub-diffusion, directed motion and dynamic heterogeneities.

In addition, the work done by Jäger et al [29] focused on computer simulation studies of a monolayers of particles with permanent dipole moments that are driven by rotating external fields. This was motivated by experimental work studying layer formation in rotating fields [30]. Both simulation and experiment found that the particles in such systems self-organize into two-dimensional clusters. Also investigated were the field strengths and frequencies at which clusters formed, and the influence that hydrodynamic interactions had on the clusters.

2.10 Hydrodynamic Interactions

Diffusion according to the Stokes-Einstein-Sutherland relation assumes that particles are at low enough concentrations that each particle can be considered to be isolated. However, this is rarely the case in real colloidal suspensions.

When a particle immersed in a fluid moves, it exerts a force on the solvent which changes the fluid flow around it from its undisturbed value. The disturbance to the fluid, in turn, changes the viscous drag force exerted on the other particles in the colloidal suspension. Similarly, the other particles can also cause a disturbance. By generating and reacting to a fluid's local velocity, colloidal particles experience "hydrodynamic interactions" with each other. Despite their importance being long recognized, the effects of hydrodynamic interactions on collective behaviour is a complex many-particle problem and as a result often too difficult to treat properly ([9], section 4.8.2).

2.11 Faxén's Law

In 1922, the physicist Hilding Faxén introduced a correction to Stokes law for the friction on spherical objects in a viscous fluid, which would be valid where the object moves close to a wall of the container. In the presence of a spatially varying flow, but in the absence of any other external force, Faxén's law takes the form:

$$v = u(r) + \frac{1}{6}a^2 \nabla^2 u(r) \quad (2.15)$$

In the above equation, v is the sphere's velocity, $u(r)$ is the disturbance velocity

(the local fluid velocity), and a is the radius of the sphere. [14]

Faxén's laws can be used to predict the near-wall in-plane hindered coefficient (D_H) as:

$$\frac{D_H}{D} = [1 - \frac{9}{16}\delta + \frac{\delta^3}{8} - \frac{45}{256}\delta^4 + \dots] \text{ where } \delta = \frac{a}{H+a} \quad (2.16)$$

In the above, a is the radius of the colloidal particle, D is the bulk diffusion coefficient and H is the distance from the surface [31].

2.12 Induced Dipole Interactions

Induced dipole forces result when a ion, a dipole, or a molecule with a induced dipole, induces a dipole in an atom or a molecule with no dipole. There are two types of induced dipole interaction.

First there is the ion-induced dipole force, which is a weak attraction that results when the approach of an ion induces a dipole in an atom or in a nonpolar molecule by disturbing the arrangement of electrons in the nonpolar species.

Second, the dipole-induced dipole force is a weak attraction that results when a polar molecule (or a non-polar molecule which has a temporary dipole) induces a dipole in an atom or in a nonpolar molecule by disturbing the arrangement of electrons in the nonpolar species. This dipole-induced dipole forces can also be the result of a electric field disturbing the arrangement of electrons on an atom or in a nonpolar molecule thus inducing a dipole.

2.13 Attractive Forces

Colloidal particles within a solvent have a strong tendency to aggregate into large clusters, which may be compact or fractal-like in nature. This occurs under the influence of universal attractive forces which become increasingly potent as the particles size become larger [22].

2.13.1 London-Van Der Waals Force

One of the main forces that is included within this universal attractive force is the van der Waals force or the induced-dipole interaction. This force was first postulated by the physicist Johannes van der Waals in 1827 (section 11.2 of [9]). This force exists between all atoms and molecules and does not depend on whether they are electrically charged or not. This force is a results from the fluctuating of atomic and molecular electrical dipoles [22].

In 1930, physicist Fritz London was the first to recognize that this force could also be the result of the interaction between a temporary induced dipole on one molecule and the induced dipole on a neighbouring molecule. This type of van der Waals force is referred to as the London-Van der Waals force [22] ([9], section 11.2).

2.13.1.1 Hamaker Theory

Following Fritz London's explanation of the origins of van der Waals forces, Hamaker in 1937 was quick to realize that such universal long-range intermolecular forces could give rise to the long-range attractive forces between macroscopic objects that must be invoked to explain the phenomenon of colloid aggregation ([9], section 11.3).

The van der Waals interaction energy V_A has been solved for a few known geometries ([9], section 11.3). For two spherical colloidal particles separated by distance H , where H is the shortest surface to surface distance between the spheres, the interaction potential is:

$$V_A = \frac{-A}{6H} \left(\frac{a_1 a_2}{a_1 + a_2} \right), \text{ where } a_1, a_2 \gg H \quad (2.17)$$

with A as the Hamaker constant (a typical Hamaker coefficient for metal is around $30 kT_{room}$ (table LI.3 of [32])), a_1 and a_2 are the radii of the two spheres.

Now looking at equation 2.17, it is clear that if the particles are of the same size ($a_1 = a_2 = a$) then this simplifies to:

$$V_A = \frac{-Aa}{12H} \quad (2.18)$$

from this equation we can see that if the particle size is on the order of the distance between them, then the van der Waals interaction energy is about 12 times smaller than the Hamaker constant. But if $\frac{a}{12H} \sim 1$, then the van der Waals interaction energy is equal to the Hamaker constant.

For a spherical colloid next to a flat surface, [9]:

$$V_A = \frac{-Aa}{6H} \left(1 + \left(\frac{H}{2(a) + H} \right) + \dots \right), \text{ where } a \gg H \quad (2.19)$$

where a is the radius of the sphere, and H is the distance between the sphere and the flat surface.

Van der Waals forces are implicated in the uncontrolled aggregation of colloidal spheres to each other and to the sample cell surfaces [9], so these forces are always somewhat relevant.

2.14 Electro-kinetic Effects

We cannot neglect the effect of electrical charges that are inevitably present at the particle surface and in the surrounding liquid when a electric field is applied to the cell. There are many dynamical effects that happen within the sample cell when a electric field is applied. But the three main mechanisms for electric-field effects are electrophoresis, dielectrophoresis and electro-osmosis [9]. These mechanisms will be discussed in the following subsections.

2.14.1 Electrophoresis

Electrophoresis is the motion of dispersed particles relative to a fluid under the influence of a uniform electric field. Experimentally it was found that the particle velocity is proportional to the applied field strength. For spherical particles this relationship is, $u = \mu_E E$, where μ_E is the electrophoresis mobility of the particle. It is caused by the presence of a charged interface between the particle surface and the surrounding fluid ([9], section 8.2.3).

2.14.2 Electro-osmosis

Electro-osmosis is the motion of liquid induced by an applied electric field across capillaries or microchannels. Like electrophoresis, the velocity of this motion is also linearly proportional to the applied electric field, and dependent on both the material used to construct the microchannel and the solution in contact with the channel wall. The role of electro-osmosis is more dominant in highly polar solvents ([9], section 8.2.1). In this work, we used less polar solvents to minimize electro-osmotic flows.

2.14.3 Dielectrophoresis

Dielectrophoresis is a phenomenon in which a force is exerted on a dielectric particle when it is subjected to a non-uniform electric field. In contrast to linear electrophoresis, it does not require that the object have a net charge. All particles exhibit dielectrophoretic activity in the presence of non-uniform electric fields. However, the strength of the force depends strongly on the medium and particles' dielectric constants, on the particles' shape and size, as well as on the frequency of the electric field (section 8.9 of [9]).

Chapter 3

Experimental Methods

3.1 Introduction

The experiments described in this thesis involve electric-field-driven oscillatory motion of colloidal particles in suspension. Electric fields of varying amplitudes and frequencies were employed. This chapter will focus on the details of the electric field cell design and construction. This chapter will also address the experimental hardware used to carry out the experiments within this thesis. Finally this chapter will discuss the image acquisition methods, and the image processing software used to analyse the images acquired.

3.2 Electrode Geometry and Electric Field Lines

Figure 3.1 shows a schematic design of an electric field sample cell with electric field parallel to the substrate and perpendicular to gravity. In the figure, the green colour denotes the bottom glass, yellow denotes the spacing electrodes, and cyan denotes

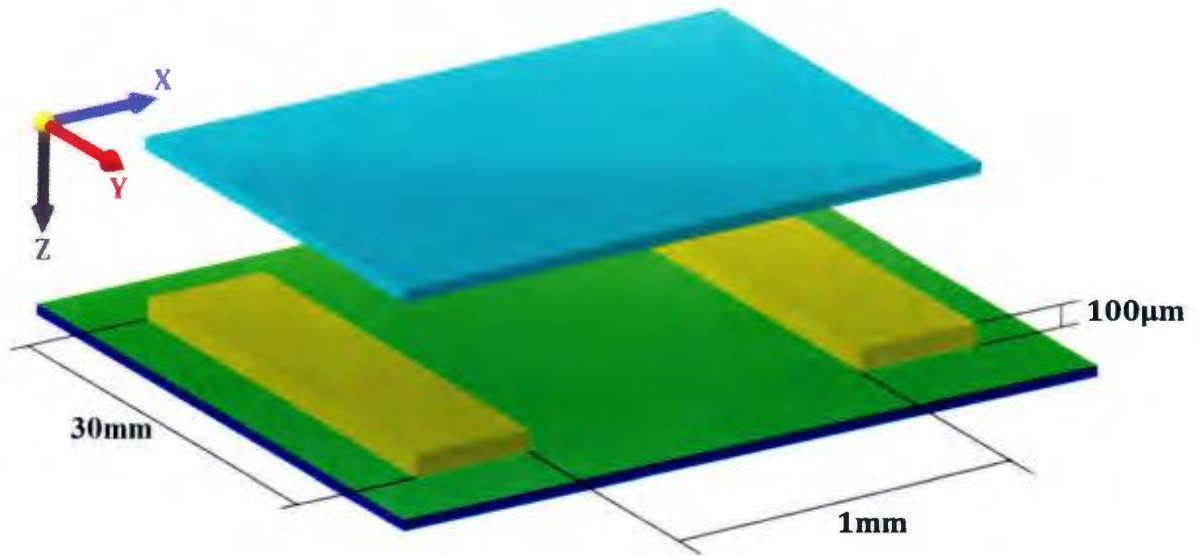


Figure 3.1: Schematic design of a field cell with electric field parallel to the substrate and perpendicular to gravity. The green colour denotes the bottom glass, yellow denotes the spacing electrodes, and cyan denotes the top plate. (Not drawn to scale.)

the top plate.

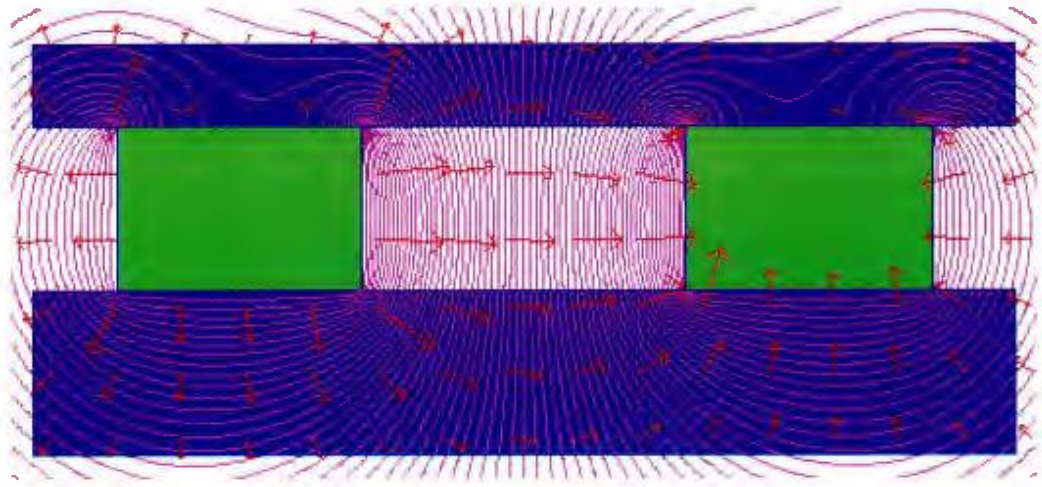


Figure 3.2: Electric vector fields for schematic design of a field cell with electric field parallel to the substrate and perpendicular to gravity. The blue colour is the glass slides, and green are the electrodes. The pink lines are the vector field lines and the red arrows are the electric vectors.

Figure 3.2 shows an electric field vector diagram of the electric field set-up. In this set-up a uniform force pointing to the left on a negatively charged particle was used. The lines are equipotentials while the arrows represent field vectors. The electric force on the particles are achieved by voltages applied across the electrodes (shown in green). From this diagram, it is clear that the most uniform fields are far from and in between the electrodes. For the largest applied voltages, when the particles will traverse the largest distance, it is possible that field non uniformities will become important.

3.3 Designs and Construction of Electric Field Cells

The electric field cells that were used in this thesis went through several different types and styles before reaching a final sample style which was used for most of the primary data collection. For completeness, a description of all the cell designs is provided here.

3.3.1 Electric Field sample Cell Design 1

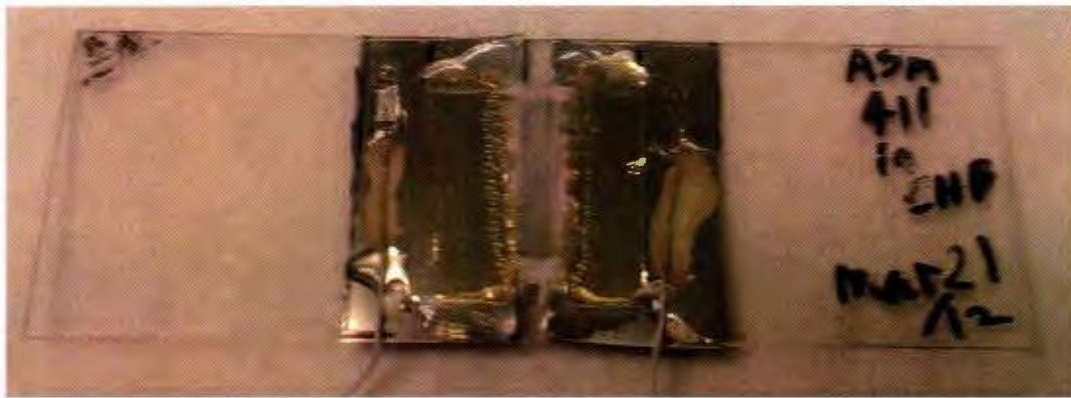


Figure 3.3: Design 1 for an electric field cell.

The first sample electric field cell design that was constructed is shown in figure 3.3. First a glass microscope slide was cleaned with acetone. Then two pieces of stainless steel were cut to size (which were used as the two electrodes) and taped on to the clean microscope slide using double-sided medical grade adhesive tape (*ARcare® 92712 Clear Polyester* by Insight Adhesives Research). Then a glass cover slide with a thickness of around 0.13 – 0.17 mm was taped on top of the two steel shims using the same double-sided adhesive tape. Afterward 30 gauge wires

were attached to the electrodes using drops of an ultraviolet-curing (“UV”) UV glue (“Norland Optical Adhesive 68” by Norland Products Inc.) and cured under a an ultraviolet (UV) lamp (Spectroline model SB-100P) for 15 minutes. Next a connection was made from the wire to the electrodes using silver paste (colloidal silver paste by Canemco Inc.). After the silver paste had dried, the conductivity of each electrode was tested using a multimeter. One end on the multimeter was attached to the end of one of the wires and the other end of the multimeter was place on the electrode. If the resistance from the end of the wire to the electrode was some low number (around 1Ω) then it was good connection. If the resistance from the end of the wire to the electrode was some high number (around $1M\Omega$) the it was a bad connection, at which point the wire was removed, cleaned, reattached and tested again until it was a good connection.

Next the cell was filled using one of the colloidal suspensions that were used for this experimental work (refer to section 3.4 for more details). Finally the cell was sealed using UV glue (refer to section 3.4 for details on how the cell was sealed). This first type of electric field cell had many problems with leaks, and the double-sided tape would also dissolve in the solvent.

3.3.2 The Zero Field Sample Cell

The cell in figure 3.4 shows a sample cell for an experiment where we did not apply a external electric field. In this case we would contain our colloidal suspension within a rectangular glass capillary ($0.10 \times 1.0\text{mm}$ by Vitrocom Inc.). Again the first step was to clean a glass microscope slide with acetone, and then on opposite side



Figure 3.4: A Design for a cell which did not have electrodes within it but was used for studying dynamics at zero fields as well as for testing the tracking code used in this experimental work. The black lines are guide lines, and are only used in the placement of the capillary tube.

on which the cell was to be built, guide lines are drawn. These lines only serve one purpose, which is to act as guide in the placement of the capillary tube. A capillary tube is then glued onto the microscope slide using UV glue and cured. The tube was then filled with the colloidal suspension and sealed (refer to section 3.4 for more details).

This type of cell was good for testing the code that was used to track the particle (discussed in section 3.6). This type of cell was also appropriate for studying dynamics at zero fields. Results of which can be seen in chapter 4.

3.3.3 Electric Field Sample Cell Design 2

The second electric field cell that was constructed is shown in figure 3.5. Again the first step was to clean a glass microscope slide with acetone, and then on the opposite side from the one on which the cell was to be built, guide lines are drawn.



Figure 3.5: Design 2 for an electric field cell. The black lines are guide lines, and are only used in the placement of the electrodes and the capillary tube.

These lines only serve one purpose, which is to act as guide in the placement of the electrodes and the capillary tube. Next a capillary tube with an square cross section ($0.10 \times 1.0\text{mm}$ by Vitrocom Inc.) was glued onto the cleaned microscope slide. Two thin wires (tungsten wire with a diameter of 0.05mm from Goodfellow Cambridge Limited) were then inserted through the tube to act as the electrodes. Two metal shims were also attached to the slide using UV glue and cured. The wires that were inserted into the tube were then attached to these shims using UV glue and cured. A connection was then made from the wires to the electrodes using silver paste. Then their conductivity was tested using a multimeter. The tube was then filled using one of the colloidal suspensions that were used for this experimental work and sealed (refer to section 3.4 for more details).

This type of electric field cell also had problems, although not as many as the first electric field cell design. The main problem with this type of cell was the overall thickness of the cell. One problem was that the wires could not be 100% straight

and were hard to straighten them within the capillary tube. Thus it is harder in this geometry to guarantee the uniformity of the electric field.

3.3.4 Electric Field Sample Cell Design 3

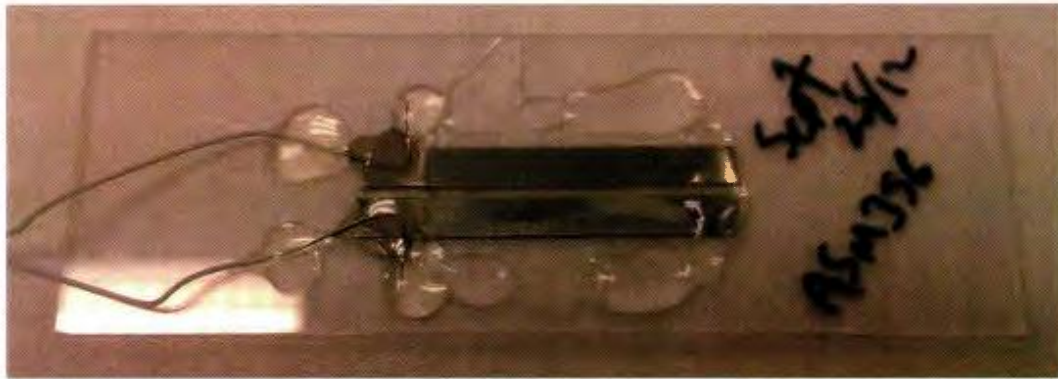


Figure 3.6: Design 3 for an Electric Field Cell. This design was used for the electric field experiments reported in this thesis

The third design for the electric field sample cell that was constructed is shown in figure 3.6 (refer to section 3.2 for more detail on the electrode geometry and electric field lines within the sample electric field cell). This cell follows the same idea as the first electric field cell design but improves the idea. First a glass microscope slide was cleaned with acetone, and then on the side opposite to the one on which the cell was to be built, guide lines were drawn. These lines only serve one purpose, which is to act as a guide in the placement of the electrodes. Again, stainless steels shims were used as electrodes but this time they were smaller and were machine cut for flatness. Then the electrodes were placed into position on the microscope slide. A clean glass cover slide was then placed on top of the electrodes and carefully clamped into place

such that the electrodes did not move nor did the glass cover move or break. Next UV glue (“Norland Optical Adhesive 61” by Norland Products Inc.) was placed along the edge of the cover slide, and due to capillary action the glue is sucked under the cover slide into the electrodes and stops. A weight was placed on the cover cell to maintain the thickness (the glue may push the cover slide up) of the cell then it is cured. After wires are attached to the electrodes, their conductivity was tested using a multimeter. The guides line on the other side of the cell were then washed off using acetone. The cell was then filled using one of the colloidal suspension that were for this experimental work and sealed (more details are given in the following section).

3.4 Filling the Electric Field Cell

Filling the electric field cell consisted of pipetting the colloidal suspension near one entrance to the cell. Due to capillary action the suspension was sucked in to fill the cell. Any excess solution at the edge was then wiped off.

The cell was sealed using a UV glue and cured under a UV lamp for 15 minutes. The area within the sample cell which will be looked at within the experiment was covered with a piece of aluminium foil or a metal plate to prevent “bleaching” from happening. Bleaching is the fading of the fluorescence dye that was used.

3.4.1 Colloidal Suspension

The colloidal suspension that was used within the experiment was $2\mu\text{m}$ diameter PMMA (poly(methyl methacrylate)) colloids, in a mixture of 67.5% v/v (volume/volume) CHB (cyclohexyl bromide) and 32.5% v/v decalin (decahydronaphtha-

lene) solvent. In table 3.1 is a list of the chemicals used and their refractive indexes and densities.

Table 3.1: Refractive index (n), and density (ρ) of the solvents and colloids.

Chemical Name	Refractive Index	Density ($\frac{\text{g}}{\text{cm}^3}$)
PMMA(Poly(methyl methacrylate))	1.4914	1.18
CHB(cyclohexyl bromide)	1.4957	1.382
Decalin (decahydronaphthalene)	1.4750	0.896
Solvent Mixture (67.5% CHB and 32.5% decalin)	1.4890	1.23

Note that the density for CHB in table 3.1 was found from weighing know volumes (taking a average of three different runs) of the solvent and using $\rho = \frac{m}{V}$.

Now assuming that there is no volume change during mixing, the Arago-Biot equation can be used to find the refractive index and density of the mixed solvents. This equation states [33]:

$$n_{12} = \phi_1 n_1 + \phi_2 n_2 \quad (3.1)$$

with n_i , ($i = (1, 2)$) as the refractive index of the two pure solvents, n_{12} is the mixture refractive index, and ϕ_i , ($i = (1, 2)$) as the component of the volume fraction of the two pure solvents. Similarly for the densities:

$$\rho_{12} = \phi_1 \rho_1 + \phi_2 \rho_2 \quad (3.2)$$

with ρ_i , ($i = (1, 2)$) as the densities of the two pure solvents, ρ_{12} is the mixture density. Now comparing these two values (n_{12} and ρ_{12}) with the values for PMMA

the values should be close. Thus from table 3.1, with $\rho_1 = 0.675$ and $\rho_2 = 0.325$, the mixture is only 0.16% off from the colloids refractive index and 4.07% off from the colloids density. For our experiments, this mismatch in density is actually desired in order to have the colloids migrate to one of the surfaces. The Bjerrum length is the separation in the solvent where the electrostatic energy between two electrons equals $k_B T$. In our solvent mixture the Bjerrum length is calculated to be 103 Å.

3.5 The Control Hardware

The experimental set-up for the control of the electric field within the sample cell is shown in figure 3.7. A function generator (Tektronix AFG3002 Dual channel function generator) output is connected to both channel 1 of an oscilloscope (Tektronix TDS1002 Two Channel digital oscilloscope) and to a wideband amplifier (Krohn-Hite Corporation model 7662M wideband amplifier). The output of the amplifier is connected to both channel 2 on the oscilloscope by a divide-by-10 oscilloscope probe (Tektronix P2220 Voltage Probe) and to the sample cell which is mounted on a sample stage of a microscope which is discussed next.

3.5.1 Optical Microscopy

In this work, a Nikon Eclipse 80i upright optical and confocal microscope is used. A Qimaging QICAM fast1394 12-bit monochrome camera (model QIC-F-CLR-12-C) is mounted on the microscope rear port, and is used to image the particles that were to be tracked within the sample cell (with sample EH01). The other set of experiments (with sample EH02) was carried out with a camera (model PCO.Edge) capable of

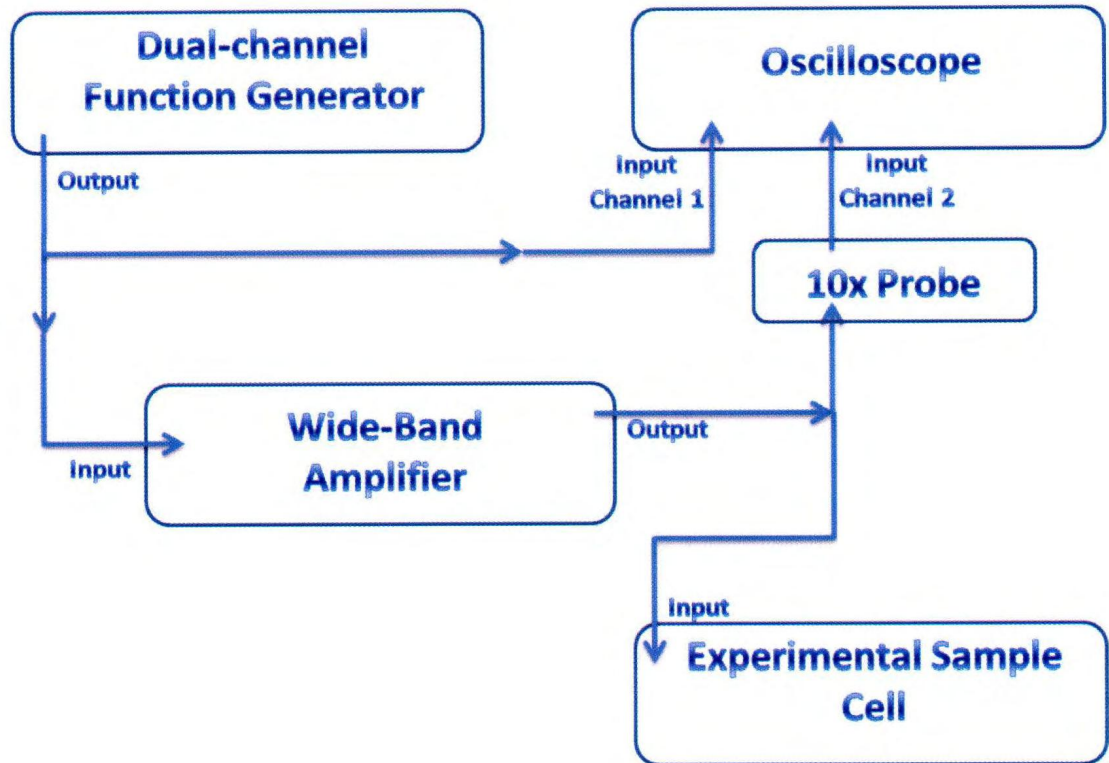


Figure 3.7: Experimental set-up for the applied AC electric field. A function generator output is connected to both one channel on a oscilloscope and to a wideband amplifier. The output of the amplifier is connected to both a second channel on the oscilloscope by a divide by 10 probe and to the sample cell

higher frame rates. Fluorescence microscopy is used to track the particles instead of bright field microscopy due its enhanced rejection of non-fluorescing objects and its rejection of scattered incident light.

Bright field microscopy (BFM) uses a white light source in order to illuminate the entire area of interest. Places within the area of interest which have some object there, be it the sample or dust/dirt, appear darker with a bright background. BFM normally has a lower contrast as compared to some other microscopy techniques. But BFM is a very simply set-up, needing only a white light source, thus is used to carry out initial tests of the sample.

Fluorescence microscopy (in this case epifluorescence microscopy and not fluorescence confocal microscopy) uses a light source (in this case a mercury lamp) which emits light over a broad wavelength range. The light is then passed by a filter such that only a narrow wavelength range hits the area of interest. Objects in the area of interest that have been “marked” with a fluorescent dye will be excited by that wavelength and they subsequently emit light at a longer wavelength than the input wavelength. The light that comes from the area of interest is then filtered again such that only light at the longer wavelength can pass the filter. Thus, in our experiments, only the particles that fluoresce light were picked up, blocking out scattered light from non-fluorescing objects. This light was recorded with a monochrome camera where intensity from the full range of the emission spectrum of the fluoresce is recorded in one grey-scale image, under a range of 0 to 255 “grey-levels”.

The colloidal particles (PMMA (Poly(methyl methacrylate))) that were used within this thesis were labeled with a fluorescent dye (NDB-Cl [4-Chloro-7-nitrobenzofurazan]) that was excited by a blue wavelength, and emits in the green wavelength range. This



Figure 3.8: The Nikon Eclipse 80i C1+SHV confocal microscope with a Qimaging QICAM fast1394 12-bit monochrome camera (mounted on the rear port).

fluorescent dye eventually bleaches after exposures of extended duration. Bleaching is the fading of the fluorescence of the dye. After the particles have bleached then the experiment is continued by translating the sample to a new unbleached area.

3.6 Particle Tracking Software

In this thesis, particle tracking refers to the investigation of colloidal particle positions as a function of time within a solvent. The list of coordinates of the particles over a series of time steps is referred to as the “particle tracks”. The tracks can then be analysed to identify what is happening to each particle motion as a function of time.

Movies (image .tiff stacks) were acquired using the camera (Qimaging QICAM fast1394 12-bit monochrome camera) software. These movies are a series of images taken at a frame-rate which was set within the camera software, and were checked by cross-calibrating by acquiring images of a stopwatch having 10 ms second resolution.

After a movie was acquired, the stack was then analysed using computer programmes that were coded in IDL (Interactive Data Language by Exelis Visual Information Solutions). IDL is a programming language and is popular for data analysis of large sets of images. This language is often used for astronomy, medical imaging, and colloidal systems. The IDL data analysis code that was used follows the procedures outlined by Dr. John C. Crocker and Dr. David G. Grier [34] (refer to reference [35] for the outline of the code by Dr. Eric R. Weeks).

Within the code, the colloidal particles are found for each image in the tiff stacks are assigned a particle number (or ID) as well a set of coordinates (x,y). Also from

one image to the next the particles are linked together. This is done by creating a circle of some distance from the place of the first set of coordinates for each particle and checking to see if any particle coordinates in the next set fall within this circle. The code then assumes that these two particles are the same and thus they are given the same particle ID. Thus after the tracking has finished, there is a list of particle IDs with a set of coordinates as a function of frame number, which in our experiments represents time.

Since our experiments are carried out near the surface, particles sometimes stick to the surface. Thus the code identifies which particles are stuck and non-stuck next. This is done by taking the average distance that a particle centroid move from one image to the next. If this average distance is less than some threshold value (a value of $0.04a - 0.06a$ was used) then the particle is assume to be stuck. This stuck threshold is not set to 0, but to some small number to allow for some pixel noise in the tracking code. Then the code solves all the particle displacements, and from this the distance from starting position is calculated. The code also places circles around both the stuck and non-stuck particles on separate images for all the frames. This was done so that a visual inspection of the assortment of the stuck and non-stuck particle could be made.

The next part of the code solves for the mean displacement (MD, $\langle x \rangle$), the mean square displacement (MSD, $\langle x^2 \rangle$), the mean cubed displacement (MTD, $\langle x^3 \rangle$), and the mean fourth power displacement (MFD, $\langle x^4 \rangle$) of the particles. This is done by calculating the displacement for different time steps, and finding the square displacement, the cubed displacement, and the fourth power displacement from the displacement at these different time steps. Next each displacement at each

time step is averaged to find their mean. Next for the MSD, the MTD, and the MFD, the average ‘drift’ is then removed; refer to table 3.2 for each displacement correction equation. This drift correction was found to be quantitatively very tiny in our experiments (of around 0.01a).

Table 3.2: Table of Mean Displacements Corrected Equations

Names	Correction Equation
MD	$\langle x \rangle = \langle x \rangle$
MSD	$\langle x^2 \rangle = \langle x^2 \rangle - \langle x \rangle^2$
MTD	$\langle x^3 \rangle = \langle x^3 \rangle + 2 * (\langle x \rangle^3) - 3 * (\langle x^2 \rangle * \langle x \rangle)$
MFD	$\langle x^4 \rangle = \langle x^4 \rangle + 6 * (\langle x \rangle^2 * \langle x^2 \rangle) - 4 * (\langle x \rangle * \langle x^3 \rangle) - 3 * \langle x \rangle^4$

The final step is to cluster the particles into groups. This step of the code was written for this thesis. Two particles that are less than a user-defined distance apart are linked as members of one “cluster”. A third particle that is less than this threshold distance from any particle in this cluster belongs to this cluster as well. On each image the code assign the first particle with a cluster ID, then each subsequent particle is checked to see if it falls within a user defined distance from another particle. If it does fall with that distance then those particles are assigned the same cluster ID (the lower of the two cluster ID’s). Next, for each image a table is made and the particle number and cluster ID are placed in the table. Now the code checks to make sure that cluster from one image to the next have the same cluster ID, if not, the later cluster is reassigned a cluster ID.

There was also an optional piece of code to handled stacks where the particles have

moved more than one diameter between two frames. This optional piece needed an additional data file. This data file comes from tracking a particle x and y positions in pixels by hand. The particle was selected after watching the movie for some time to select a particle that was a good reference particle for the whole movie. Then the particle initial position is subtracted from all of the positions. This gives a displacement for that particle and this displacement was assume to be average displacement for the whole stack. Next at each image the average displacement for that frame was subtracted from each particle. The stack was then track and the average displacement at each frame was added back to corrected what was subtracted before the tracking.

All the data that the code has found was then outputted to .dat files which could be read in by plotting software (Igor Pro, Wavemetrics Inc.) and plotted.

Chapter 4

Results

4.1 Introduction

In this chapter the results of three viscosity measurements that were done on the solvent of cyclohexyl bromide and decalin that was used, will be reported. Following this, the main experimental results on colloidal dynamics in an external electric field, as a function of field frequency and field strength, will be reported.

4.2 Viscosity Measurement

Figure 4.1 shows plots of stress versus the shearing strain for three different experimental runs on the solvent of 67.5% v/v (volume/volume) CHB (cyclohexyl bromide) and 32.5% V/V decalin (decahydronaphthalene) with linear fit lines for each experimental run. The slope of the linear fits lines is equal to the viscosity of the solvent. Taking an average of the three experimental data runs one can get a value of about 2.11 mPa * s. This value was used in calculating the Reynolds

number is section 2.3 and in the calculations of the Stokes-Einstein equation outline in section 2.5.2 and was done in section 4.3.

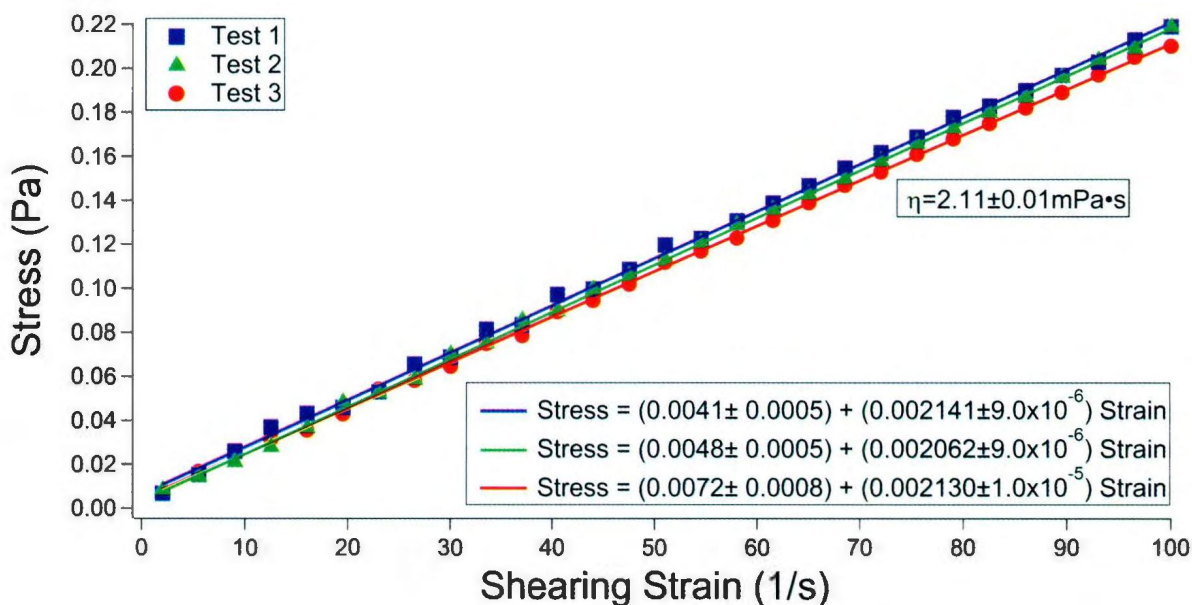


Figure 4.1: Stress versus strain relationship for solvent mixture at $T = 22^{\circ}\text{C}$ of 67.5% CHB (cyclohexyl bromide) and 32.5% decalin(decahydronaphthalene) used in the electric field studies. Shown also are the linear fits, and the viscosities from the fitted slopes.

4.3 Stokes-Einstein-Sutherland Diffusion Coefficient

As discussed in section 2.5.2 the colloid diffusivity, in the absence of external forces, can be calculated from equation 2.4. Using the viscosity found in section 4.2:

$$D = \frac{(1.38 * 10^{-23} \frac{J}{K})(295 K)}{6\pi(2.11 * 10^{-3}\text{Pa} * \text{s})(1 * 10^{-6}m)} \quad (4.1)$$

which works out to be $D_{SES} = 0.102 \pm 0.002 \mu\text{m}^2/\text{s}$.

4.4 Colloidal Dynamics in Electric Fields

Two samples were used in the experiments carried out for this thesis. These two samples will be referred to as EH01 and EH02. These samples both had similar compositions. Both were composed of $2\mu\text{m}$ diameter PMMA (poly(methyl methacrylate)) colloids, in a refractive-index matching but density mis-matched solvent mixture (67.5% V/V (volume/volume) CHB (cyclohexyl bromide) and 32.5% V/V decalin (decahydronaphthalene)). The stock suspensions for EH01 had particle concentrations of 3.49% M/V (mass/volumes) and EH02 has 3.70% M/V. However, because the area packing fraction (α) of the colloidal monolayer is also a function of the sample thickness these two samples had different area fractions α (for EH01 $\alpha = 0.082$ and for EH02 $\alpha = 0.076$).

It should be noted that for both samples the electrode spacing was the same at 1 mm, thus for 7 volts applied to both EH01 and EH02, the electric field strength was 7 V/mm . The main contribution to the error in electric field strength ($\pm 0.1 \text{ V/mm}$) came from an uncertainty in electrode spacing. In addition, since in the experiments the electric field direction was along x and dynamics parallel and perpendicular to the field is monitored, the results had to be carefully corrected for small possible mis-orientations of the camera with respect to the electric field direction. A description of the procedure is in Appendix A.

4.5 Sample EH01: Area Fraction $\alpha = 0.082$.

Experiments on sample EH01 were carried out using a 40x oil immersion objective, using fluorescence optical imaging and the experimental set up described in section 3.5. Once the conditions under which the sample was exposed were considered to have reached a steady state, such that most of the particles are within a layer (typically 15 minutes) the data acquisition consisted of an movie of images, typically around 200 \sim 300 frames. Results are reported first at zero electric field, and then for applied electric fields at different frequencies and amplitudes.

4.5.1 EH01: Zero Field

Figure 4.2 shows a plot of $\log(\text{MSD})$ vs $\log(\text{time})$ at zero field for sample EH01. From the linearity of this plot, we see that the scaling is $\text{MSD} = t^\gamma$. The linear behaviour is fitted to obtain an average value of $\gamma = 1.04 \pm 0.01$, which is consistent with normal diffusion ($\gamma = 1$). The reported error in γ arises from the difference between the fits for the $\langle X^2 \rangle$ and $\langle Y^2 \rangle$ measurements, which are in principle identical; this difference is larger than the error reported in the fits.

Figure 4.3(a) shows the pair correlation for this sample at zero field. The peak at $r/\sigma \sim 2$, with a peak height of about 1.4, indicating weak structuring in a relatively dilute colloidal fluid phase. The existence of weak structuring is inferred from that fact that the first peak in the $g(r)$ arises at relatively low densities, and there are no visible secondary peaks.

Finally, at zero field, we plot the MSD vs time in figure 4.3(b). This relationship is linear, and from the slope we obtain the diffusion coefficients along the x and y

directions, with an average value $D_{NF}^{EH01} = 0.048 \pm 0.002 \mu\text{m}^2/\text{s}$. Comparing this with the bulk value, $D_{SES} = 0.102 \mu\text{m}^2/\text{s}$, we see that the colloid diffusion constant is roughly half the expected bulk value. The reason for this slowing down was discussed in section 2.11 where it was pointed out that hydrodynamic interactions with a hard wall can slow down colloidal diffusion. In chapter 5 section 5.4.1.1, this is used to quantify distance from the wall, and put a numerical value on the two-dimensionality of the system.

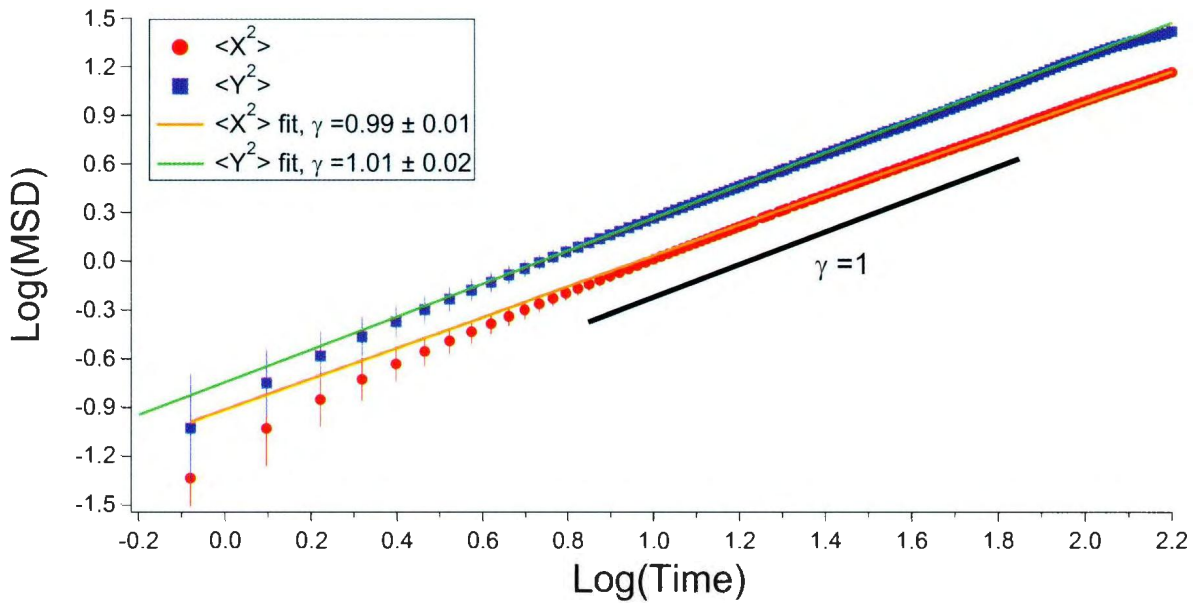
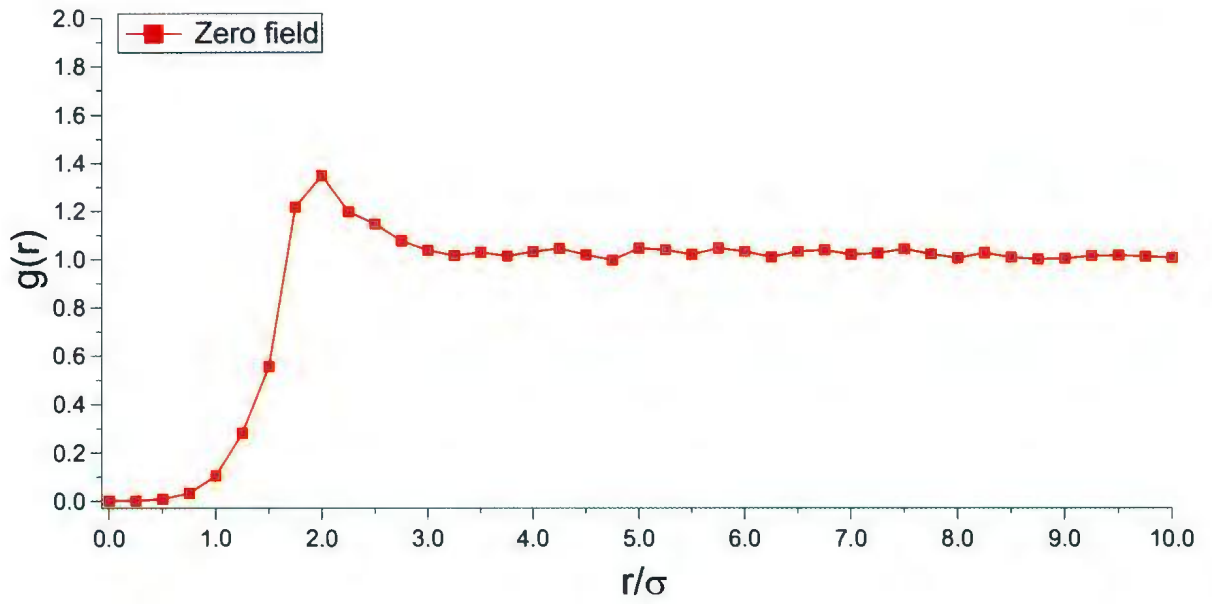
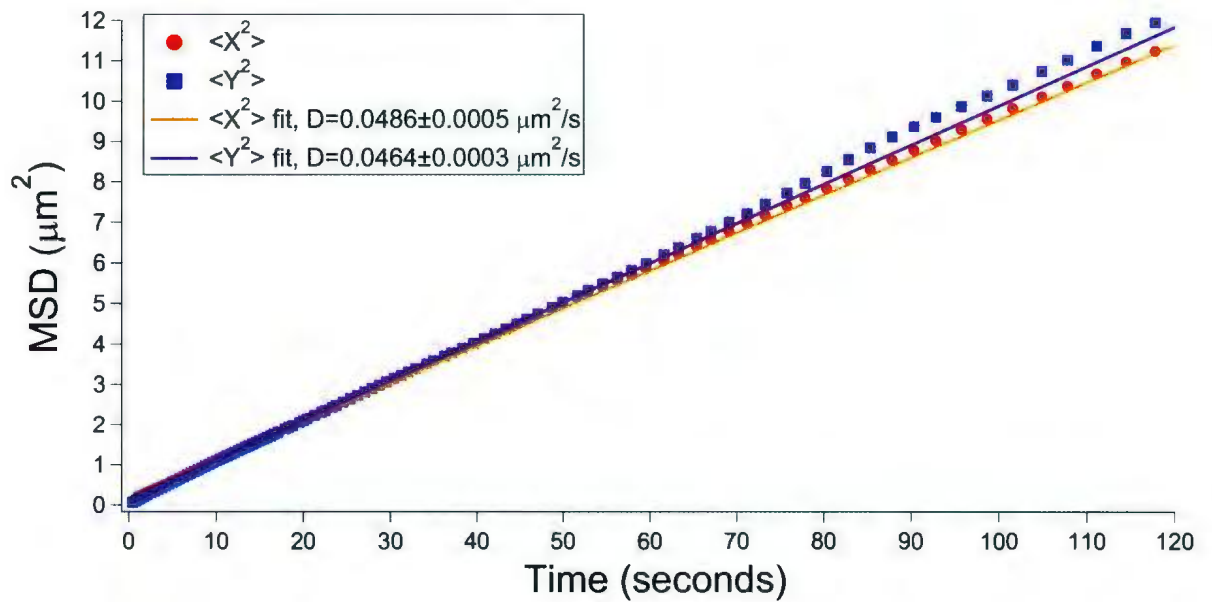


Figure 4.2: EH01, zero field. At zero field, the dynamics is diffusive: if one writes $MSD = t^\gamma$, then a linear fit to $\log(MSD)$ vs $\log(t)$ yields a slope $\gamma = 1.04 \pm 0.01$ consistent with $\gamma = 1$.



(a)



(b)

Figure 4.3: (a) EH01, zero field. Pair correlation function shows a peak at $r/\sigma \sim 2$. The height of this peak is 1.4 indicating weak structuring. (b) EH01, zero field. Mean square displacement ($\langle X^2 \rangle$, $\langle Y^2 \rangle$) versus time is linear, and yields an experimental diffusion coefficient of $D_{NF}^{EH01} = 0.048 \pm 0.002 \mu\text{m}^2/\text{s}$.

4.5.2 EH01: $f = 250$ mHz

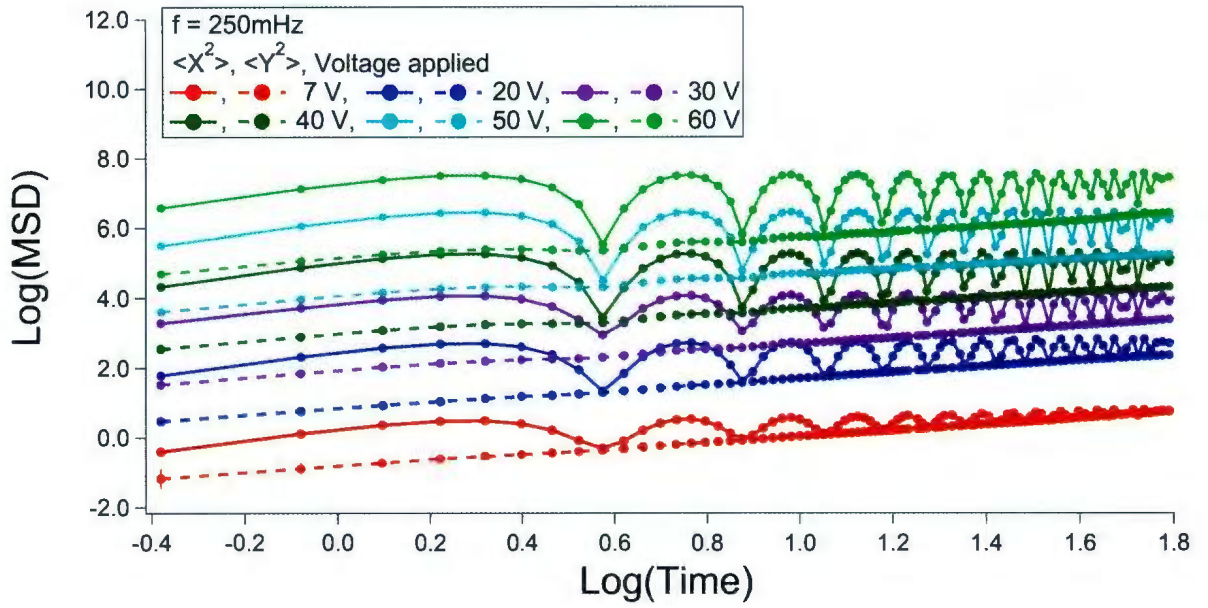
Figure 4.4(a) shows a plot of $\log(\text{MSD})$ vs $\log(\text{time})$ at 250 mHz with voltages that ranged from 7 volts up to 60 volts for sample EH01, which corresponds to an electric field amplitude ranging from $E_0 = 7$ V/mm to $E_0 = 60$ V/mm. The data for $\langle Y^2 \rangle$ at all of the voltages has a linear behaviour at short and long times, which will be looked at more carefully in figure 4.4(b). The data for $\langle X^2 \rangle$ at all of the voltages roughly follows the same pattern, where as the voltage increases so does the amplitude of the sinusoidal oscillations. This pattern is that at short times, $2 > \gamma > 1$ meaning that the colloids are being directed by an external force (the applied electric field) and that, at long times, the slope trends to $\gamma = 1$ at long time. It should be noted that if one sampled the motion along X once per cycle of the applied electric field, this stroboscopically sampled $\langle X^2 \rangle$ behaves just like $\langle Y^2 \rangle$.

Figure 4.4(b) show a plot of the $\log(\langle Y^2 \rangle)$ vs $\log(\text{time})$ at the different electric fields. The slopes at short and long times are different, with a plateau-like region in between. This is shown by extrapolating the fit at short times (red dotted line on top curve, i.e. 60 V/mm). Thus the dynamics is diffusive at short times ($\gamma \sim 1$), and sub-diffusive at intermediate times, which should return to nearly diffusive behaviour at longer times.

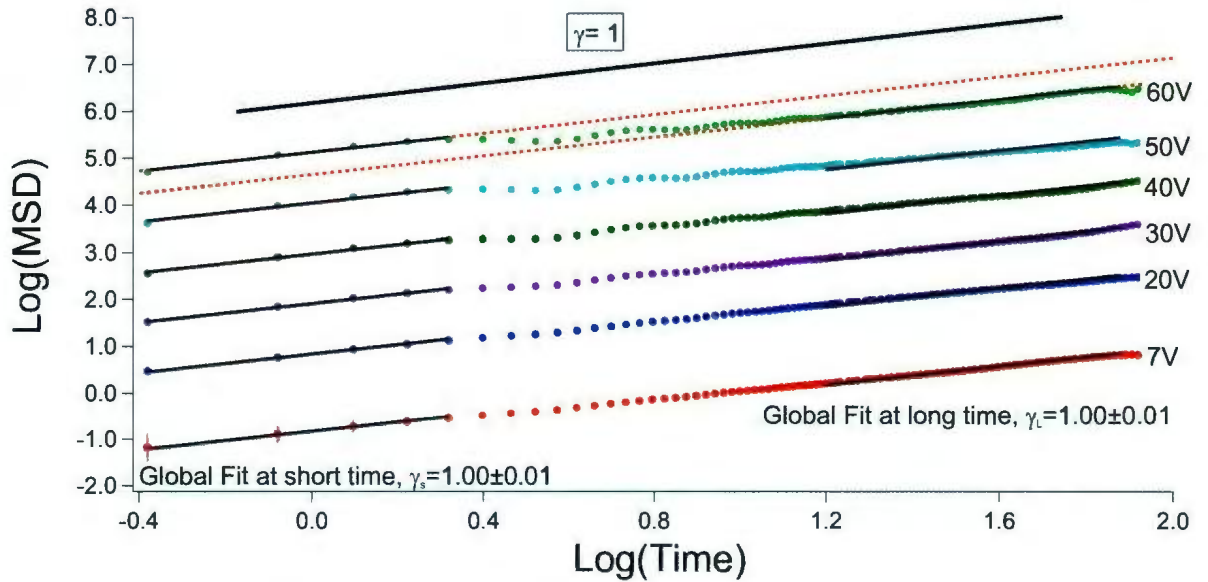
Figure 4.5(a) shows the pair correlation function for this sample at the different electric fields. It should be noted that as the voltage increase, so does the size of the first peak at around $4\frac{r}{\sigma}$. This indicates that there is weak structuring in a relatively dilute colloidal fluid phase which get stronger as the voltage increases. Plotted in figure 4.6 is the MSD vs time for an applied field of 7V/mm at $f = 250$ mHz. At

low fields, the mean squared displacements along y are essentially unchanged from the zero-field values. The diffusion coefficient obtained along y is equal to $D_{250mHz}^{EH01} = 0.043 \pm 0.001 \mu\text{m}^2/\text{s}$. Again comparing this with $D_{SES} = 0.102 \mu\text{m}^2/\text{s}$, we see that this value is less than half the expected bulk value, but consistent with the zero-field value in figure 4.3. This will be discussed later on in chapter 5 section 5.4.1.1.

Another curious point is the small jump in the MSD between 7V and 20V in both figure 4.4(a) and figure 4.4(b). Associated with this is a noticeable shift in the position of the first $g(r)$ peak. Both these effects could be related to the thin colloidal sediment becoming more two-dimensional. A quasi-3-dimensional sediment (where there are particles excursions out of plane) would result in projected distance in a 2D $g(r)$ appearing smaller. This would also affect the 2D mean squared displacements.

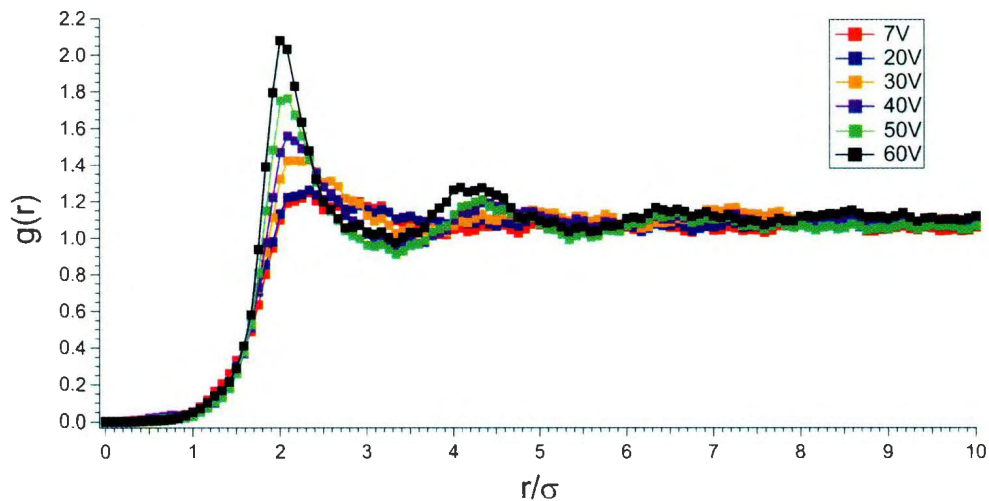


(a)

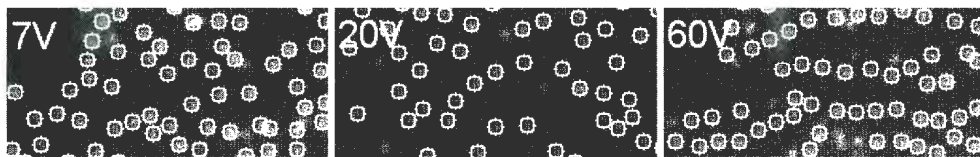


(b)

Figure 4.4: (a) EH01, $f= 250\text{mHz}$ with voltages ranging from 7 to 60V. Results at each voltage are offset upwards from the previous voltage by 1 unit.(b) EH01, $f= 250\text{mHz}$ with voltages ranging from 7 to 60V, $\langle Y^2 \rangle$ data only. Results at each voltage are offset upwards from the previous voltage by 1 unit.



(a)



(b)

Figure 4.5: (a) EH01, $f = 250\text{mHz}$ with voltages ranging from 7 to 60V (or electric field amplitudes E_0 from 7 to 60 V/mm). The pair correlation function shows a peak at $r/\sigma \sim 4$. The height of this peak ranges from 1.4 to 4.0, indicating weak structuring at low fields but getting stronger at higher fields. (b) EH01, $f = 250\text{mHz}$. Montage of area from single frames of tracked data at 7V, 20V and 60V.

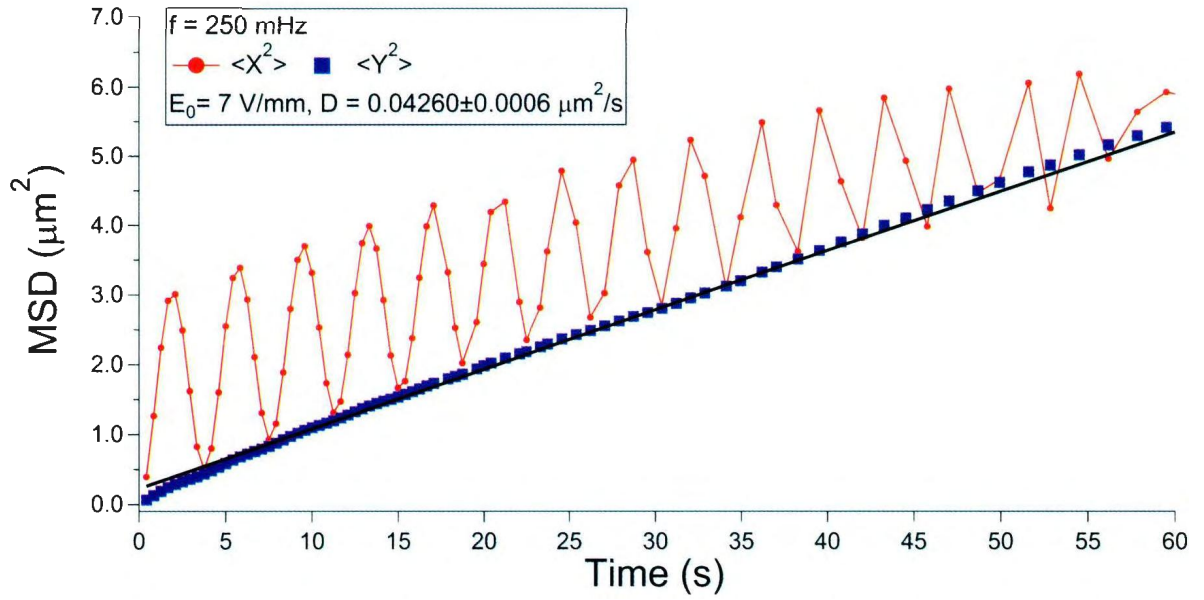


Figure 4.6: EH01, $f = 250\text{mHz}$ with $7\text{V}/\text{mm}$. $\langle Y^2 \rangle$ versus time is linear, and yields an experimental diffusion coefficient of $D_{250\text{mHz}}^{EH01} = 0.043 \pm 0.001 \mu\text{m}^2/\text{s}$. The dynamics along the field direction, if analysed stroboscopically (looking only at the minima) is also diffusive with almost the same behaviour.

4.5.3 EH01: $f = 500$ mHz

Figure 4.7 shows a plot of $\log(\text{MSD})$ vs $\log(\text{time})$ at 500 mHz with voltages at 8 volts and 30 V ($E_0 = 8$ and 30 V/mm) for sample EH01. The data for $\langle Y^2 \rangle$ at the lowest voltage appears to have a linear behaviour with $\gamma \sim 1$ at all times, which is consistent with normal diffusion. The data for $\langle X^2 \rangle$ at 8 V/mm follows a similar trend as at 250mHz where the data oscillates at the applied frequency of the applied electric field. At 8V/mm (as with the results at 7V, 250 mHz shown in figure 4.6), the oscillation appears uncoupled with the normal diffusive motion, because the minima of the oscillatory motion coincides with the Y diffusion. The results for $\langle Y^2 \rangle$ at the higher field strength appears to be affected by the motion along X, and oscillates in phase with $\langle X^2 \rangle$ but with much smaller amplitude. This indicates coupling between x (which the force was applied along) and y (which is restricted because of the motion along x) driven motions at higher driving amplitudes. The mean-squared displacements at 30 V/mm are not plotted because there were intermittent problems particle tracking in this dataset. However, the pair correlation function could be calculated and will be this is discussed next.

Figure 4.8(a) shows the pair correlation for this sample at the same two field strengths. It should be noted that as the voltage increase from 8 to 30 V, the position of the peak shifts from $r/\sigma = 2$ to 3.5. At the same time the peak height increases from 1.4 to over 5. This indicates that there is weak structuring at the lower voltage but at the higher voltage there is much stronger structure; this can be seen in figure 4.8(b) where the first image is a single frame at 8 volts where the formation of chains can be seen starting to happen, and the second image is a single frame at 30 volts where

there are well formed chains.

Since the results along the Y direction at 8V/mm in Figure 4.7 are consistent with $\gamma = 1$, we can extract the diffusion coefficient from a plot of MSD vs. time, shown in figure 4.9, also from these results, we obtain the diffusion coefficients along the Y direction. This diffusion is equal to $D_{500mHz}^{EH01} = 0.061 \pm 0.001 \mu\text{m}^2/\text{s}$. Again comparing this with $D_{SES} = 0.102 \mu\text{m}^2/\text{s}$, we see that this value is roughly 60% the expected bulk value. The dynamics along the field direction is, however, sub-diffusive, and remarkably slower than the dynamics perpendicular to the field.

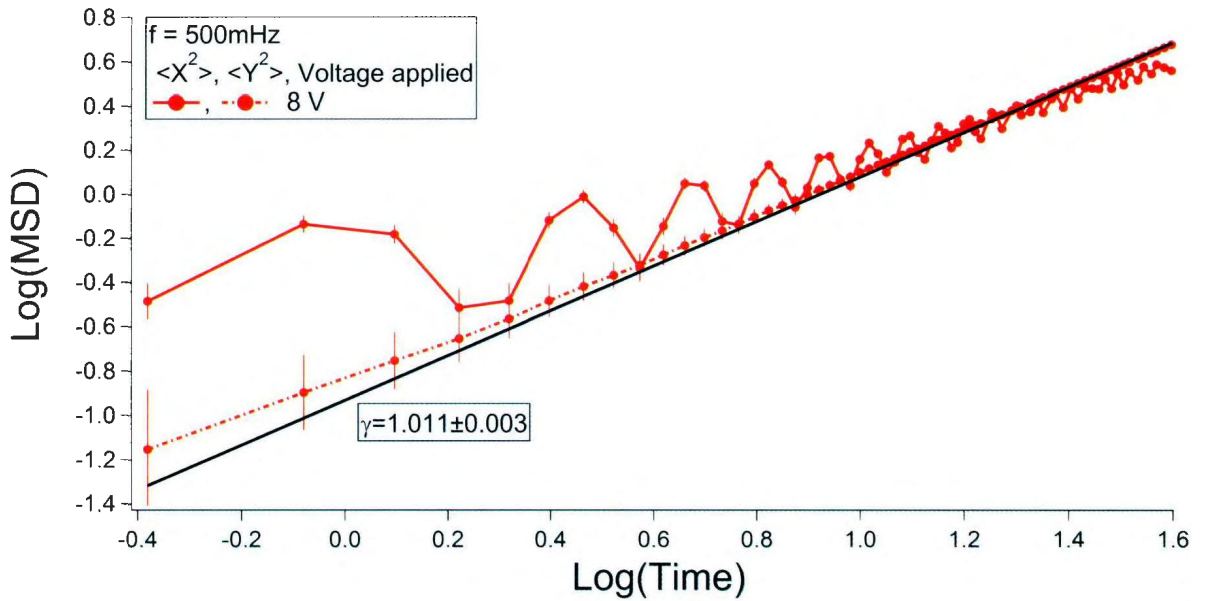
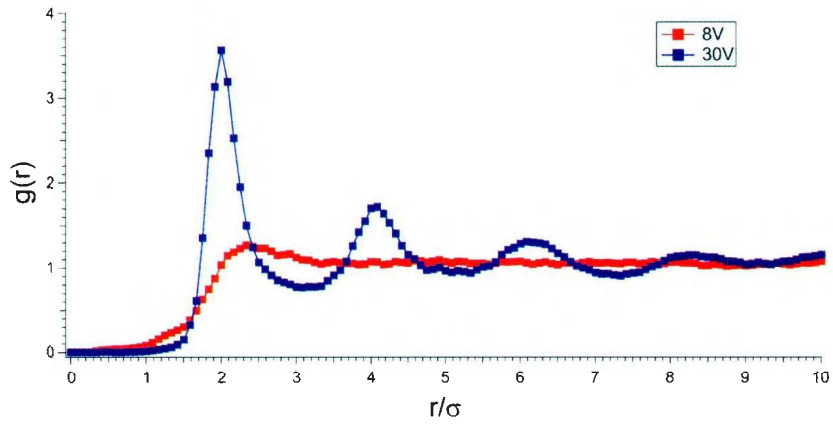
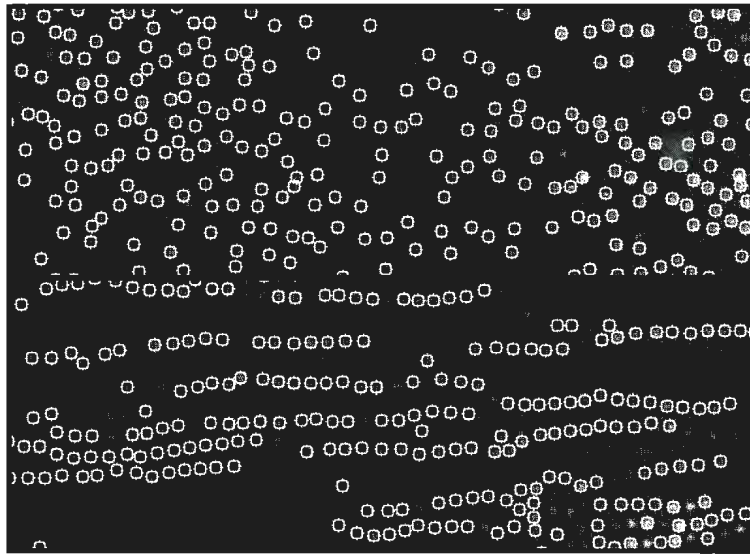


Figure 4.7: EH01, 500mHz at electric fields of 8 V/mm. The 8 V/mm results show normal behaviour in Y with weak oscillatory behaviour in X.



(a)



(b)

Figure 4.8: (a) EH01, $f = 500\text{mHz}$, $E_0 = 8$ and 30 V/mm. The pair correlation function shows a peak between $r/\sigma \sim 2$ for 4 V/mm, but shifts to $r/\sigma \sim 3.5$ for 30 V/mm. At the same time the peak height changes dramatically from about 1.4 to over 5 indicating a significant increase in structuring. (b) Frames from sample EH01 at 500mHz at 8 V and 30 V, showing the onset of chain formation and well-formed chains respectively.

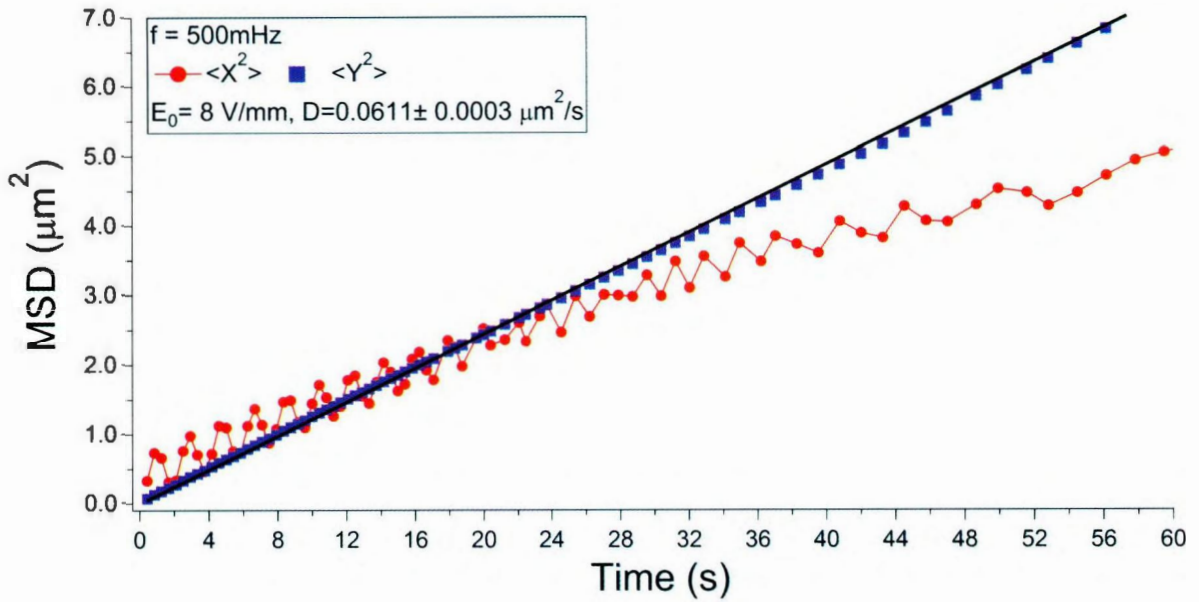


Figure 4.9: EH01, $f = 500\text{mHz}$ with $8\text{V}/\text{mm}$. $\langle y^2 \rangle$ versus time is linear, and yields an experimental diffusion coefficient of $D_{500\text{mHz}}^{\text{EH01}} = 0.0611 \pm 0.0003 \mu\text{m}^2/\text{s}$.

4.5.4 EH01: $f = 1 \text{ Hz}$

Figure 4.10 shows a plot of $\log(\text{MSD})$ vs $\log(\text{time})$ at 1 Hz with a voltage of 10 volts ($E_0 = 10 \text{ V}/\text{mm}$) for sample EH01. The results for $\langle Y^2 \rangle$ appears to have a linear behaviour with $\gamma < 1$ at all times. $\langle X^2 \rangle$ follows a similar trend as for $f = 250\text{mHz}$ with a sinusoidal oscillation at the frequency of the applied electric field. However, this is not seen as clearly because of the limited time resolution in this experiment.

Figure 4.11 shows the pair correlation for this sample at this field strength. It should be noted that the position of the first peak happens at $r/\sigma = 2$ with a value of around 1.7 . This indicates that there is weak structuring as in figure 4.3(b).

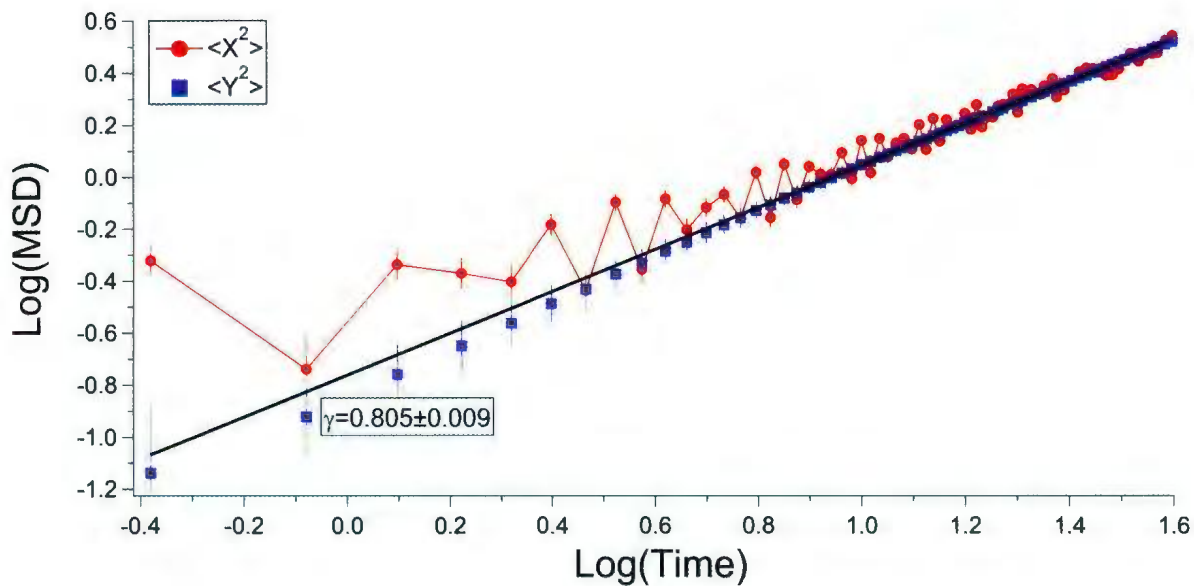


Figure 4.10: EH01, 1Hz at electric fields of 10 V/mm. The results show linear behaviour in Y, with $\gamma = 0.8$, less than the $\gamma = 1$, normal diffusion behaviour.

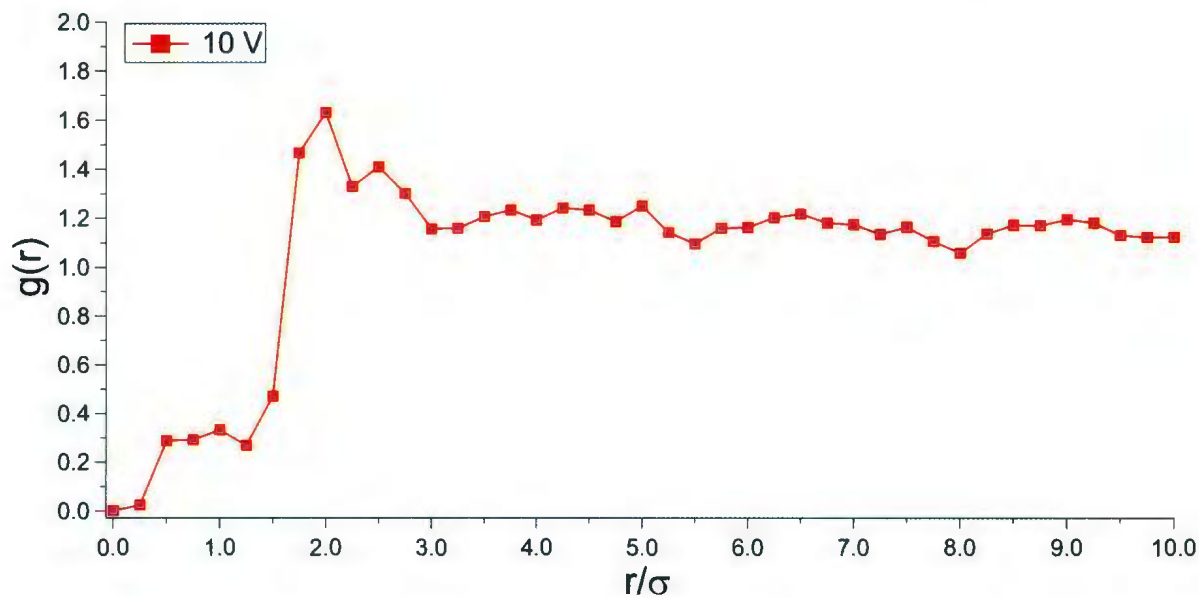


Figure 4.11: EH01, 1Hz at electric fields of 10 V/mm. Pair correlation function shows a peak at $r/\sigma \sim 2$. The height of this peak is at 1.7, indicating weak structuring.

4.5.5 EH01: $f = 5$ Hz

Figure 4.12 shows a plot of $\log(\text{MSD})$ vs $\log(\text{time})$ at 5 Hz with a voltage of 16 volts ($E_0 = 16$ V/mm) to sample EH01. The data for $\langle Y^2 \rangle$ appears to have a linear behaviour with $\gamma < 1$ at all times. The data for $\langle X^2 \rangle$ appears to have two linear but sub-diffusive regimes. The first one, at short times, appears to coincide with $\langle Y^2 \rangle$, and the second one, at long times, appears to have a slope closer to one.

Figure 4.13 shows the pair correlation for this sample at this field strength. It should be noted that the position of the first peak happens at $r/\sigma = 2$ with a value of around 3.4. This indicates that chains are starting to form.

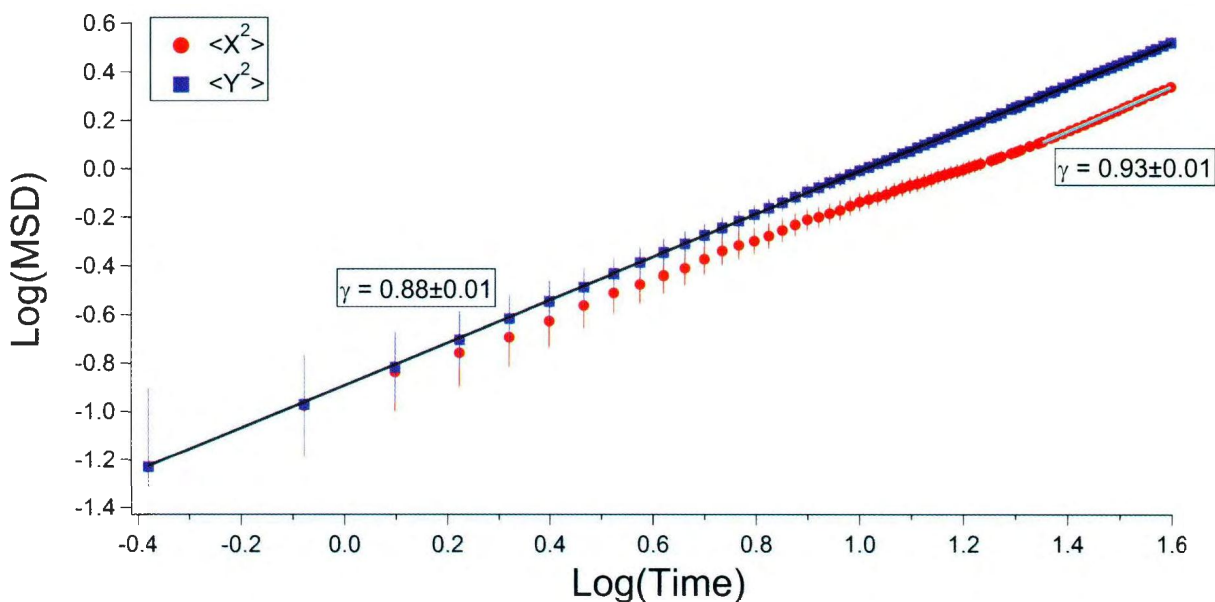


Figure 4.12: EH01, $f = 5$ Hz, $E_0 = 16$ V/mm. $\langle Y^2 \rangle$ shows a single sub-diffusive behaviour at all times, while $\langle X^2 \rangle$ shows a transition from sub-diffusive behaviour at short times to somewhat less sub-diffusive behaviour at long times.

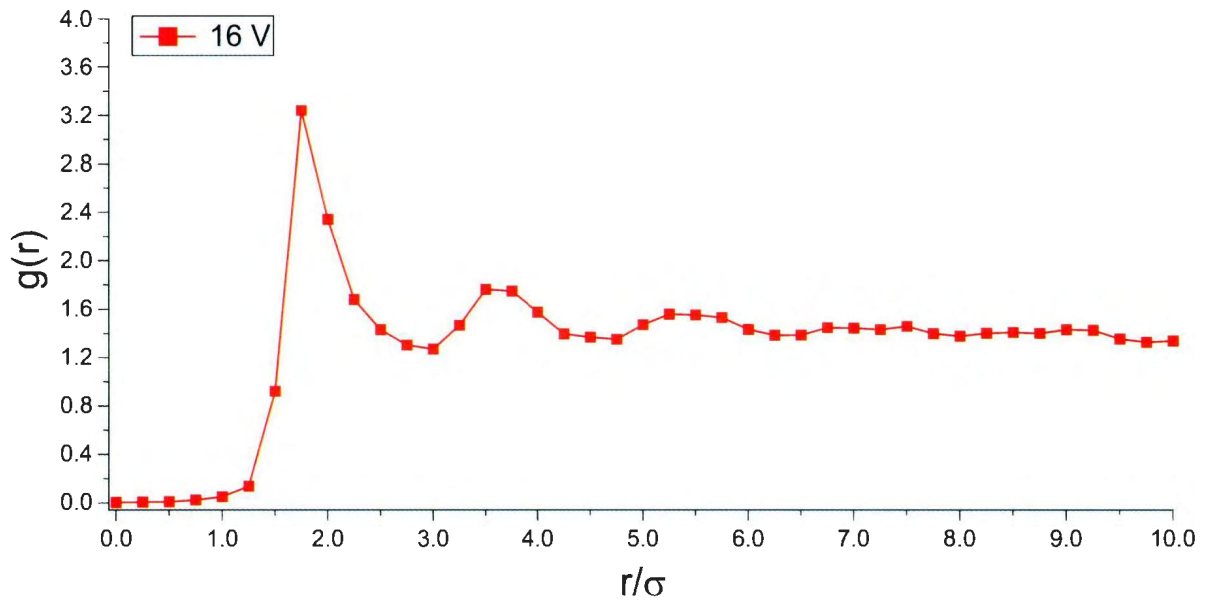


Figure 4.13: EH01. $f = 5$ Hz, $E_0 = 16$ V/mm. Pair correlation function shows a peak at $r/\sigma \sim 2$. The height of this peak is at 3.3, indicating that this peak correlates to the formation of chains. The existence of structuring is inferred from that fact that the first peak is around 3.2, with visible secondary and third peaks.

4.5.6 EH01: $f=10$ Hz

Figure 4.14 shows a plot of $\log(\text{MSD})$ vs $\log(\text{time})$ at 10 Hz at electric fields of $E_0 = 17$ and 30 V/mm. The data for both $\langle Y^2 \rangle$ and $\langle X^2 \rangle$ at the lowest voltage appears to exhibit sub-diffusive behaviour at all times with $\gamma = 0.8$. At the higher voltage the $\langle Y^2 \rangle$ data appears to exhibit sub-diffusive behaviour with $\gamma = 0.54$ at all times while the data for $\langle X^2 \rangle$ appears to have two linear regimes. The first one, at short times, is sub-diffusive with $\gamma = 0.35$ and the second one, at long times, is super-diffusive with $\gamma = 1.48$.

Figure 4.15(a) shows the pair correlation for this sample at the same two field strengths. It should be noted that as the voltage increase from 17 to 30 V, the position of the peak remains at $r/\sigma \sim 2$. At the same time the peak height increases from 3.6 to over 4.4. This indicates that there is weak structuring at the lower voltage but at the higher voltage there is much stronger structure; this can be seen in figure 4.15(b) where the first image is a single frame at 17 volts where the formation of chains can be seen to be starting to happen, and the second image is a single frame at 30 volts where there are well formed chains.

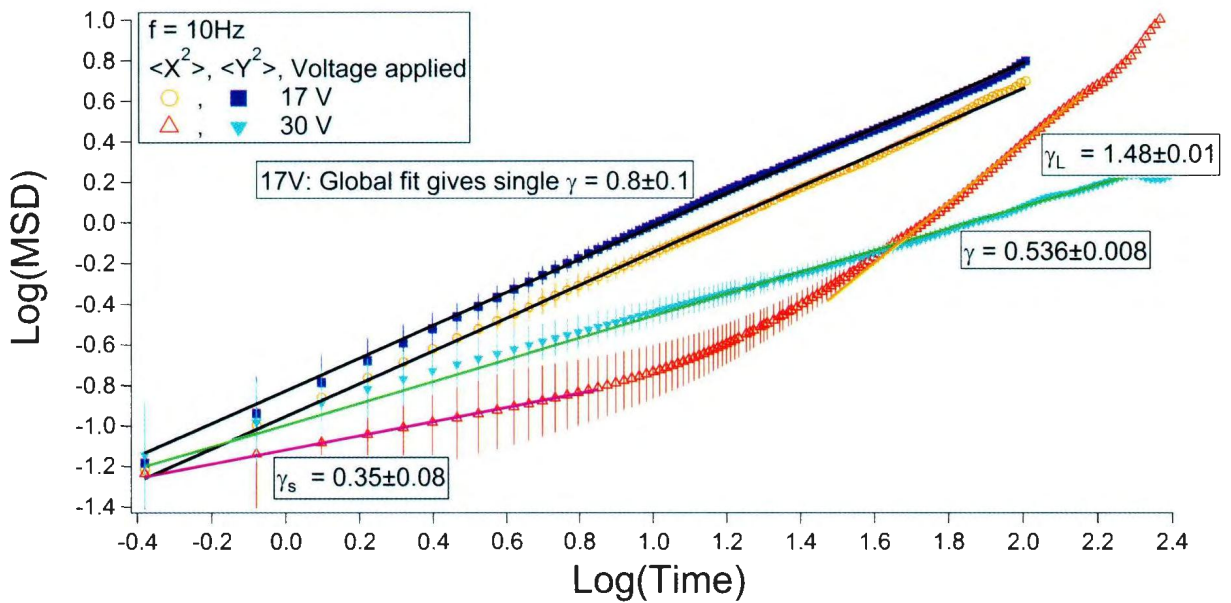
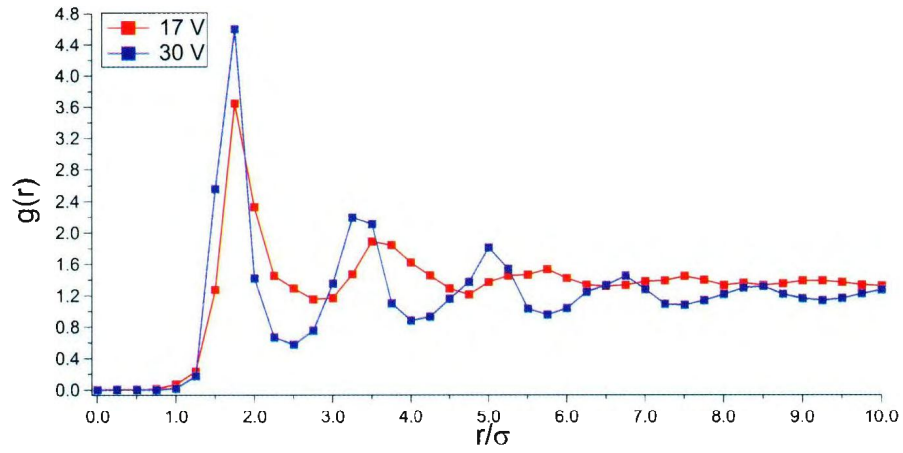
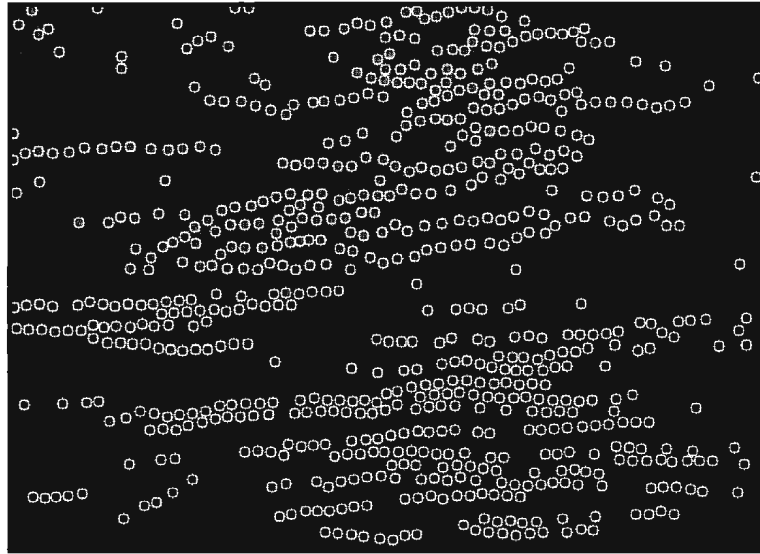


Figure 4.14: EH01, $f = 10\text{Hz}$ at electric fields of 17 and 30 V/mm. The 17 V/mm results exhibit sub-diffusive behaviour at all times with $\gamma = 0.8$. The 30 V/mm results (offset upward by 1 unit) show the $\langle Y^2 \rangle$ data exhibit sub-diffusive behaviour at all times while $\langle X^2 \rangle$ appears to have two linear regimes, at short times is sub-diffusive and at long times is super-diffusive.



(a)



(b)

Figure 4.15: (a) EH01, $f = 10$ Hz at electric fields of 17 and 30 V/mm. Pair correlation function shows a peak at $r/\sigma \sim 2$. The height of this peak increases as field increase, indicating that the chain stiffness increases.(b) Frames from sample EH01 at 10Hz at 17 V and 30 V, showing the onset of chain formation and well-formed chains respectively.

4.6 Sample EH02: Area Fraction $\alpha = 0.074$.

Experiments on sample EH02 were carried out using a camera capable of higher frame rates and with a 20x air objective, using fluorescence optical imaging and the experimental set up described in Section 3.5.

Once the conditions under which the sample was exposed were considered to have reached a steady state (typically 15 minutes) the data acquisition consisted of an image series of 1000 images at 30 frames/second. Results are reported first at zero electric field, and then for applied electric fields at different frequencies and amplitudes.

4.6.1 EH02: Zero Field

Figure 4.16 shows a plot of $\log(\text{MSD})$ vs $\log(\text{time})$ at zero field for sample EH02. From the linearity of this plot, we see that the scaling is $\text{MSD} = t^\gamma$. The linear behaviour is fitted to obtain an average value ($\gamma = 1.006 \pm 0.002$), which is consistent with normal diffusion ($\gamma = 1$).

Figure 4.17 shows the pair correlation for this sample at zero field. It shows no peak indicating that there is no structuring in the relatively dilute colloidal fluid. The 2-dimensional pair correlation functions show a broad crossover from zero to 1 because the 2D image projects out-of-focus particles, the result is a non-zero $g(r)$ even at $r < \sigma$.

Finally, at zero field, we plot the MSD vs time in figure 4.18. This relationship is linear, and from the slope we obtain the diffusion coefficients along the X and Y directions, with an average value $D_{NF}^{EH02} = 0.039 \pm 0.001 \mu\text{m}^2/\text{s}$. Comparing this

with $D_{SES} = 0.102 \mu\text{m}^2/\text{s}$, we see that this value is roughly half the expected bulk value. The reason for this slowing down was discussed in section 2.11 where it was pointed out that hydrodynamic interactions with a hard wall can slow down colloidal diffusion.

The faster camera enabled data to be captured at a higher frame rates, and a lower magnification objective was used enabling a larger field of view and therefore gaining better statistics. However, the sample itself was made from a different batch of colloidal suspension, and the ionic strength of the solvent mixture (which was determined after viewing data was taken via pair correlation function measurements) was found to be higher than that of EH01. Thus this second sample provided a window into the role of another experimental parameter, the ionic concentration or the related Debye length, on the colloidal dynamics.

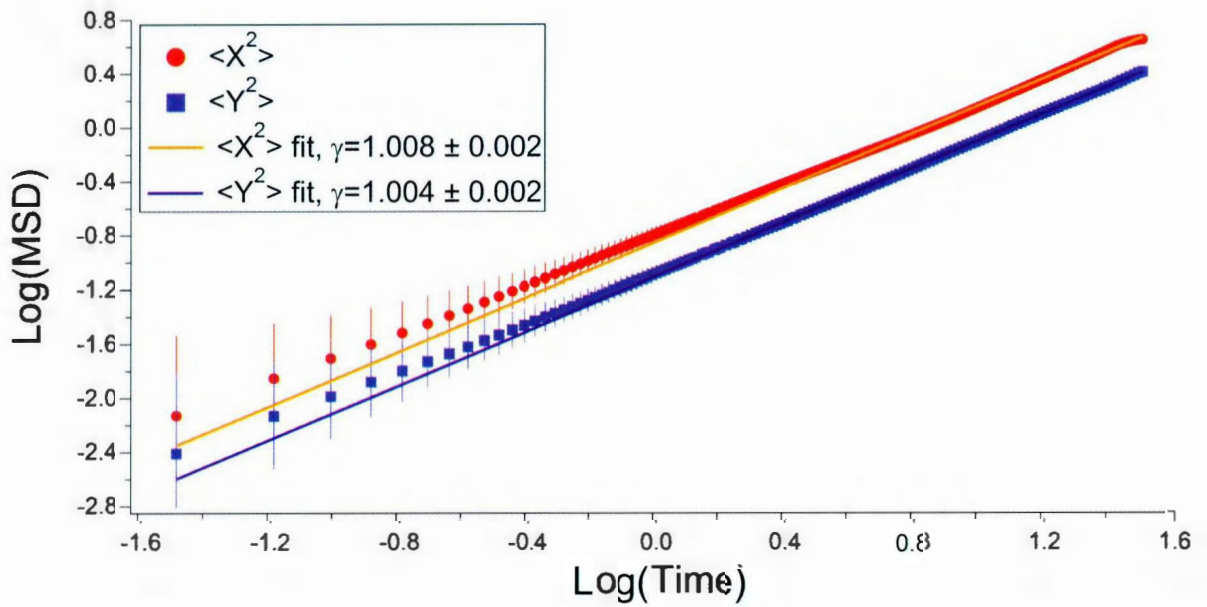


Figure 4.16: EH02, zero field. At zero field, the dynamics is diffusive: if one writes $MSD = t^\gamma$, then a linear fit to $\log(MSD)$ vs $\log(t)$ yields a slope $\gamma = 1.004 \pm 0.002$ which is consistent with $\gamma = 1$. $\langle X^2 \rangle$ is offset by 0.25 for better visualization.

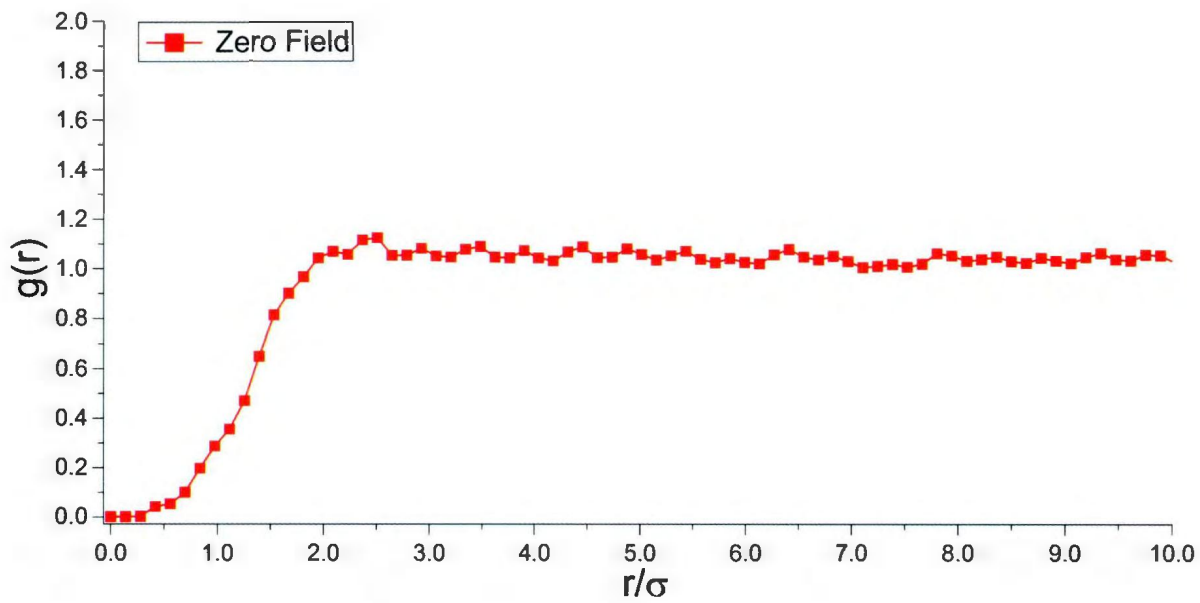


Figure 4.17: EH02, zero field. Pair correlation function shows no peak, indicative of fluid-like structure expected for dilute colloidal suspensions.

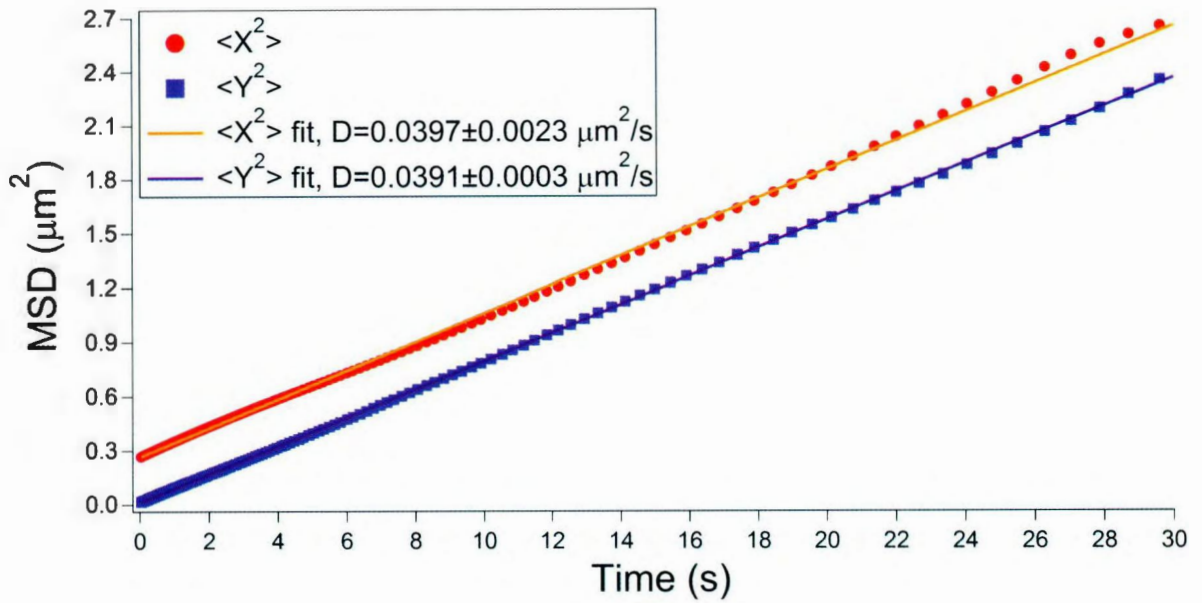


Figure 4.18: EH02, zero field. Mean square displacement ($\langle X^2 \rangle$, $\langle Y^2 \rangle$) versus time is linear, and yields an experimental diffusion coefficient of $D_{NF}^{EH02} = 0.0394 \pm 0.0002 \mu\text{m}^2/\text{s}$. $\langle X^2 \rangle$ is offset by 0.25.

4.6.2 Unwanted Particle Drift at High Voltages

When the movies acquired were later reviewed, it was noticed that there was fluid flow in the sample at higher voltages. To visualize this, at each frequency and field strength a sub-stack was made with 1 frame per cycle. In this stroboscopic sub-stack movie, the directed motion is removed, so what is left is diffusive motion. Drift was detectable as a subtle directed motion, typically along a direction uncorrelated with the applied field. All the images in this substack can then be averaged. Figure 4.19 shows a montage of these averaged images as a function of frequency and applied voltage. Each row corresponds to a different frequency with each column corresponding to different voltages there were applied to the cell. Each image is a average of the sub-stack and is a zoomed in area highlighting only a few particles to see if there was indeed drift. A particle that is not drifting is seen as a solid circular object, while a drifting particle is seen as a blurred particle track. Images acquired at applied voltages and frequencies to the right of the red line were determined to be drifting - these datasets were discarded from further analysis.

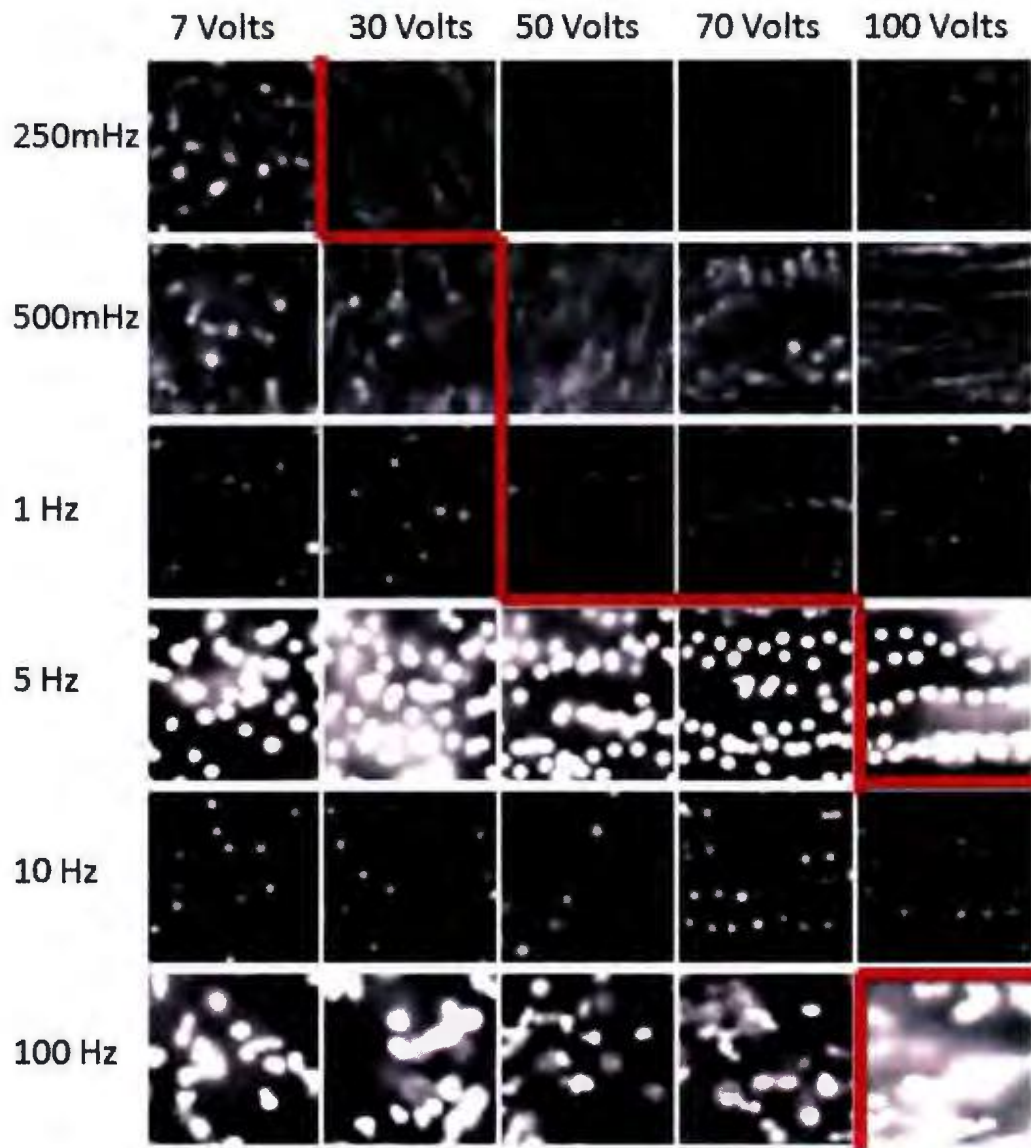


Figure 4.19: The average of several frames sampled stroboscopically at the frequency of the applied field yields information about drift. Solid white circles are roughly static due to the stroboscopic sampling which renders the oscillatory motion invisible. Any left over drift manifests itself as a blurred particle track. This drift was observed to occur for experimental conditions (applied voltage and frequency) to the right of the red line.

4.6.3 EH02: $f = 250$ mHz

Figure 4.20 shows a plot of $\log(\text{MSD})$ vs $\log(\text{time})$ at 250 mHz with a voltage of 7 volts ($E_0 = 7$ V/mm) to sample EH02. The data for $\langle Y^2 \rangle$ appears to have roughly a linear behaviour to the eye with $\gamma \sim 1$ at all times. $\langle Y^2 \rangle$ data appears to alternate from slightly larger than to slightly less than 1. The data for $\langle X^2 \rangle$ at short times, $2 > \gamma > 1$ meaning that the colloidal are being move with not only Brownian motion but with some additional force (the applied electric field) and trending to $\gamma = 1$. It should be noted that at the end of every cycle of the applied electric field, the $\langle X^2 \rangle$ data returns to the $\langle Y^2 \rangle$ data.

Figure 4.21 shows the pair correlation for this sample at zero field shows no peak indicating that is no structure.

Finally, at this field strength, we plot the MSD vs time in figure 4.22. This relationship is linear along $\langle Y^2 \rangle$, and from the slope we obtain the diffusion coefficients, $D_{250\text{mHz}}^{EH02} = 0.039 \pm 0.001 \mu\text{m}^2/\text{s}$. Compared this with $D_{SES} = 0.102 \mu\text{m}^2/\text{s}$, we see that this value is roughly half the expected bulk value. The reason for this slowing down was discussed in section 2.11 where it was pointed out that hydrodynamic interactions with a hard wall can slow down colloidal diffusion, this will be discussion later on in chapter 5 section 5.4.1.1.

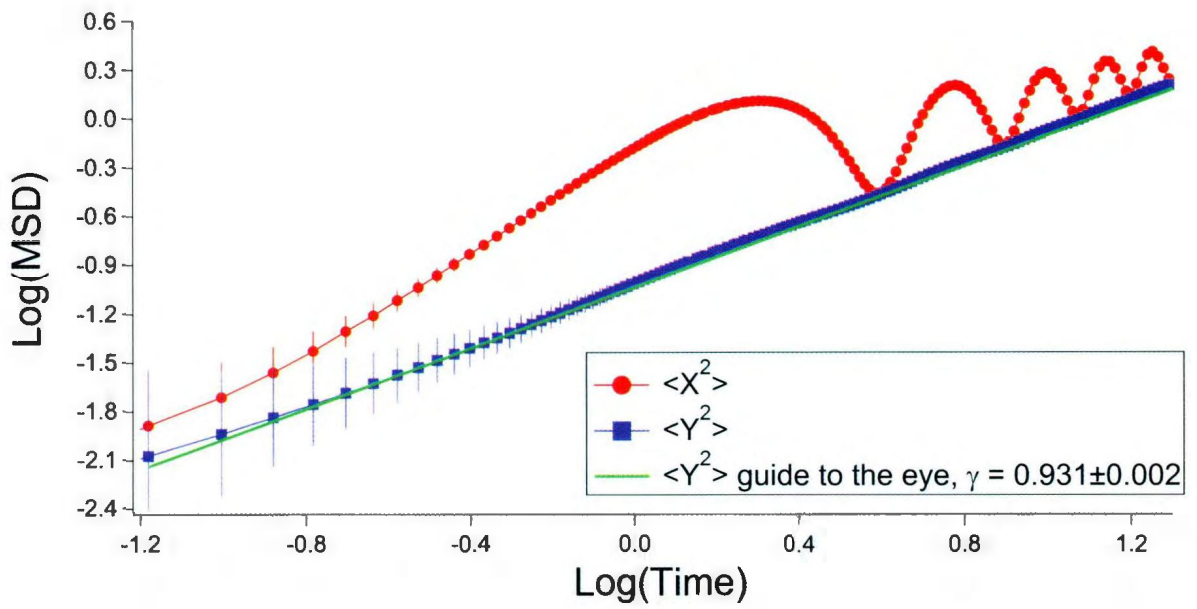


Figure 4.20: EH02, 250 mHz at electric fields of 7 V/mm. The results show linear behaviour in Y

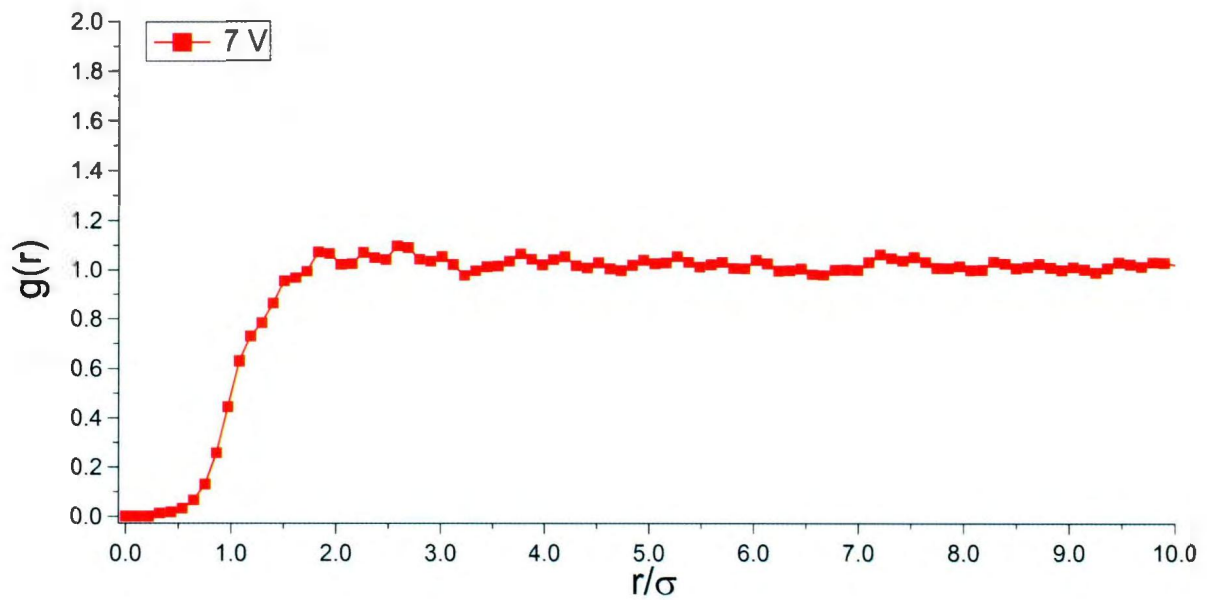


Figure 4.21: EH02, 250 mHz at electric fields of 7 V/mm. Pair correlation function shows no peak, indicating no structuring of colloids.

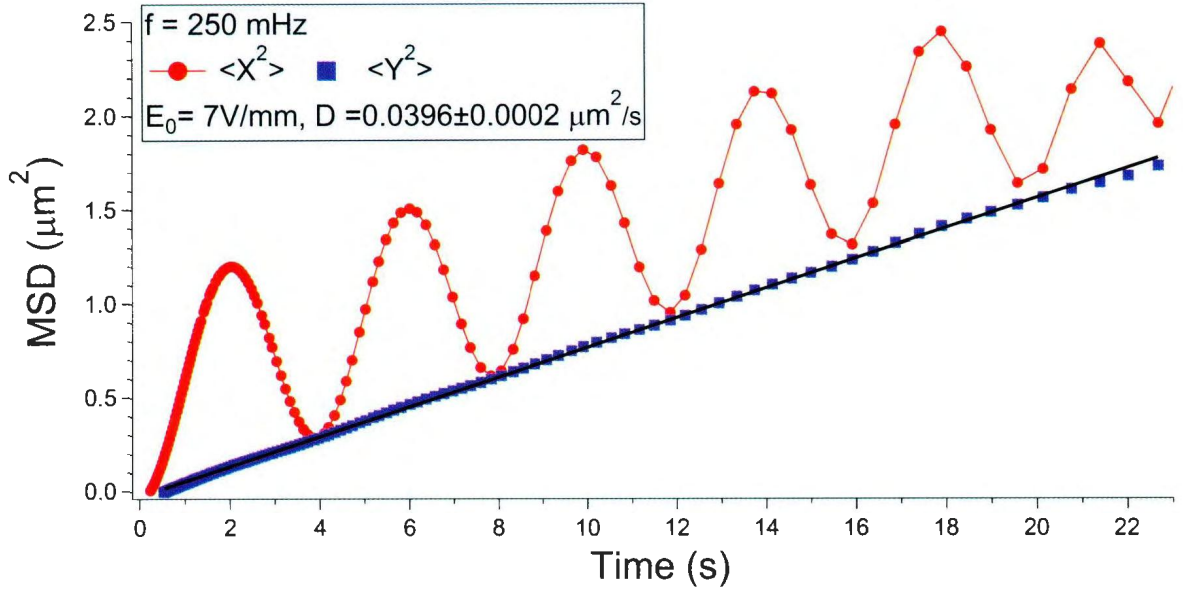


Figure 4.22: EH02, $f = 250\text{mHz}$ with 7V/mm . $\langle Y^2 \rangle$ versus time is linear, and yields an experimental diffusion coefficient of $D_{250\text{mHz}}^{EH02} = 0.039 \pm 0.0002\mu\text{m}^2/\text{s}$.

4.6.4 EH02: $f = 500\text{ mHz}$

Figure 4.23 shows a plot of $\log(\text{MSD})$ vs $\log(\text{time})$ at 250 mHz with a voltage of 7 volts and 30 V ($E_0 = 7$ and 30 V/mm). The data for $\langle Y^2 \rangle$ at the lowest voltage appears to have a linear behaviour with $\gamma \sim 1$ at all times, which is consistent with normal diffusion. The data for $\langle X^2 \rangle$ at both 7 V/mm and 30 V/mm follow a similar trend as at 250mHz where the data oscillates at the applied frequency of the applied electric field.

At 7 V/mm , the oscillation of the $\langle X^2 \rangle$ data appears to uncoupled $\langle Y^2 \rangle$, because the minima of the oscillatory motion coincides with the Y diffusion. The data for $\langle Y^2 \rangle$ at the higher field strength appears to be affected by the motion along X , causing a change in the slope of $\langle Y^2 \rangle$ at the higher voltage at long time.

Figure 4.24 shows the pair correlation for this sample at the same two field

strengths. It should be noted that this plot shows no peak, indicating that is is no structure.

Since the results along the Y direction at 7V/mm in Figure 4.23 are consistent with $\gamma = 1$, we can extract the diffusion coefficient from a plot of MSD vs. time, shown in figure 4.25. We obtain the diffusion coefficients along the Y direction, $D_{500\text{mHz}}^{EH02} = 0.039 \pm 0.001 \mu\text{m}^2/\text{s}$. Again comparing this with $D_{SES} = 0.102 \mu\text{m}^2/\text{s}$, we see that this value is roughly half the expected bulk value. This will be discussion later on in chapter 5 section 5.4.1.1.

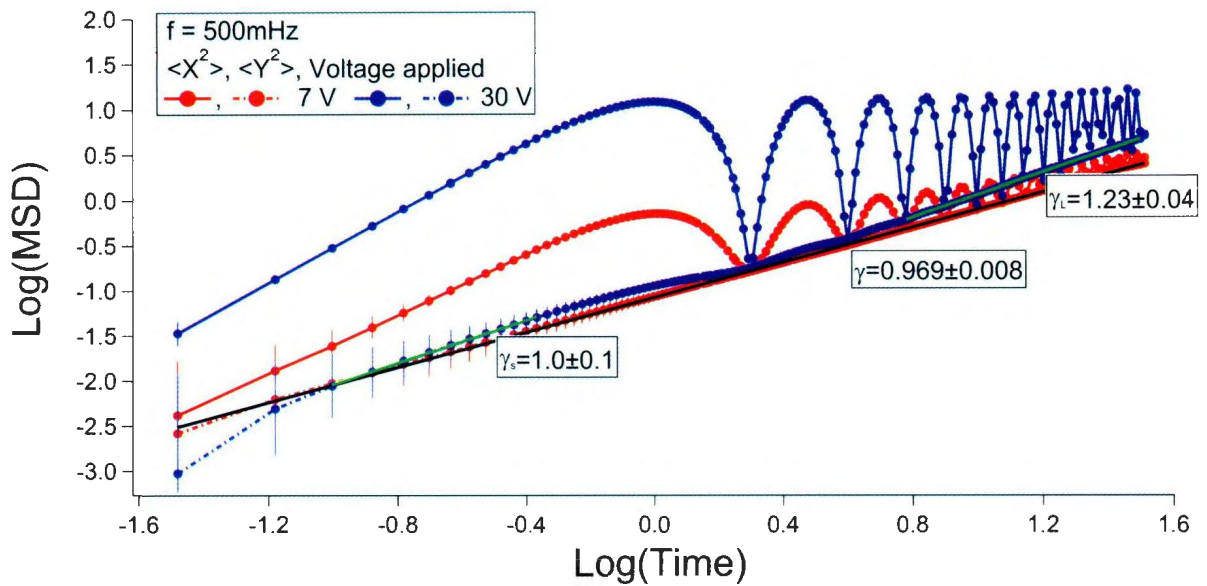


Figure 4.23: EH02, 500 mHz at electric fields of 7 and 30 V/mm. The results show linear behaviour in Y at 7 V/mm. . At 30 V/mm, the MSD appears to show a subtle $\gamma > 1$ behaviour.

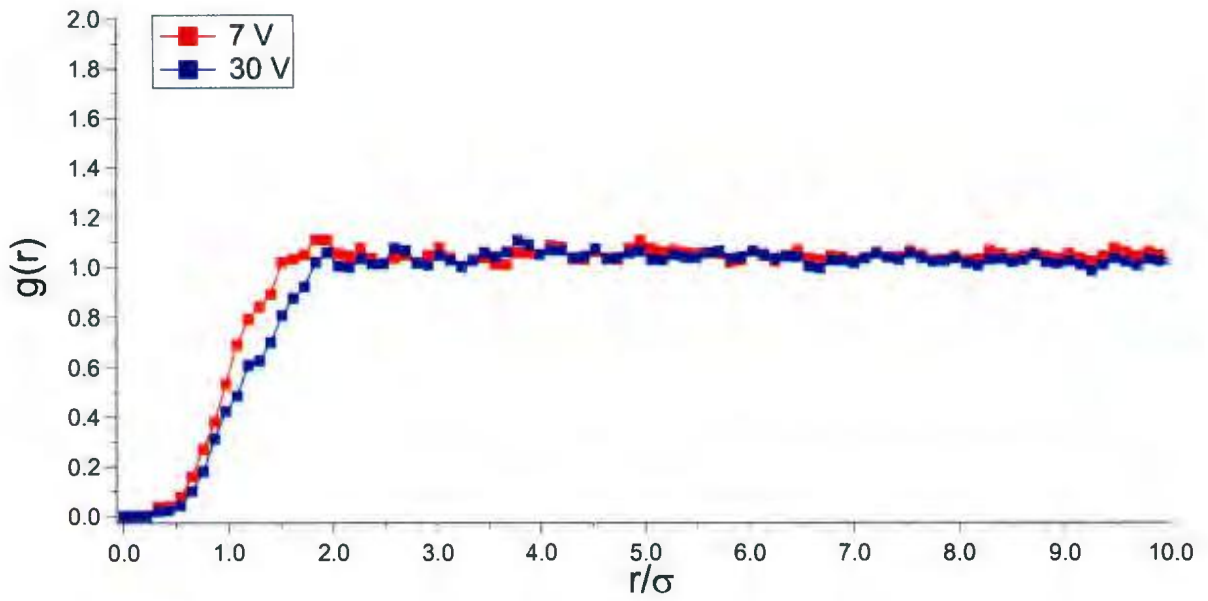


Figure 4.24: EH02, 500 mHz at electric fields of 7 and 30 V/mm. Pair correlation function shows no peak, indicating no structuring of colloids.

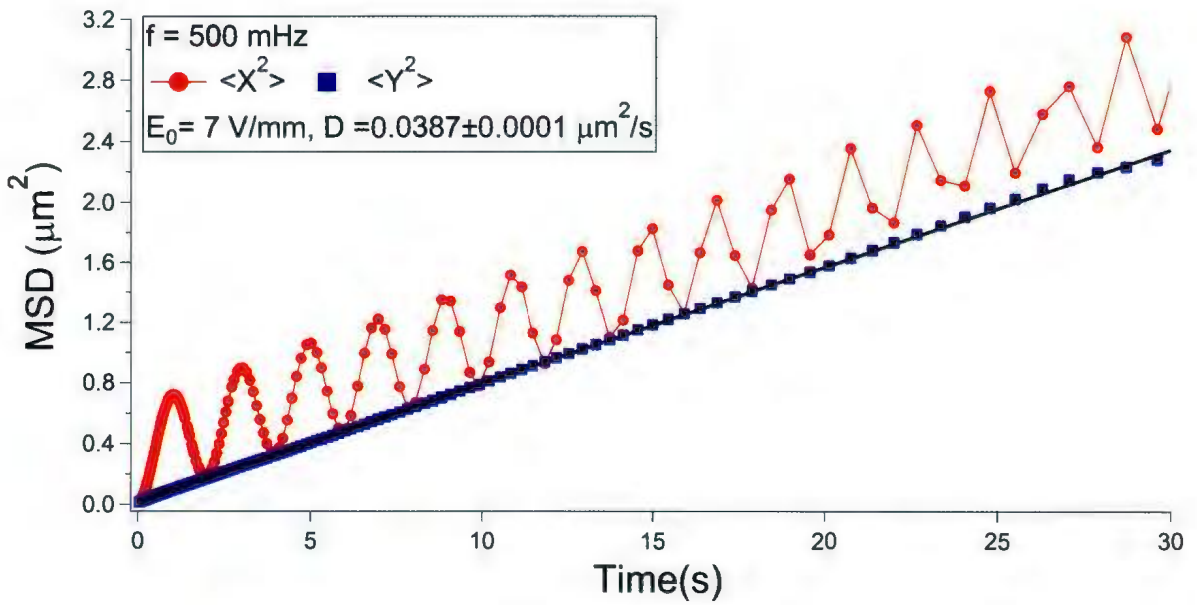


Figure 4.25: EH02, $f = 500\text{mHz}$ with 7V/mm . $\langle Y^2 \rangle$ versus time is linear, and yields an experimental diffusion coefficient of $D_{500\text{mHz}}^{EH02} = 0.039 \pm 0.0001 \mu\text{m}^2/\text{s}$.

4.6.5 EH02: $f = 1$ Hz

Figure 4.26 shows a plot of $\log(\text{MSD})$ vs $\log(\text{time})$ at 1 Hz with voltages ranging from 7 V to 30 V ($E_0 = 7$ to 30 V/mm). Again, the dynamics along X exhibits oscillatory behaviour that appears decoupled with diffusive motion, except at the highest field studied (similar to the 500 mHz case). Figure 4.27 show a plot of the $\log(\langle Y^2 \rangle)$ vs $\log(\text{time})$ at the different voltages with slopes at both short and long times, At 7 and 30 V/mm, $\gamma \sim 1$ at all times, which is consistent with normal diffusion. At 50V/mm and long times, the dynamics is noticeable super-diffusive, more so than at 500 mHz.

The pair correlations, shown in figure 4.28, show little field-induced structuring.

For $E_0 = 7$ and 30 V/mm, we extract the diffusion coefficient along Y from a plot of MSD vs. time, shown in figure 4.29. We obtain the diffusion coefficients along the Y direction, $D_{1\text{Hz}}^{EH02} = 0.036 \pm 0.001 \mu\text{m}^2/\text{s}$. Again comparing this with $D_{SES} = 0.102 \mu\text{m}^2/\text{s}$, we see that this value is roughly one-third the expected bulk value.

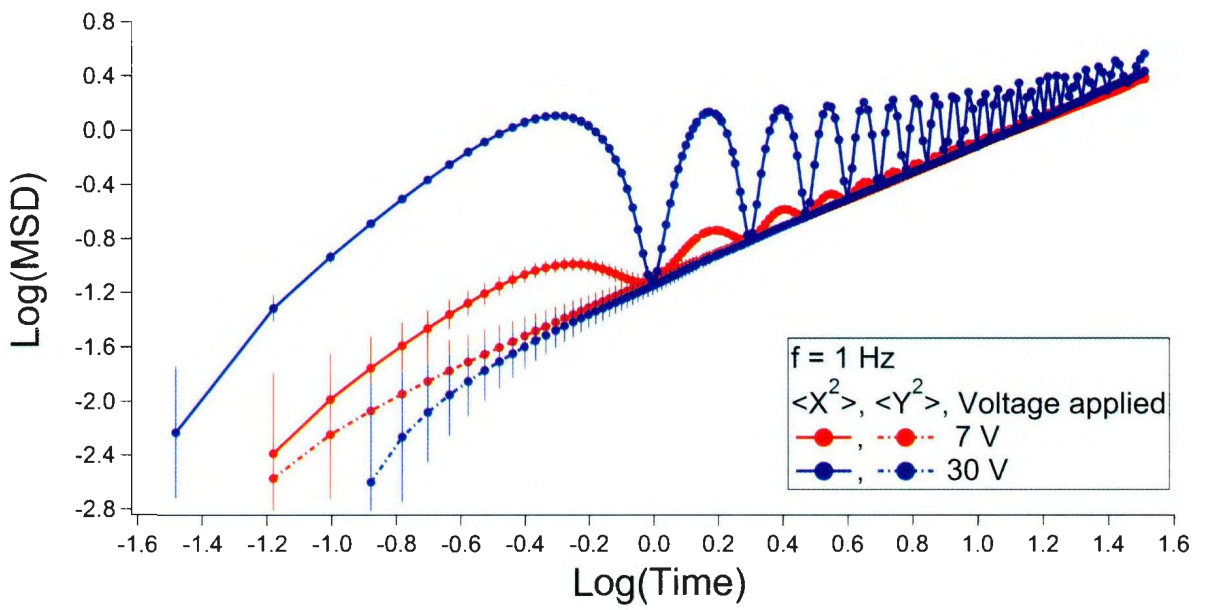


Figure 4.26: EH02, 1 Hz at electric fields ranging from 7 to 30 V/mm.

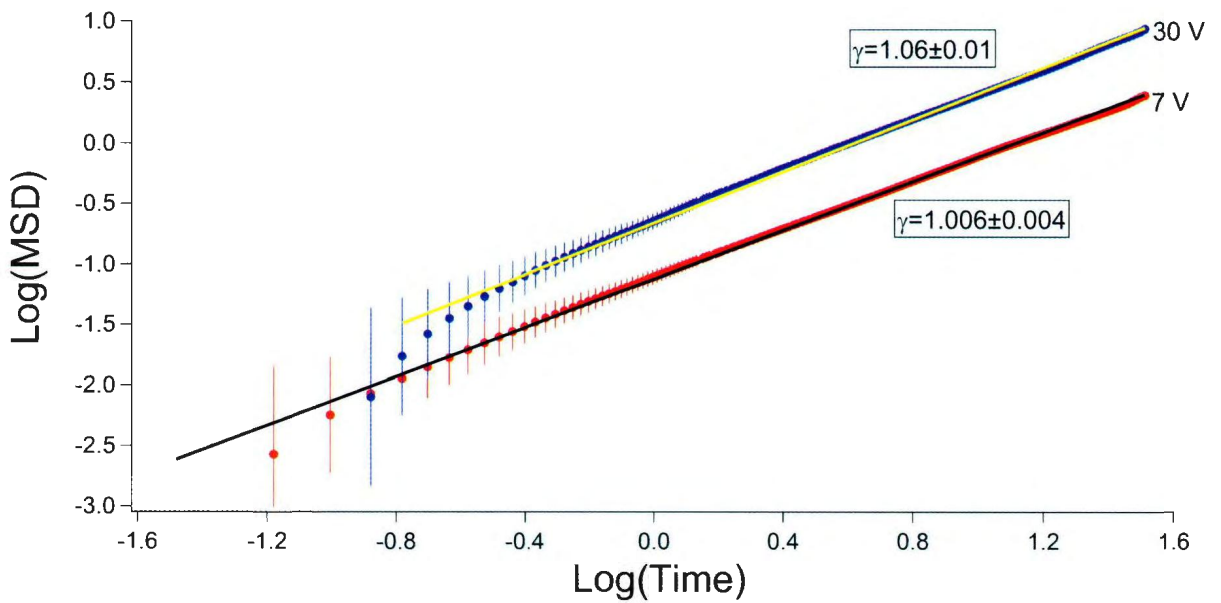


Figure 4.27: EH02, 1 Hz at electric fields ranging from 7 to 30 V/mm. $\langle Y^2 \rangle$ data only. Each voltage offset from the previous voltage by 0.25 unit.

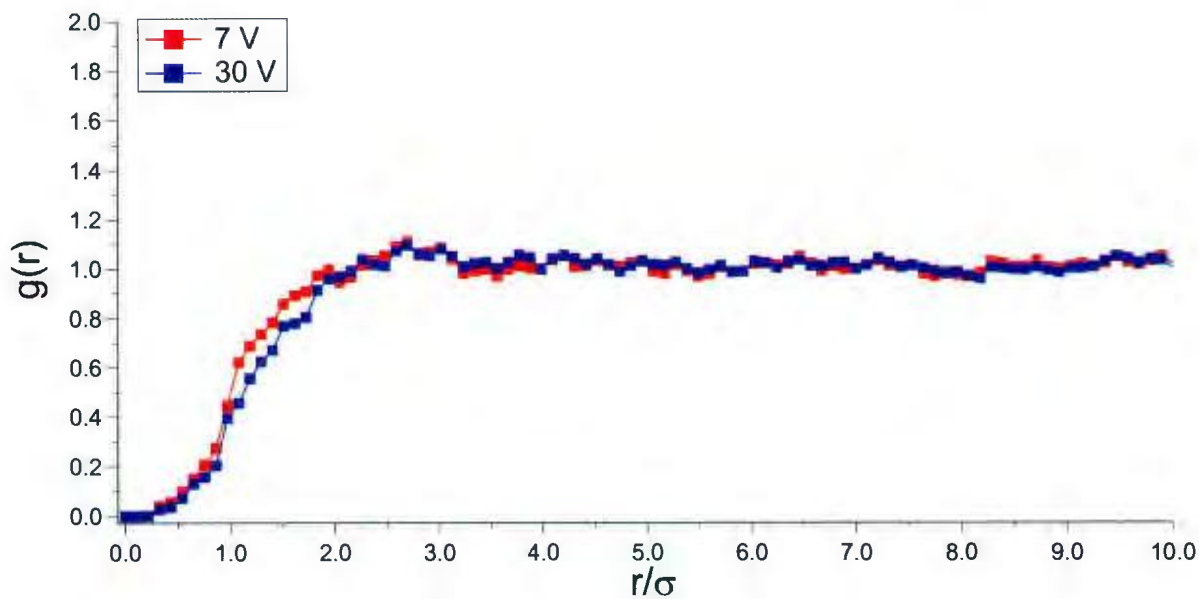


Figure 4.28: EH02, 1 Hz at electric fields ranging from 7 to 30 V/mm. Pair correlation function shows no peak at low voltages only at the highest voltage.

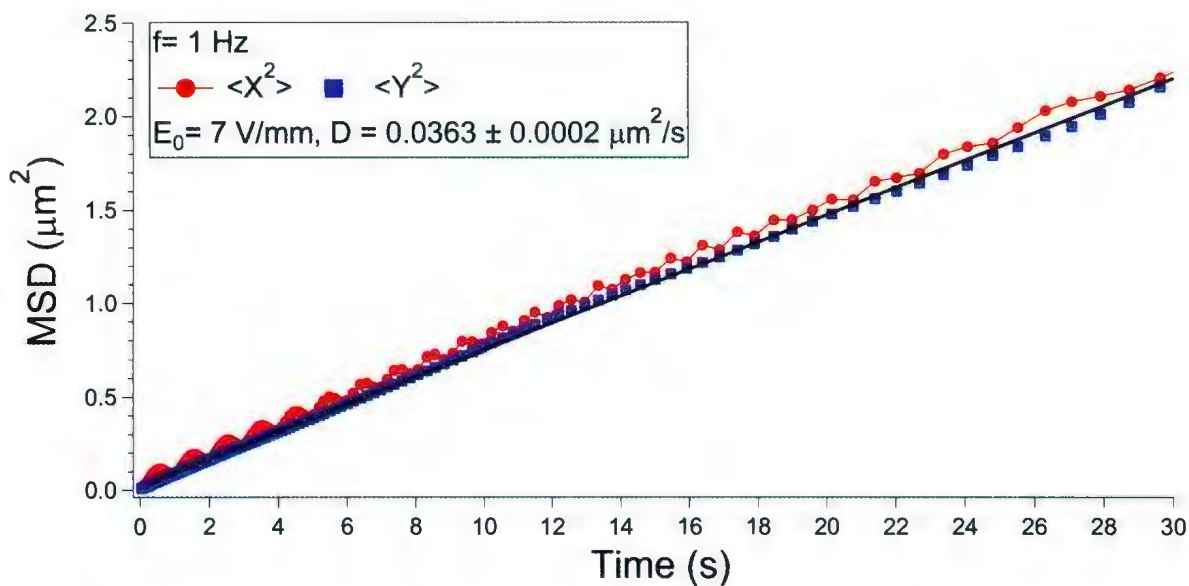


Figure 4.29: EH02, $f = 1 \text{ Hz}$ with 7 V/mm . $\langle y^2 \rangle$ versus time is linear, and yields an experimental diffusion coefficient of $D_{1\text{Hz}}^{\text{EH02}} = 0.036 \pm 0.0001 \mu\text{m}^2/\text{s}$.

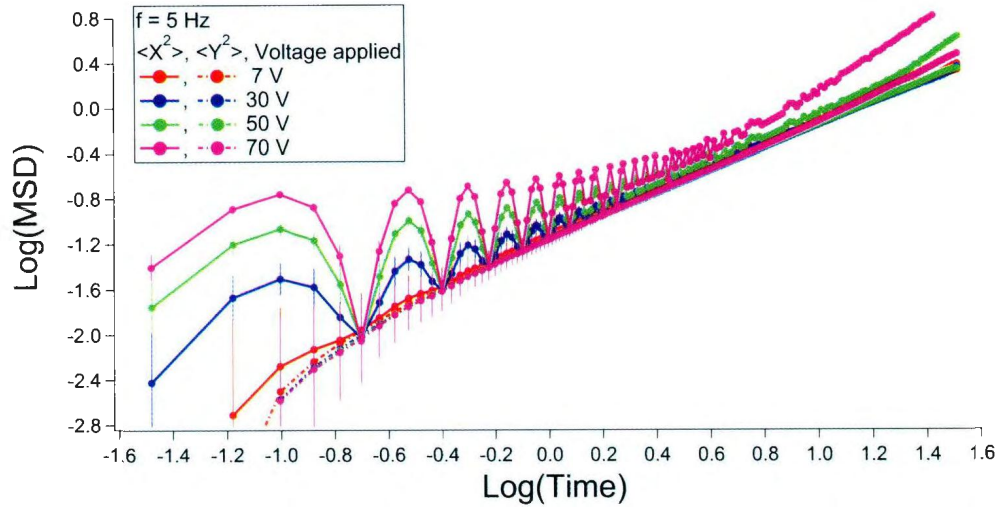
4.6.6 EH02: $f = 5$ Hz

Figure 4.30(a) shows a plot of $\log(\text{MSD})$ vs $\log(\text{time})$ at 5 Hz with voltages ranging from 7 V to 70 V ($E_0 = 7$ to 70 V/mm). The behaviour here is similar to that at $f = 1$ Hz. There is normal diffusion in Y (shown clearly in Figure 4.30(a), where the Y dynamics is fit to a power law γ of 1). Along X, there is the familiar “Normal + Oscillatory” behaviour, except at long times at the highest field, where the dynamics appears super-diffusive.

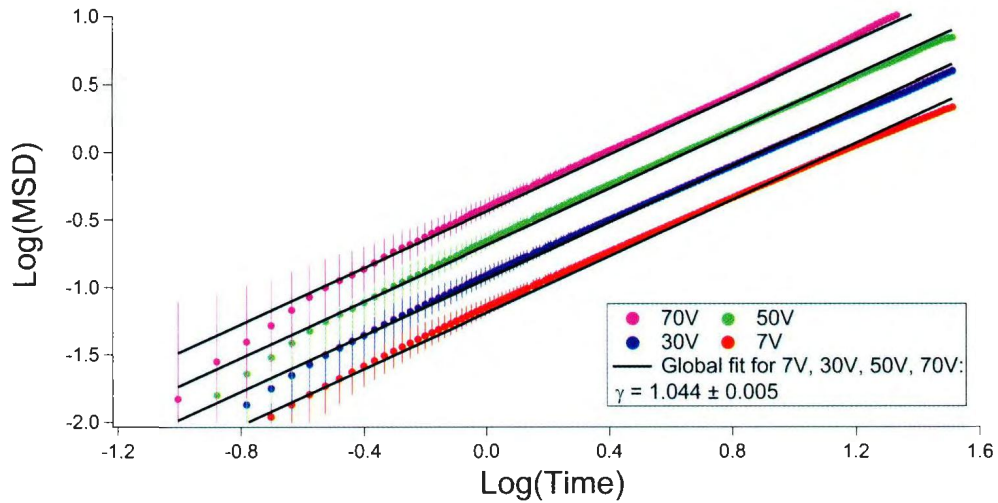
The global fitting was done by restricting the slopes to be the same but leaving the y-intercept free.

Figure 4.31(a) shows the pair correlation for this sample at the same field strengths. It should be noted that this plot shows a peak at around $r/\sigma \sim 2$ with the height ranging from 1.2 to 1.9. indicating that is weak structure.

Since the results along the Y direction at 7 V/mm in Figure 4.30(b) are consistent with $\gamma = 1$, we can extract the diffusion coefficient from a plot of MSD vs. time, shown in figure 4.32. We obtain the diffusion coefficients along the Y direction, $D_{5Hz}^{EH02} = 0.0332 \pm 0.0001 \mu\text{m}^2/\text{s}$. Again comparing this with $D_{SES} = 0.102 \mu\text{m}^2/\text{s}$, we see that this value is roughly one-third the expected bulk value.

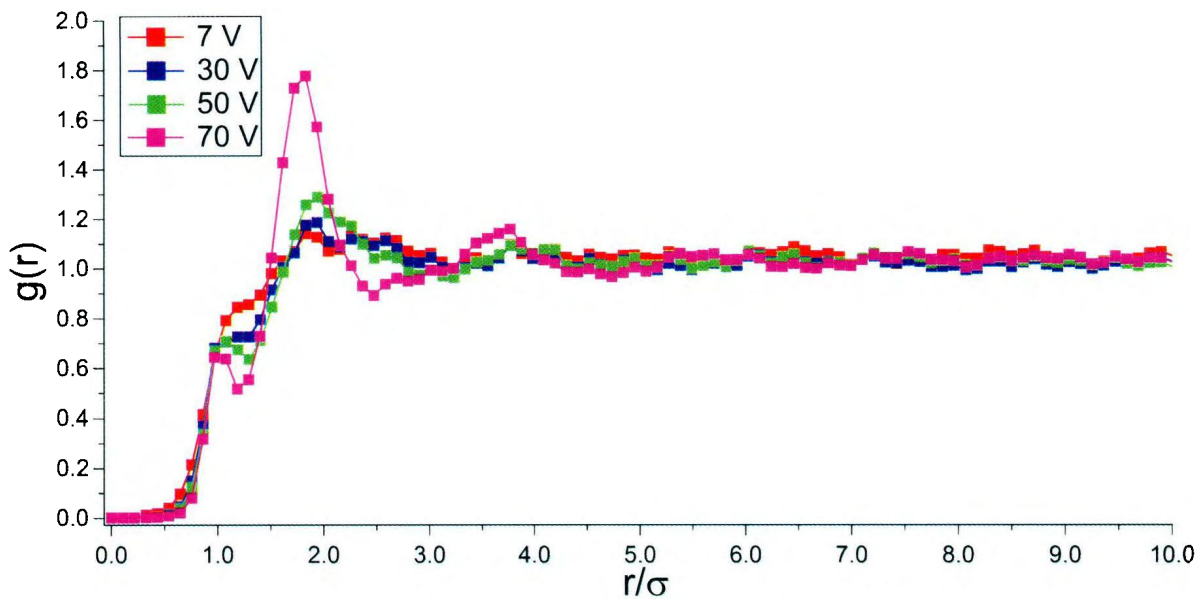


(a)

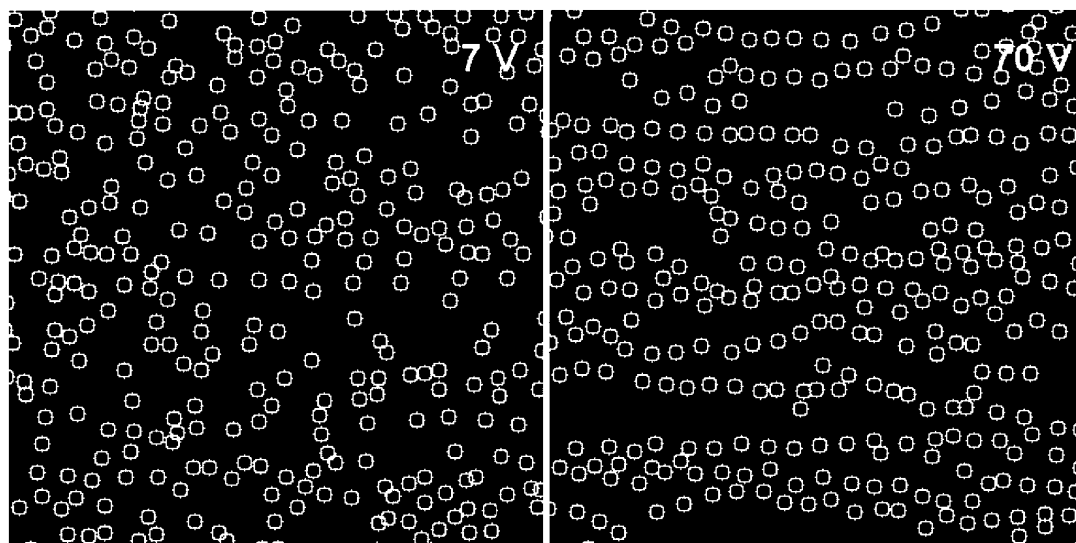


(b)

Figure 4.30: (a) EH02, 5 Hz at electric fields ranging from 7 to 70 V/mm. The dynamics along X shows oscillatory motion superimposed on diffusive dynamics at short times; this diffusive dynamics is seen for all times along Y. At high fields and long times, the motion along X is faster than diffusive.(b) EH02, 5 Hz at electric fields ranging from 7 to 70 V/mm. $\langle Y^2 \rangle$ data only. Each voltage offset from the previous voltage by 0.25 unit. The dynamics along $\langle Y^2 \rangle$ is seen to be diffusive at all field amplitudes.



(a)



(b)

Figure 4.31: (a) EH02, 5Hz with electric fields ranging from 7 to 70 V/mm. Pair correlation function shows a peak at $r/\sigma \sim 2$. The height of this peak is ranges from 1.2 to 1.9, indicating some structuring only at the highest field (70V/mm). (b) Frames from sample EH02 at 5Hz at 7 V and 70 V, showing the onset of chain formation and formed chains respectively.

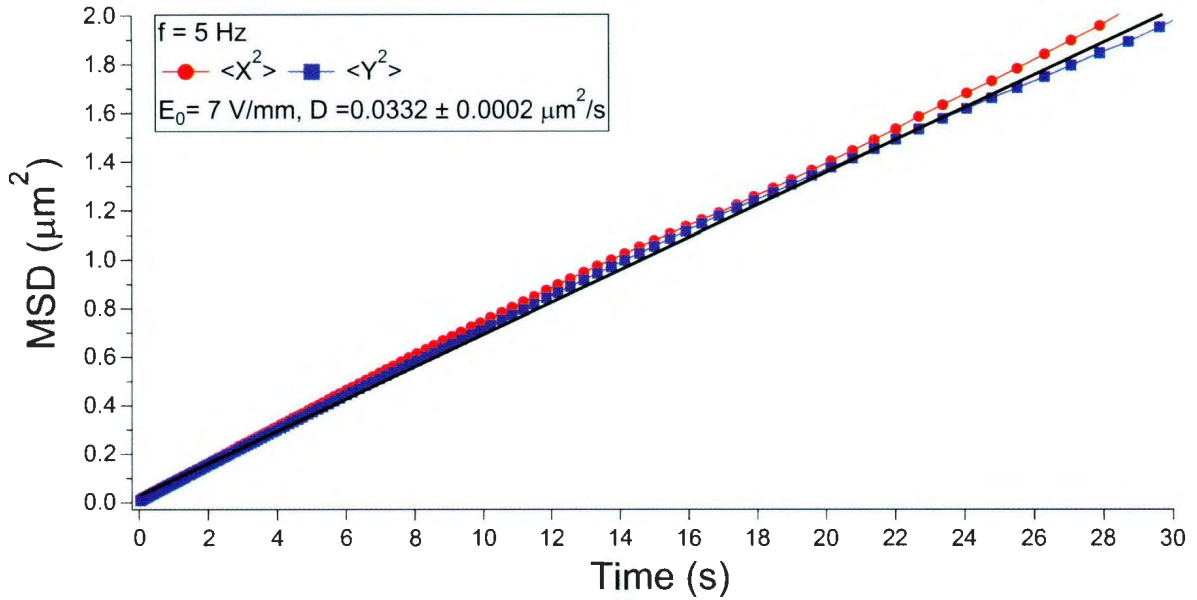


Figure 4.32: EH02, $f = 5\text{Hz}$ with 7V/mm . $\langle Y^2 \rangle$ versus time is linear, and yields an experimental diffusion coefficient of $D_{5\text{Hz}}^{EH02} = 0.0332 \pm 0.0001 \mu\text{m}^2/\text{s}$.

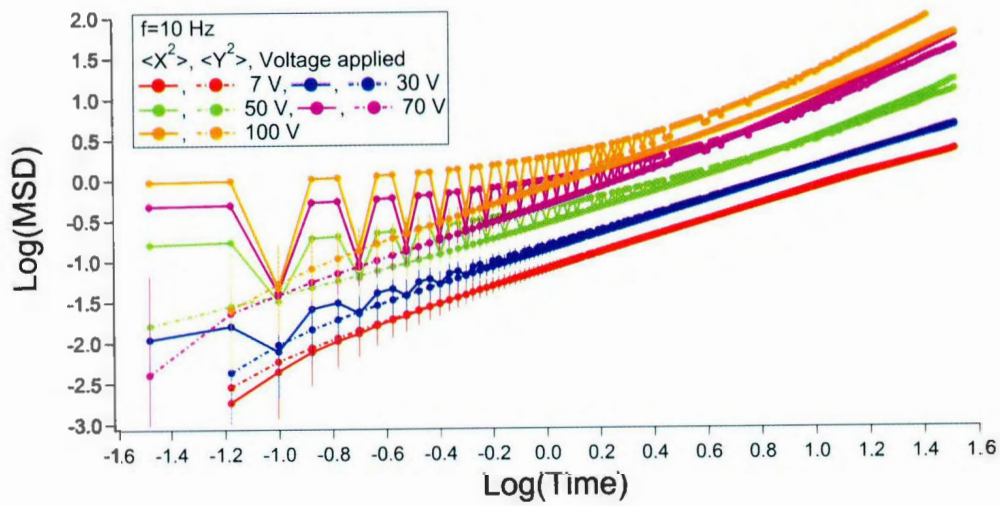
4.6.7 EH02: $f = 10 \text{ Hz}$

Figure 4.33(a) shows a plot of $\log(\text{MSD})$ vs $\log(\text{time})$ at 10 Hz with voltages ranging from 7 V to 100 V ($E_0 = 7$ to 100 V/mm). $\langle X^2 \rangle$ at all voltages follows a similar trend as at 250mHz , with sinusoidal oscillations (not very well resolved as we only acquire 3 frames per cycle) at the applied frequency of the applied electric field. At 7 V/mm , 30 V/mm and 50 V/mm , the oscillation appears uncoupled with normal diffusive motion. The data for $\log \langle Y^2 \rangle$ vs $\log(\text{time})$ at the higher field strength appears to be affected by the motion along X , causing a change in slope at the higher voltage. At the 3 lowest fields applied, $\log(\langle Y^2 \rangle)$ exhibits linear diffusive ($\gamma \sim 1$) behaviour, which will be looked at more carefully in figure 4.33(b). Figure 4.33(b) shows a plot of the $\log(\langle Y^2 \rangle)$ vs $\log(\text{time})$ at the different applied fields with fits at

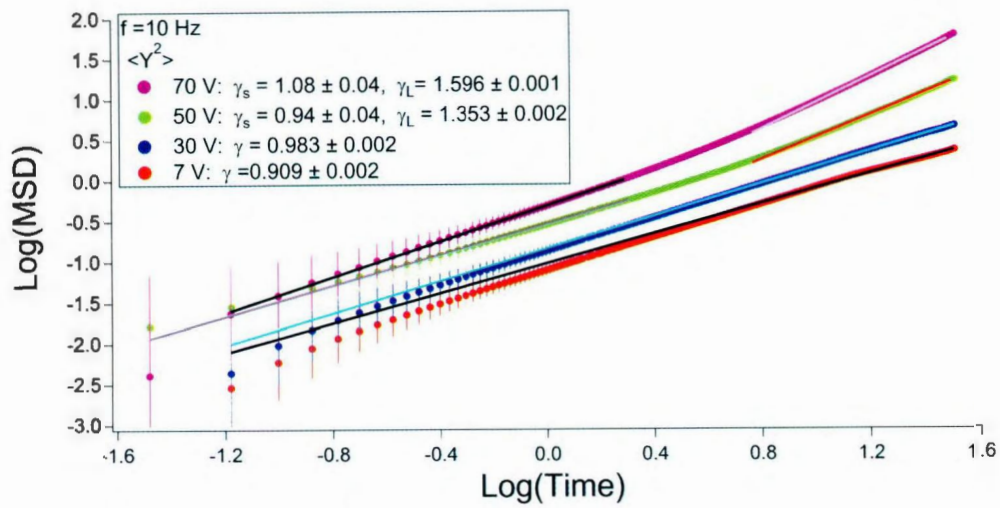
short and long time for 70V and 50V, and single fits for 30V and 7V were $\gamma \sim 1$ at all times, which is consistent with normal diffusion.

Figure 4.34 shows the pair correlation for this sample at the same field strengths. It should be noted that this plot shows a peak at around $r/\sigma \sim 2$ with the height ranging from 1.2 to 2.3. indicating that is weak structure at the lower voltages but noticeable structure at 30, 50, and 70 V/mm.

Since the results along the Y direction at 7 V/mm in figure 4.33(b) are consistent with $\gamma = 1$, we can extract the diffusion coefficient from a plot of MSD vs. time, shown in figure 4.35. We obtain the diffusion coefficients along the Y direction, $D_{10Hz}^{EH02} = 0.035 \pm 0.001 \mu\text{m}^2/\text{s}$. Again comparing this with $D_{SES} = 0.102 \mu\text{m}^2/\text{s}$, we see that this value is roughly one-third the expected bulk value. This will be discussion later on in chapter 5 section 5.4.1.1.



(a)



(b)

Figure 4.33: (a)EH02, 10 Hz at electric fields ranging from 7 to 100 V/mm. At these largest fields, and at long times, the dynamics is faster than diffusive along the field direction, and to a lesser extent, perpendicular to the field direction as well. (b) EH02, 10 Hz at electric fields ranging from 7 to 100 V/mm. $\langle Y^2 \rangle$ data only. Each voltage offset from the previous voltage by 0.25 unit. At short times, the dynamics is diffusive. At the largest fields, and at long times, the dynamics is faster than diffusive.

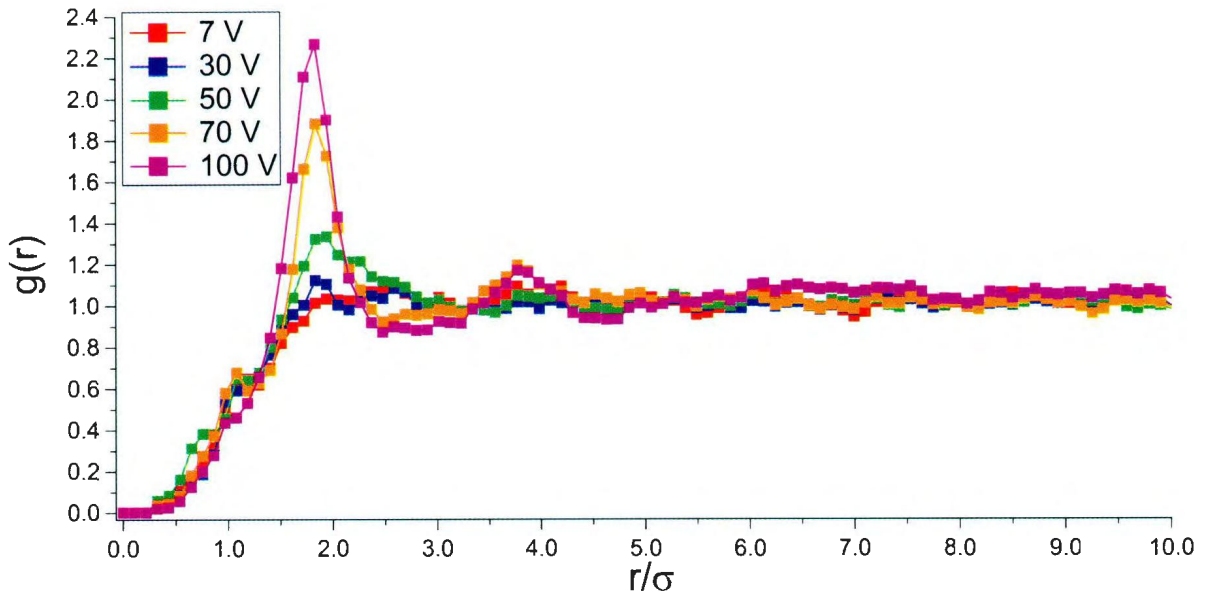


Figure 4.34: EH02, 10Hz with voltages ranging from 7 to 100. Pair correlation function shows a peak at $r/\sigma \sim 2$. The height of this peak is ranges from 1.2 to 2.3. indicating that is weak structure at the lower voltages but at the higher voltage there is much stronger structure.

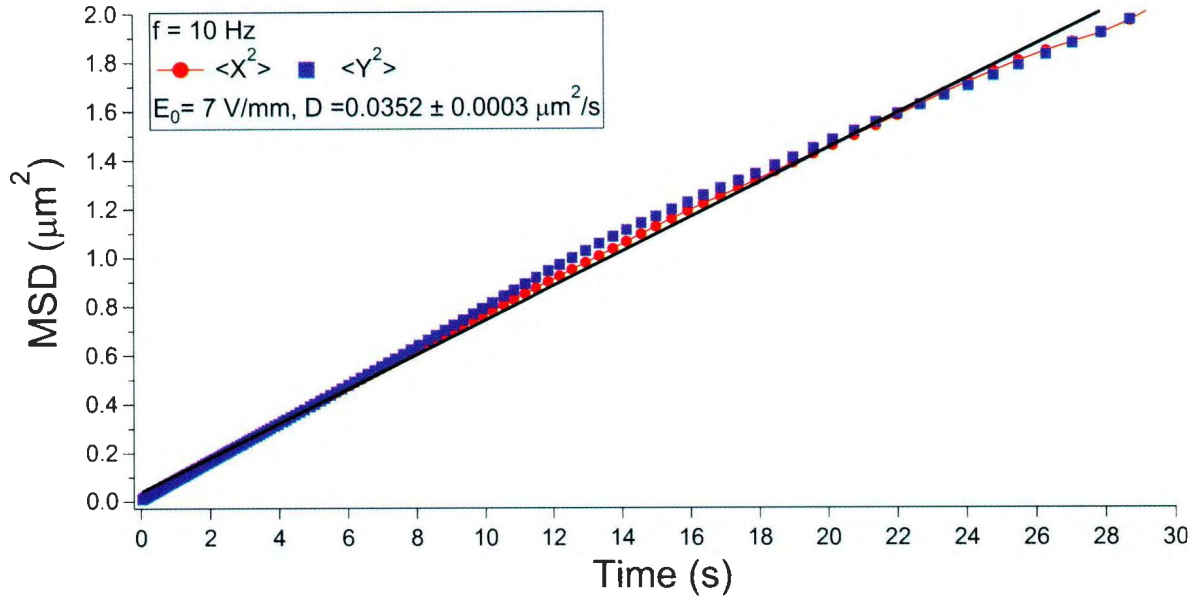


Figure 4.35: EH02, $f = 10\text{Hz}$ with $7\text{V}/\text{mm}$. $\langle y^2 \rangle$ versus time is linear, and yields an experimental diffusion coefficient of $D_{10\text{Hz}}^{\text{EH02}} = 0.035 \pm 0.0003\mu\text{m}^2/\text{s}$.

4.6.8 EH02: $f = 100\text{ Hz}$

Figure 4.36 shows a plot of $\log(\text{MSD})$ vs $\log(\text{time})$ at 100 Hz with voltages ranging from 7 V to 70 V ($E_0 = 7$ to $70\text{ V}/\text{mm}$) for sample EH02. The data for both $\langle X^2 \rangle$ and $\langle Y^2 \rangle$ at all voltages have a linear behaviour. This linear behaviour is fitted to obtain an average value ($\gamma = 1.00 \pm 0.01$), which is consistent with normal diffusion ($\gamma = 1$).

Figure 4.37(a) shows the pair correlation for this sample at $f = 100\text{ Hz}$ at electric fields ranging from 7 to $70\text{ V}/\text{mm}$. The pair correlation function shows no peak, indicating no structuring of colloids. The absence of structuring at $f = 100\text{ Hz}$ (which can be seen in figure 4.37(b) which is a montage from single frames of tracked data at 7V , 30V and 70V) for the field amplitudes less than $100\text{ V}/\text{mm}$ brings up an

interesting point. At these frequencies, the field likely oscillates too rapidly to polarize the ionic double layer, and the dielectric polarization mechanism is too weak to induce chain formation. This is an indication that the structuring at low frequencies is almost entirely due to the ionic polarization mechanism

Since the results along the Y direction at 7 V/mm in Figure 4.36 are consistent with $\gamma = 1$, we can extract the diffusion coefficient from a plot of MSD vs. time, shown in figure 4.38. We obtain the diffusion coefficients along the Y direction, $D_{100Hz}^{EH02} = 0.038 \pm 0.0002 \mu\text{m}^2/\text{s}$. Again comparing this with $D_{SES} = 0.102 \mu\text{m}^2/\text{s}$, we see that this value is roughly one-third the expected bulk value.

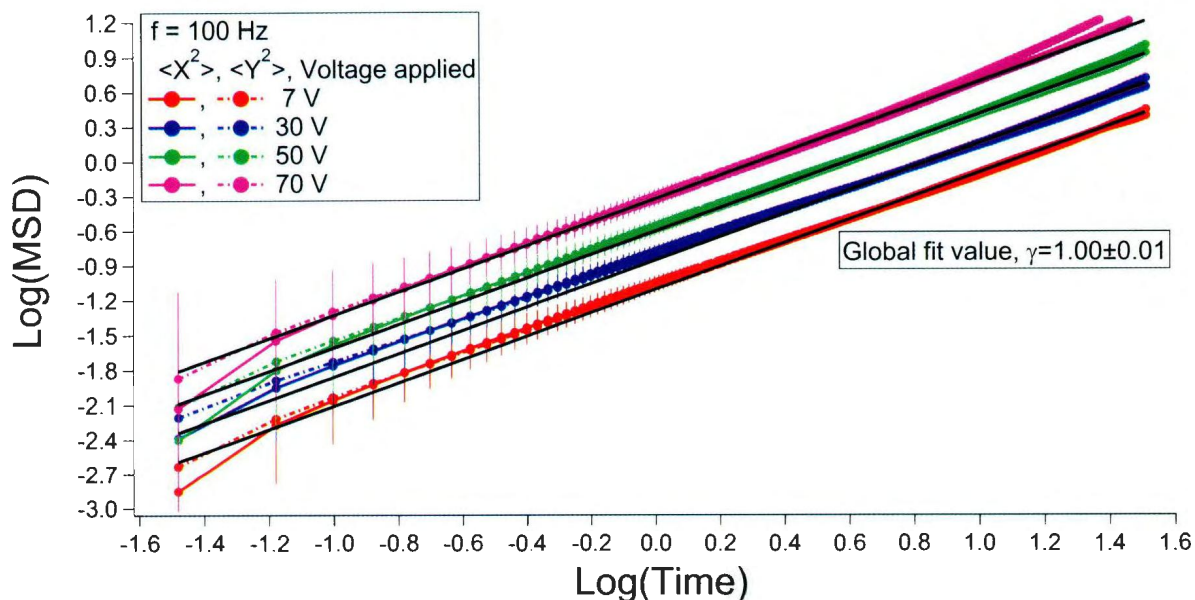
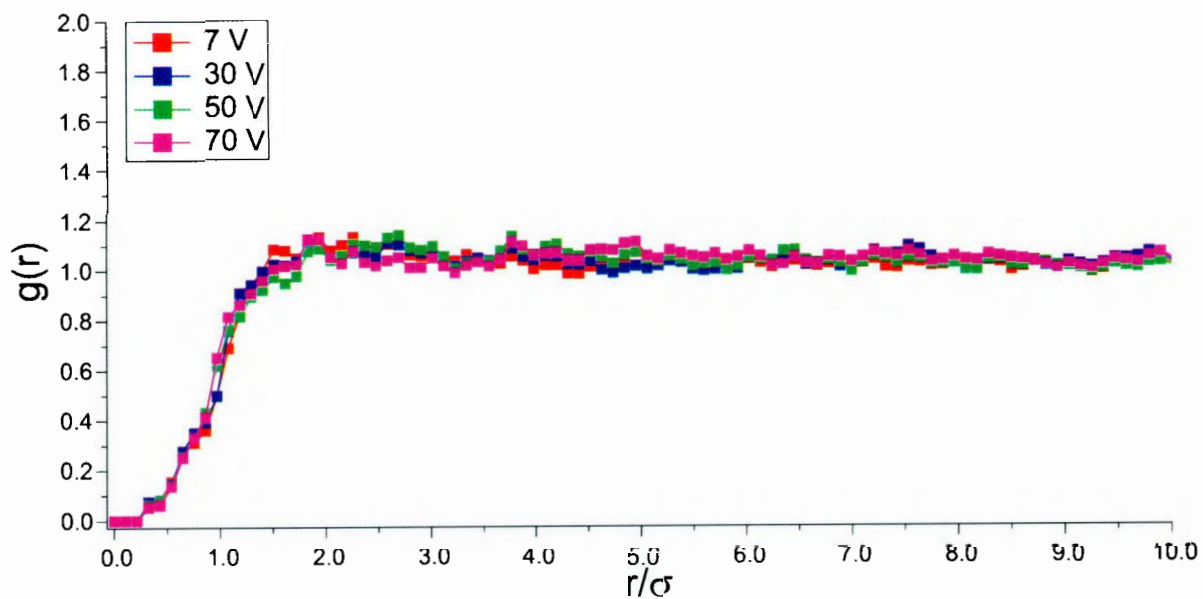
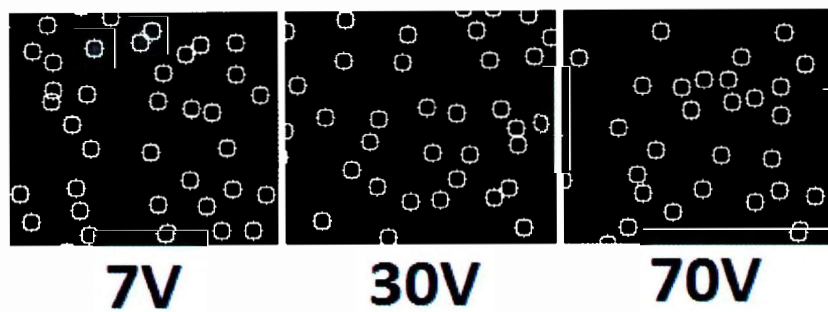


Figure 4.36: EH02, 100 Hz at electric fields ranging from 7 to 70 V/mm, shows simple diffusive behaviour both along and perpendicular to the field for all applied voltages.



(a)



(b)

Figure 4.37: (a) EH02, 100 Hz at electric fields ranging from 7 to 70 V/mm. Pair correlation function shows no peak, indicating no structuring of colloids. (b) EH02, $f = 100\text{Hz}$. Montage of area from single frames of tracked data at 7V, 30V and 70V. Shows no chainlike structures even at the highest fields.

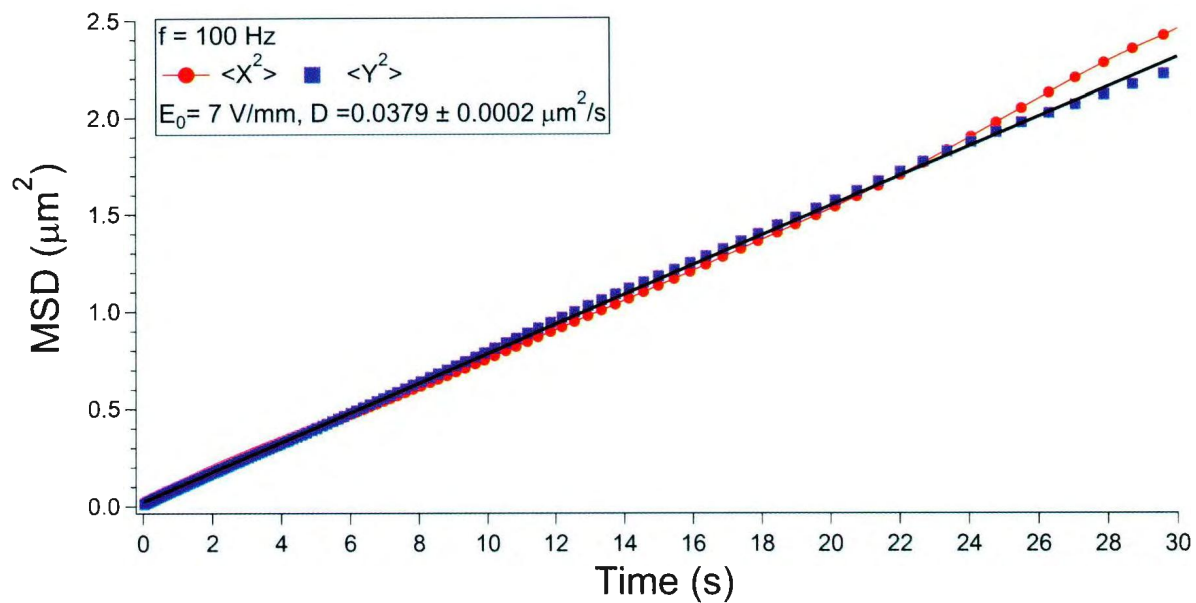


Figure 4.38: EH02, $f = 100\text{Hz}$ with 7V/mm . $\langle Y^2 \rangle$ versus time is linear, and yields an experimental diffusion coefficient of $D_{100\text{Hz}}^{EH02} = 0.038 \pm 0.0002\mu\text{m}^2/\text{s}$.

Chapter 5

Discussion and Conclusions

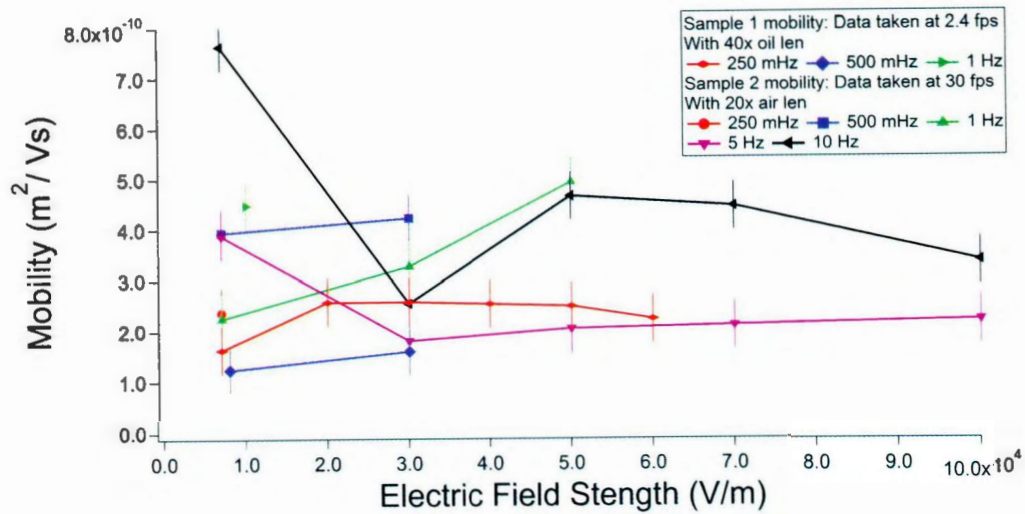
5.1 Introduction

This chapter will discuss the results that were outlined in chapter 4. This will include discussion of normal, sub-, super- diffusion behaviour, as well as an example of each type of diffusion behaviour that was seen. After that there will be a phase diagram to highlight the different behaviour, and the transition from each phase to the next. Finally at the end there will be a conclusion of the work done within this thesis as well as future work ideas.

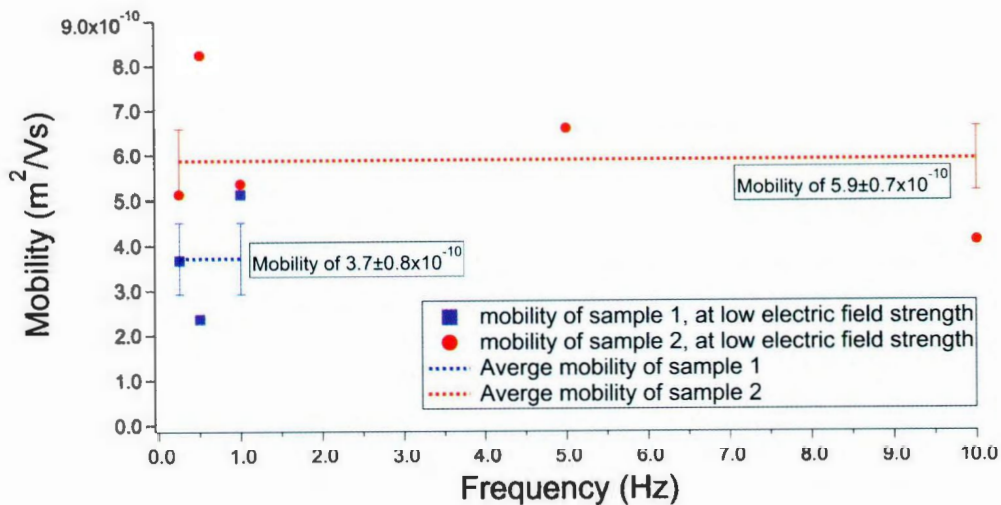
5.2 Electrophoretic Mobility

The particles respond to the electric field E by electrophoretic motion with a speed u . By measuring particle motions, we can extract the electrophoretic mobility μ_E using the equation $u = \mu_E E$ at different frequencies and field amplitudes. This is shown in figure 5.1(a). Given the noise in the data, there is no obvious trend for the

electrophoretic mobility as a function of field strength. The small-amplitude response (at low voltage) is shown in figure 5.1(b) as a function of frequency. Here too, there is no clear trend of any dependence on frequency. The average value of electrophoretic mobilities are $3.7 \pm 0.1 \times 10^{-10} \text{m}^2/\text{Vs}$ (sample EH01) and $5.9 \pm 0.1 \times 10^{-10} \text{m}^2/\text{Vs}$ (sample EH02). This may be compared with the range 4.0×10^{-10} to $6.0 \times 10^{-10} \text{m}^2/\text{Vs}$ obtained by Vissers et al in a similar system [1]. For all of the different voltages at all the different frequencies the electrophoresis mobilities were calculated to see if there was a pattern. From figure 5.1(a) and figure 5.1(b) it is clear that there is no pattern to the electrophoresis mobility. But the mobilities that were found within this thesis due compare well with previous reported mobilities from Vissers et al [1].



(a)



(b)

Figure 5.1: (a) Electrophoretic mobility for samples EH01 and EH02 for a range of frequencies ranging from 250mHz to 100 Hz. (b) The small-amplitude electrophoretic response (shown for samples EH01 and EH02) showed no strong trend as a function of frequency. The average values reported are $3.7 \pm 0.1 \times 10^{-10} m^2/Vs$ and $5.9 \pm 0.1 \times 10^{-10} m^2/Vs$ respectively and compare with values ranging from 4.0×10^{-10} to $6.0 \times 10^{-10} m^2/Vs$ reported previously in a similar system [1].

5.3 Pair correlation functions at zero field for Samples EH01 and EH02

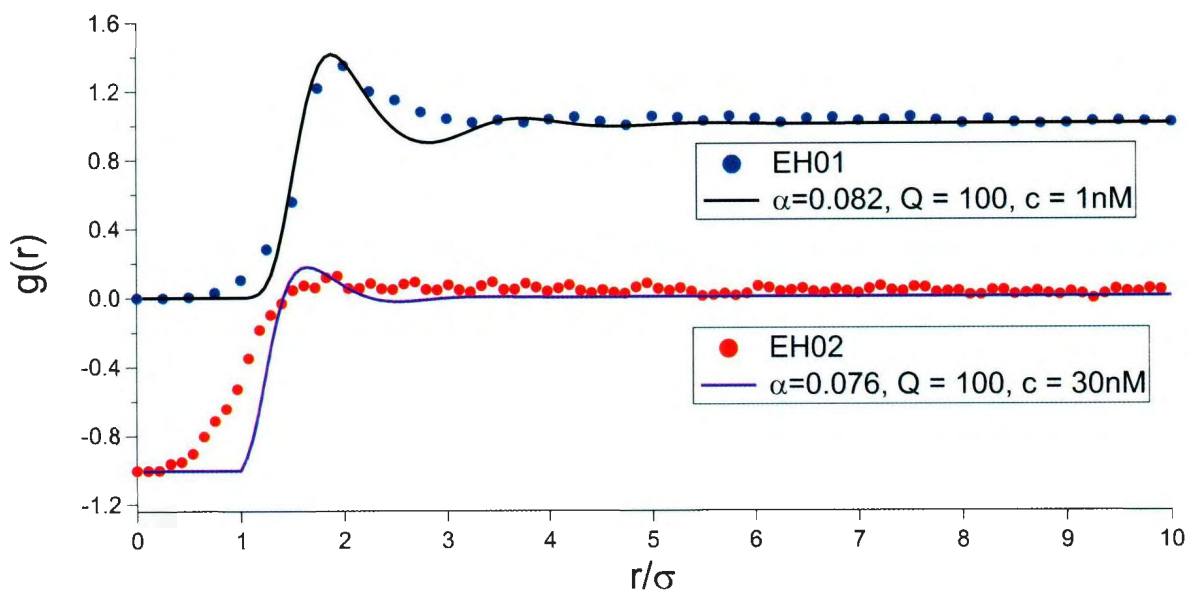
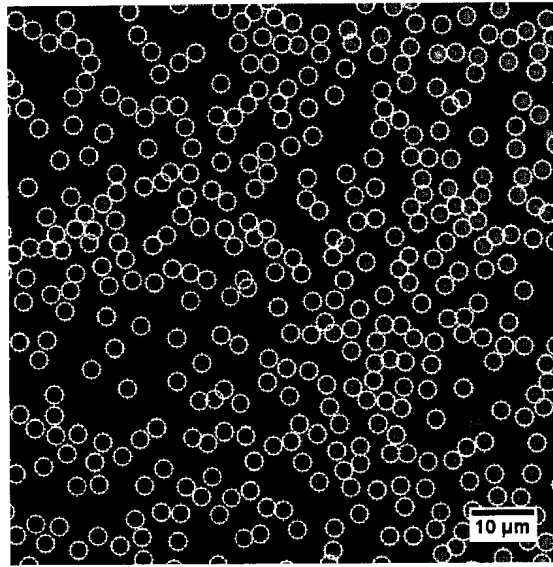
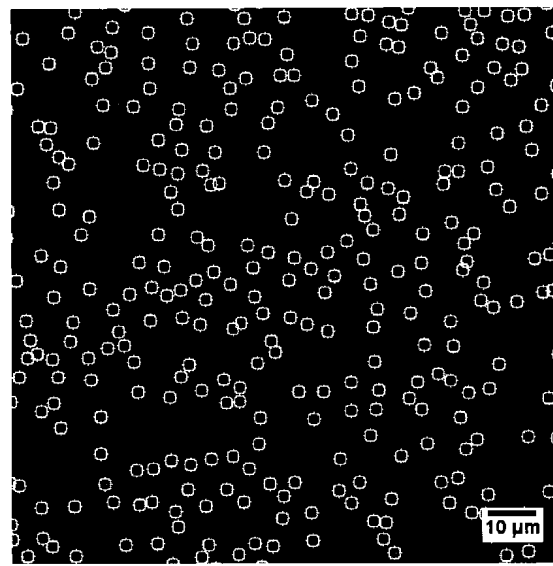


Figure 5.2: Shown are 2D pair correlation functions corresponding to samples EH01 and EH02 (circle and square symbols, respectively, data for EH02 is shifted down by 1 unit for clarity) along with calculated pair correlations for the shown values of ionic concentration (c), particle charge (Q), and particle (area) fraction ϕ .

The pair correlation functions at zero field was used to get an better idea on the differences in ion concentration between samples EH01 and EH02. Previous work ([36]) has shown that the typical values of charge per particle are in the range of $Q=100-200$, while typical ionic concentrations can be as low as the nanomolar range with Debye lengths up to the micron range. The Bjerrum length for our solvent mixture is $103 \pm 10\% \text{ \AA}$.



(a)



(b)

Figure 5.3: (a) Sample EH01 image. Particle area fractions of $\alpha = 0.082$. (b) Sample EH02 image. Particle area fractions of $\alpha = 0.076$.

At such small ion concentrations, it is easy to get sample-to-sample variability of the Debye length. Typical methods to control the Debye length (using surfactant-like salts such as tetrabutylammonium chloride [37]) can result in other complications, and are thus avoided in this study.

We can get a rough idea of ion concentrations by comparing the pair correlation functions to ones calculated for representative values of ionic concentration (1 nM) and particle charge ($Q=100$) for the experimentally determined particle area fractions but with different ionic concentrations ($\alpha = 0.082$ and $c = 1$ nM for EH01 and $\alpha = 0.076$ and $c = 30$ nM for EH02). Note that since the calculated pair correlation functions are for 3 dimensions, these are not true fits but just guides. It is reasonable to suggest that the difference in interparticle correlations that are seen in the dynamics arise simply from differences in ion concentrations: given such low ion concentrations, these differences are easier to monitor (via pair correlations) than to control.

5.4 Dynamical Phase Diagram

Figure 5.4 shows a phase diagram for the diffusion behaviour at different frequency at different electric field strength, showing the interplay between dipolar interactions and electrophoretic forces. Region I (inside the blue box) refers to normal diffusion (N). Region II (inside the red box) refers to normal diffusion at short times which changes to super diffusion at long time (N-Super). Region III (inside the purple box) refers to sub diffusion at short times which changes to super diffusion at long time (Sub-Super) along X. Region IV (inside the black box) refers to sub diffusion (Sub). Region V (inside the orange box) refers to normal diffusion along Y and sub diffusion

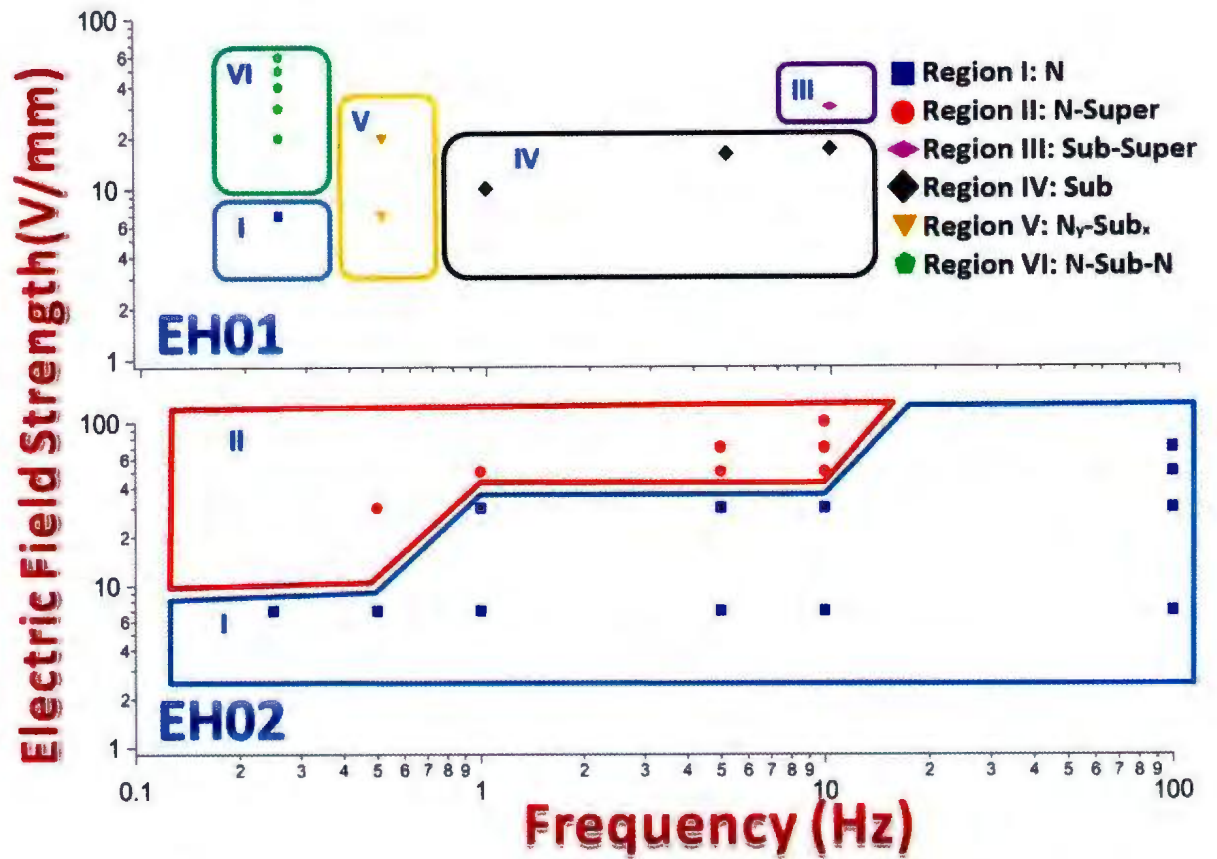


Figure 5.4: Dynamical Phase Diagram for samples EH01 and EH02. This diagram shows normal diffusive behaviour at low field strengths for all frequencies and also at high frequencies for all field strengths studied. A range of anomalous diffusive behaviours are observed in the low frequency regime but at higher field strengths.

along X (N_y, sub_x). And finally Region VI refers to the diffusion switching from normal to sub and back to normal.

5.4.1 Region I: Normal Diffusion

Normal diffusion behaviour happens when $\text{MSD} \sim t^\gamma$ with $\gamma = 1$. This typically happens at zero field and also can occur for fields where thermal energy dominates over the other external forces (see section 4.6.6 at low field strength). This can also happen when the applied external force changes at a rate faster than what the particles can respond at, if the field does not result in larger scale structures. Figure 5.5 shows a montage of 5 frames about 0.8 seconds apart of a small region of tracked data. The red circles highlight particles undergoing normal diffusion behaviour due to Brownian motion.

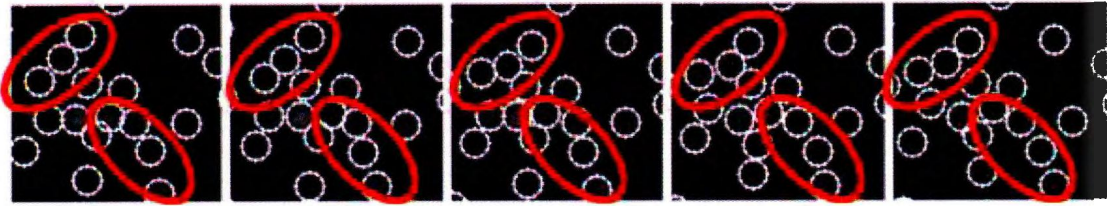


Figure 5.5: Montage of 5 frames about 0.8 seconds apart of a small region of tracked data of sample EH01. The red ellipses highlight particles undergoing normal diffusion behaviour due to Brownian motion.

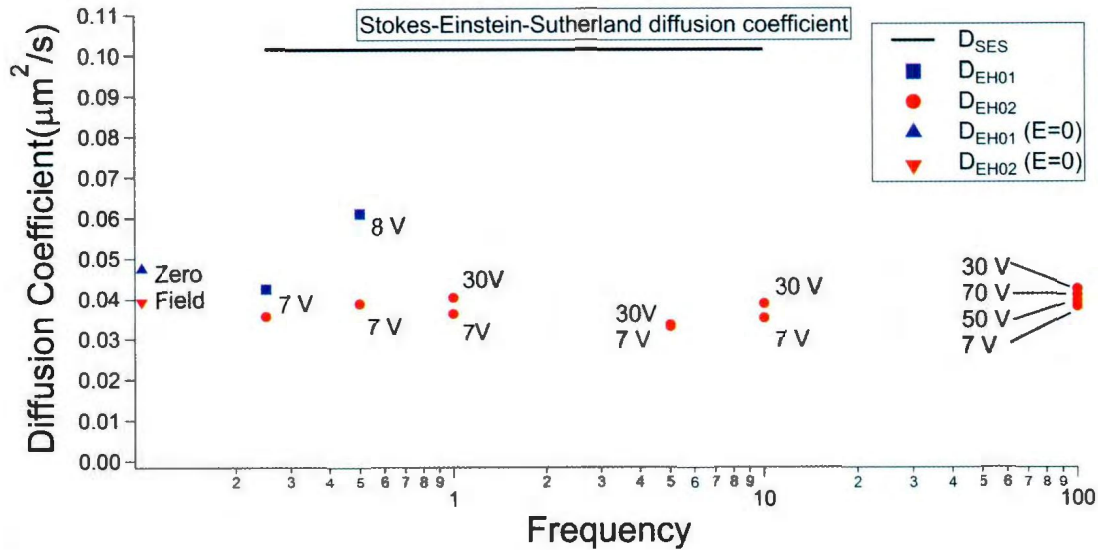


Figure 5.6: Plot of the diffusion coefficient for Stokes-Einstein-Sutherland (black line), EH01 (blue squares), and EH02 (red circles)

5.4.1.1 Stokes-Einstein-Sutherland Diffusion

In section 4.3 the diffusion coefficient was worked out to be $D = 0.102\mu\text{m}^2/\text{s}$ but both the diffusion coefficient for EH01 and EH02 differ from this value. The reason for this is primarily hydrodynamic interactions with the substrate. Using Faxén's law, (equation 2.16) we can estimate the surface-to-surface distance of the particles from the wall at zero field to be $0.113 \mu\text{m}$ and $0.006 \mu\text{m}$ for samples EH01 and EH02 respectively.

An interesting point that we note is that the lowest field diffusion coefficient is systematically lower than the ones at higher fields. This could also arise from the system being more two-dimensional at higher electric fields due to increased particle interactions. The projection of quasi two-dimensional sediment onto a 2-dimensional image has the effect of producing some apparent distances that are shorter than the

true distances. This was noted in section 4.5.2.

5.4.2 Region II: Transition from Normal to Super-Diffusion

In sample EH02, at high fields (ranging from 30 V/mm to 100V/mm) and in the frequency range 500 mHz to 10 Hz, we can see loose, flexible chainlike structures (shown in Figure 5.7). Individual colloidal particles appear free to diffuse at short times, but at long times we see slow reorganization of these chains. It is likely this directed motion of chains (i.e. chains being attracted by nearby chains and reconfiguring the structure) that manifests itself as super-diffusive behaviour (see also figure 4.30) at long times. A good example of this type of behaviour is shown in figure 5.7 which is a montage of 3 frames 10 seconds apart, of a small region of tracked data (sample EH02, $f= 5\text{Hz}$, $E_0=30\text{ V/mm}$). The red circles highlight particles undergoing this chain reconfiguration at long times.

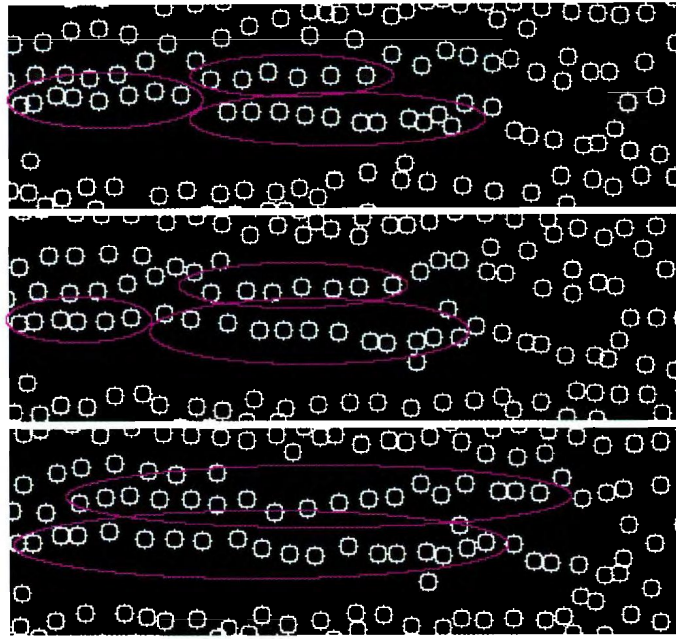


Figure 5.7: Montage of 3 frames 10 seconds apart, of a small region of tracked data of sample EH02 at 5Hz, 70 V/mm. The purple circles highlight chains that are breaking and forming new chains.

5.4.3 Region III: Transition from Sub-Diffusive to Super-Diffusive Behaviour

At high field strength ($\sim 30\text{V/mm}$) and intermediate frequency ($\sim 10\text{Hz}$) colloidal particles have form chains. The particles within these chains are restricted to maintain the chains, thus exhibit sub-diffusive behaviour (with $\gamma < 1$). As compared to region II, where the short-time behaviour is diffusive, the chains (see figure 5.7) are much stiffer and the particles are seen to be restricted by the chain structure more. This is the likely reason for the sub-diffusive behaviour at short times (figure 4.14)

The super-diffusive behaviour at long times has the same origin as in region II, and seems to correlate with the chains reorganizing themselves. A good example of this is when colloidal chains have formed at 10 Hz with 30 V/mm applied to sample EH02 (figure 4.14) and these chains diffuse into each other. Figure 5.8 shows a montage of 5 frames at about 1 second of a small region of tracked data. The red circles highlight tracked particles in a chain that attaches to another chain.

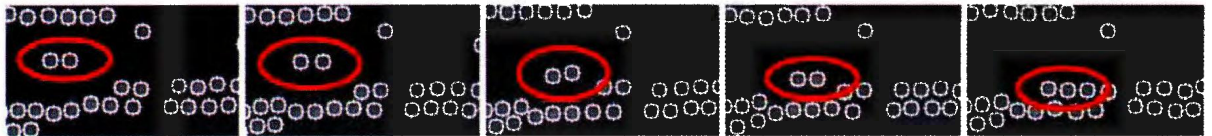


Figure 5.8: Montage of 5 frames at 1 second apart, of a small region of tracked data of sample EH01 at 10Hz, 30 V/mm. The red circles highlight tracked particles in a chain that attaches to another chain.

5.4.4 Region IV: Sub-Diffusive Behaviour

Sub-diffusive behaviour is observed (figure 4.10. or figure 4.12) when the motion of colloidal particles are restricted to within chains for the duration of the observations. The chains themselves seem to have formed (figure 5.9) a large laterally extended cluster, so there is no transition to normal diffusion of chains, which might be expected for particles in an isolated chain at long times. A good example of this is when colloidal chains are starting to form at 5 Hz with 16 V/mm applied (sample EH01). Figure 5.9 shows a montage of 5 frames at .4 seconds apart, of a small region of tracked data of sample EH01 at 5Hz, 16 V/mm, highlighting particles within chains.

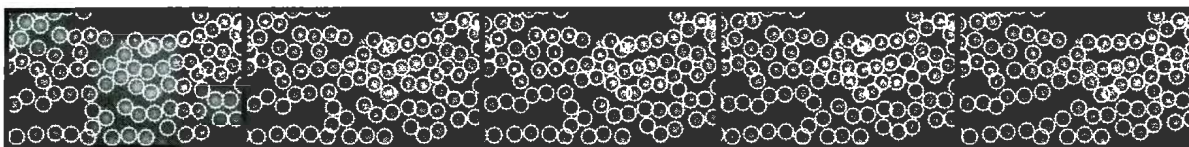


Figure 5.9: Montage of 5 frames at .4 seconds apart, of a small region of tracked data of sample EH01 at 5Hz, 16 V/mm, highlighting particles within chains.

5.4.5 Region V: Anisotropic normal and sub-diffusive behaviours

In Region V, we observe that the dynamics perpendicular to the field direction (Y) is diffusive, while the dynamics along the field direction is sub-diffusive with $\gamma = 0.8$. For example, when 500 mHz was applied with a field strength of $E_0 = 8$ V/mm, what we saw was very weak particle alignment along the field direction (see figure 4.8(b), top image). Thus particles execute normal diffusion at short times since the alignment

was weak, but at long times, the particles are more likely to be obstructed along the field direction.

5.4.6 Region VI: Sub-Diffusive Behaviour at Intermediate Times.

In sample EH01, when 250 mHz was applied what appears to happen along the non-applied direction is switching from normal diffusive to sub-diffusive to normal diffusive behaviour for all field strength. Even at the largest fields where there is clear chain formation, the chains appear to be undulating and not rigid. Thus, at short times colloids are free to diffuse. In addition there is, of course, a short time oscillatory motion along the field direction. At intermediate times the presence of chain structures restricts motion along X and Y. We see this clearly in the slopes of the $\log(\langle Y^2 \rangle)$ vs $\log(\text{time})$ in figure 4.4. At long times, the chains themselves can diffuse, and there is not much chain-chain association. This gives rise to diffusion again at long times.

5.5 Conclusion

In this thesis we see regimes of normal diffusion, as well as regimes where one observes both restricted and enhanced motions, which has been seen in other colloidal systems. Reduced particle motions are normally accompanied by cooperative motion all directions [24]. This type of motion has also been seen in glass-forming systems (Chaudhuri et al [24]). Enhanced mobility on the other hand, is seen in systems with anisotropy, e.g. rod-like colloidal systems (Höfling et al [28]) and self-propelled

bacteria (Golestanian et al [38]).

Also in this thesis, we have measured the response of charged colloids to electric fields at a wide range of frequencies and amplitudes. We see that there was no obvious trend for the electrophoretic mobility as a function of field strength nor for the small-amplitude response electrophoretic mobility as a function of frequency. But the electrophoretic mobilities found within this thesis compare well with ones obtained by Vissers et al in a similar system [1].

Our results are summarized in a dynamical phase diagram where both dipolar forces and time-dependent electrophoretic forces on the colloidal particles. As the frequency goes from low to high the force acting on the colloidal particles goes from dipolar interactions to electrophoretic force.

At the highest frequency that was probed, there is very little effect of the field on the colloidal particles. This is understandable as the amplitudes of the field were small (less than 100 V/mm). Previous experiments have shown that one needs fields on the order of ~ 1000 V/mm for (dielectric) dipolar forces to be important. This implies that even the dipolar forces induced here are driven by ionic (not dielectric) polarization, i.e. deformation of the double layer around the colloids.

At the lowest electric field strength, motions along X and Y (parallel and perpendicular to the electric field) seem to be uncoupled from each other. But as the electric field strength increases, X and Y motions are more coupled. This transition from normal to sub-diffusive behaviour and the subsequent normal diffusion at long times has been seen in molecular dynamics simulations of Joranovich et al [23]. This behaviour is seen qualitatively along x (the field direction) and along y, but is easier to detect along y, because there is no oscillatory motion. The complex dynamics along y indi-

cates that there is coupling between the driving force (along x) and the response along y . Additionally as the electric field strength increases, the hydrodynamic force and electrophoretic force increase as well and we start to see “collective” dynamics of the colloidal particles and chain motion which results in different anomalous behaviours.

5.6 Future Work

Our main intention for future work is to try to get a clearer picture of the different phase that were observed in the phase diagram and to reproduce the results already found with in this thesis. Additionally, the role of the third dimension is not clear, and it would be useful to make the system more two-dimensional than what was studied with this thesis. This could be achieved by introducing a laser light pressure which would force the colloidal closer to one of the walls [39]. Another possibility would be to density match the system and carry out a fully 3-dimensional of frequency-dependent electric-field driven colloidal dynamics.

Bibliography

- [1] Teun Vissers, Arnout Imhof, Félix Carrique, Ángel V. Delgado, and Alfons van Blaaderen. Electrophoresis of concentrated colloidal dispersions in low-polar solvents. *Journal of Colloid and Interface Science*, 361(2):443 – 455, 2011.
- [2] Heiko Schmidle, Sebastian Jäger, Carol K. Hall, Orlin D. Velev, and Sabine H. L. Klapp. Two-dimensional colloidal networks induced by a uni-axial external field. *Soft Matter*, 9(8):2518–2524, 2013.
- [3] Gary L Hunter and Eric R Weeks. The physics of the colloidal glass transition. *Reports on Progress in Physics*, 75(6):066501, 2012.
- [4] Wilson Poon. Colloids as big atoms. *Science*, 304(5672):830–831, 2004.
- [5] İ.İnanç Tarhan and George H. Watson. Photonic band structure of fcc colloidal crystals. *Physical Review Letters*, 76(2):315–318, 1996.
- [6] Alice P. Gast and Charles F. Zukoski. Electrorheological fluids as colloidal suspensions. *Advances in Colloid and Interface Science*, 30(0):153–202, 1989.

- [7] Anna Stradner, Helen Sedgwick, Frederic Cardinaux, Wilson C. K. Poon, Stefan U. Egelhaaf, and Peter Schurtenberger. Equilibrium cluster formation in concentrated protein solutions and colloids. *Nature*, 432(7016):492–495, 2004.
- [8] Stefan Odenbach. *Colloidal Magnetic Fluids: Basics, Development and Application of Ferrofluids*. Springer, Berlin Heidelberg, lecture notes in physics volume 763, first edition, 2009.
- [9] Robert J. Hunter. *Foundations of Colloid Science*. Oxford University Press Inc., second edition, 2001.
- [10] James E. Martin, Judy Odinek, and Thomas C. Halsey. Evolution of structure in a quiescent electrorheological fluid. *Physical Review Letters*, 69(10):1524–1527, 1992.
- [11] V. Prasad, D. Semwogerere, and Eric R. Weeks. Confocal microscopy of colloids. *Journal of Physics: Condensed Matter*, 19(113102):1–25, 2007.
- [12] Gilles Bosma, Chellapah Pathmamanoharan, Els H. A. de Hoog, Willem K. Kegel, Alfons van Blaaderen, and Henk N. W. Lekkerkerker. Preparation of monodisperse, fluorescent PMMA Latex colloids by dispersion polymerization. *Journal of Colloid and Interface Science*, 245(2):292–300, 2002.
- [13] Alfons van Blaaderen and A. Vrij. Synthesis and characterization of monodisperse colloidal organo-silica spheres. *Journal of Colloid and Interface Science*, 156(1):1–18, 1993.

- [14] William B. Russel, Dudley A. Saville, and William R. Schowalter. *Colloidal Dispersions*. Cambridge University Press, first edition, 1989.
- [15] Richard A. L. Jones. *Soft Condensed Matter*. Oxford University Press, first edition, 2002.
- [16] Robert Brown. A brief account of microscopical observations. *The miscellaneous botanical works of Robert Brown.*, Volume 1:466–486, 1827.
- [17] A. Einstein, M.J. Klein, J.J. Stachel, and R. Schulmann. *The Collected Papers of Albert Einstein: The Swiss Years - Correspondence, 1902-1914*. The collected papers of Albert Einstein. Princeton University Press, 1993.
- [18] William Sutherland. A dynamical theory of diffusion for non-electrolytes and the molecular mass of albumin. *Philosophical Magazine*, 9(0):781–785, 1905.
- [19] Todd M. Squires and Thomas G. Mason. Fluid mechanics of microrheology. *Annual Review of Fluid Mechanics*, 42(1):413–438, 2010.
- [20] Brian Kirby. *Micro- and Nanoscale Fluid Mechanics*. Cambridge University Press., first edition, 2013.
- [21] Mirjam Leunissen. *Manipulating Colloids with Charges and Electric Fields*. Utrecht University, first edition, 2007.
- [22] Thomas A. Witten with Philip A. Pincus. *Structured Fluids, Polymers, colloids, surfactants*. Oxford University Press, first edition, 2004.

- [23] Jelena Jordanovic, Sebastian Jäger, and Sabine H. L. Klapp. Crossover from normal to anomalous diffusion in systems of field-aligned dipolar particles. *Physical Review Letters*, 106(3):038301, 2011.
- [24] Pinaki Chaudhuri, Ludovic Berthier, and Walter Kob. Universal nature of particle displacements close to glass and jamming transitions. *Physical Review Letters*, 99(6):060604, 2007.
- [25] H Löwen. Colloidal soft matter under external control. *Journal of Physics: Condensed Matter*, 13(24):R415, 2001.
- [26] Anand Yethiraj. Tunable colloids: control of colloidal phase transitions with tunable interactions. *Soft Matter*, 3(9):1099-1115, 2007.
- [27] Seth Fraden, Alan J. Hurd, and Robert B. Meyer. Electric-field-induced association of colloidal particles. *Physical Review Letters*, 63(21):2373–2376, 1989.
- [28] Felix Höfling, Erwin Frey, and Thomas Franosch. Enhanced diffusion of a needle in a planar array of point obstacles. *Physical Review Letters*, 101(12):120605, 2008.
- [29] Sebastian Jäger, Heiko Schmidle, and Sabine H. L. Klapp. Nonequilibrium condensation and coarsening of field-driven dipolar colloids. *Physical Review E*, 86(1):011402, 2012.
- [30] James E. Martin, Eugene Venturini, Judy Odinek, and Robert A. Anderson. Anisotropic magnetism in field-structured composites. *Physical Review E*, 61(3):2818–2830, 2000.

- [31] Prerna Sharma, Shankar Ghosh, and S. Bhattacharya. A high-precision study of hindered diffusion near a wall. *Applied Physics Letters*, 97(10):104101, 2010.
- [32] V. Adrian Parsegian. *Van der Waals Forces: A handbook for biologists, chemists, engineers, and physicists*. Cambridge University Press., first edition, 2006.
- [33] Sébastien Wiederseiner, Nicolas Andreini, Gaël Epely-Chauvin, and Christophe Ancy. Refractive-index and density matching in concentrated particle suspensions: a review. *Experiments in Fluids*, 50(5):1183–1206, 2011.
- [34] John C. Crocker and David G. Grier. Methods of digital video microscopy for colloidal studies. *Journal of Colloid and Interface Science*, 179(1):298–310, 1996.
- [35] John C. Crocker and Eric R. Weeks. *Particle tracking using IDL*. <http://www.physics.emory.edu/weeks/idl/>, 2008.
- [36] C. P. Royall, R. van Roij, and Alfons van Blaaderen. Extended sedimentation profiles in charged colloids: the gravitational length, entropy, and electrostatics. *Journal of Physics: Condensed Matter*, 17(15):2315, 2005.
- [37] Anand Yethiraj and Alfons van Blaaderen. A colloidal model system with an interaction tunable from hard sphere to soft and dipolar. *Nature*, 421(6922):513–517, 2003.
- [38] Ramin Golestanian. Anomalous Diffusion of Symmetric and Asymmetric Active Colloids. *Physical Review Letters*, 102(18):188305, 2009.

- [39] Cecile Dalle-Ferrier, Matthias Kruger, Richard D. L. Hanes, Stefan Walta, Matthew C. Jenkins, and Stefan U. Egelhaaf. Dynamics of dilute colloidal suspensions in modulated potentials. *Soft Matter*, 7(5):2064–2075, 2011.

Appendix A

Image Orientation Corrections

Since the results of this work was based on experiments with an applied uniaxial electric field, then there is a chance that the horizontal plane of the image may not be exactly along the x direction. To test to see if this is the case, one of the experiment data sets was used. For each experiment, an image orientation correction was applied using the following procedure.

This experiment data set was then artificially rotated for a series of degrees to compare the MSD data with the non-rotated data. In figure A.1 a sample schematic of this angle measurement is shown. The blue line shows the original position, and the red line shows the rotated position from the original position by the angle ϕ . Equation A.1 shows the rotation equation for this, where (x', y') is parts of the rotated position, and (x, y) is parts of the original position.

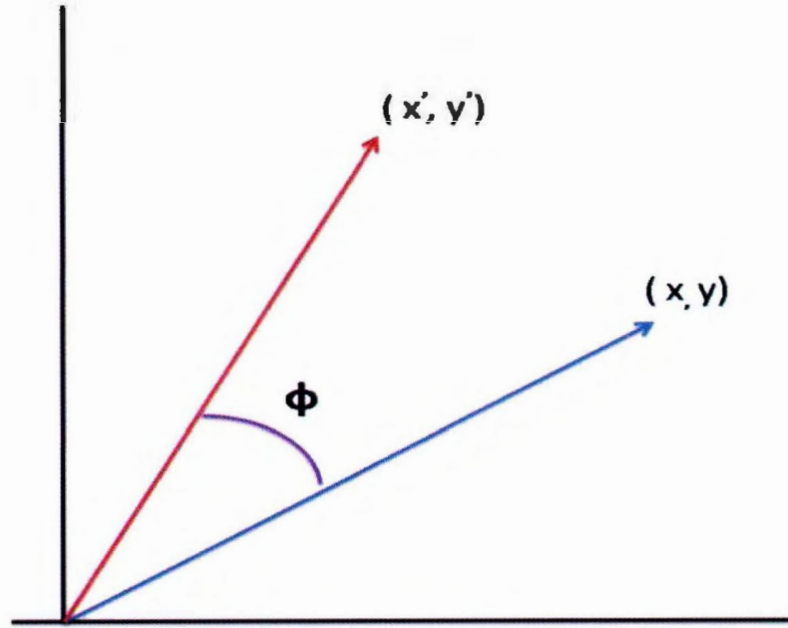


Figure A.1: Samples figure for the rotation angle problem.

$$\begin{pmatrix} x' \\ y' \end{pmatrix} = \begin{pmatrix} \cos(\phi) & -\sin(\phi) \\ \sin(\phi) & \cos(\phi) \end{pmatrix} \begin{pmatrix} x \\ y \end{pmatrix} \quad (\text{A.1})$$

Now adding in a time dependence to the positions and subtracting out the first position to equation A.1:

$$\begin{pmatrix} x'(t) - x'(0) \\ y'(t) - y'(0) \end{pmatrix} = \begin{pmatrix} \cos(\phi) & -\sin(\phi) \\ \sin(\phi) & \cos(\phi) \end{pmatrix} \begin{pmatrix} x(t) - x(0) \\ y(t) - y(0) \end{pmatrix} \quad (\text{A.2})$$

Now setting $\Delta x' = x'(t) - x'(0)$, $\Delta x = x(t) - x(0)$, $\Delta y' = y'(t) - y'(0)$, $\Delta y = y(t) - y(0)$ and solving out equation A.2 get:

$$\begin{pmatrix} \Delta x' \\ \Delta y' \end{pmatrix} = \begin{pmatrix} \cos(\phi)\Delta x & -\sin(\phi)\Delta y \\ \sin(\phi)\Delta x & \cos(\phi)\Delta y \end{pmatrix} \quad (\text{A.3})$$

Now squaring, and choosing the $t=0$ value as $(0,0)$ for equation A.3 we get:

$$\begin{aligned} (x')^2 &= x^2 \cos^2(\phi) + y^2 \sin^2(\phi) - 2y^2 x^2 (\sin(\phi) \cos(\phi)) \\ (y')^2 &= y^2 \cos^2(\phi) + x^2 \sin^2(\phi) + 2y^2 x^2 (\sin(\phi) \cos(\phi)) \end{aligned} \quad (\text{A.4})$$

Now if we take the average for equation A.4, we get:

$$\begin{aligned} \langle (x')^2 \rangle &= \langle x^2 \rangle \cos^2(\phi) + \langle y^2 \rangle \sin^2(\phi) - 2 \langle y^2 x^2 \rangle (\sin(\phi) \cos(\phi)) \\ \langle (y')^2 \rangle &= \langle y^2 \rangle \cos^2(\phi) + \langle x^2 \rangle \sin^2(\phi) + 2 \langle y^2 x^2 \rangle (\sin(\phi) \cos(\phi)) \end{aligned} \quad (\text{A.5})$$

Now if we assumed that $\langle y^2 x^2 \rangle = 0$ (value was found to be $\sim 2.0 \times 10^{-5}$) in equation A.5, then:

$$\begin{aligned} \langle (x')^2 \rangle &= \langle x^2 \rangle * \cos^2(\phi) + \langle y^2 \rangle * \sin^2(\phi) \\ \langle (y')^2 \rangle &= \langle y^2 \rangle * \cos^2(\phi) + \langle x^2 \rangle * \sin^2(\phi) \end{aligned} \quad (\text{A.6})$$

Now if we add these two equations we get:

$$\begin{aligned} \langle (x')^2 \rangle + \langle (y')^2 \rangle &= \langle x^2 \rangle (\cos^2(\phi) + \sin^2(\phi)) + \langle y^2 \rangle (\cos^2(\phi) + \sin^2(\phi)) \\ &= \langle x^2 \rangle + \langle y^2 \rangle \quad (\text{Independent of } \phi) \end{aligned} \quad (\text{A.7})$$

Clearly from equation A.7 it can be seen that total MSD value ($\langle (x')^2 \rangle + \langle (y')^2 \rangle$) of the rotated data sets, at some ϕ , is independent of ϕ . We first used this to check that the invariant quantity in the rotated data is indeed invariant of ϕ . This can be seen in figure A.2, where all the data sets lie on top of the non-rotated data.

Now, directly from equation A.6 you can see that since the true directed motion is along $\langle (x')^2 \rangle$, then the rotation angle that minimizes $\langle (y')^2 \rangle$ will correspond to the correct orientation. This typically should happen at $\phi = 0$ if there is no misorientation. To find the angle at which will minimizes this, one rotates the frame of reference by some small angle (ϑ) till this minimum happens. Thus this ϑ is the angle that the data needs to be corrected by.

A.1 Results of Angle Measurements

In figure A.2 it can be seen that all rotated data lies on top of the original data set.

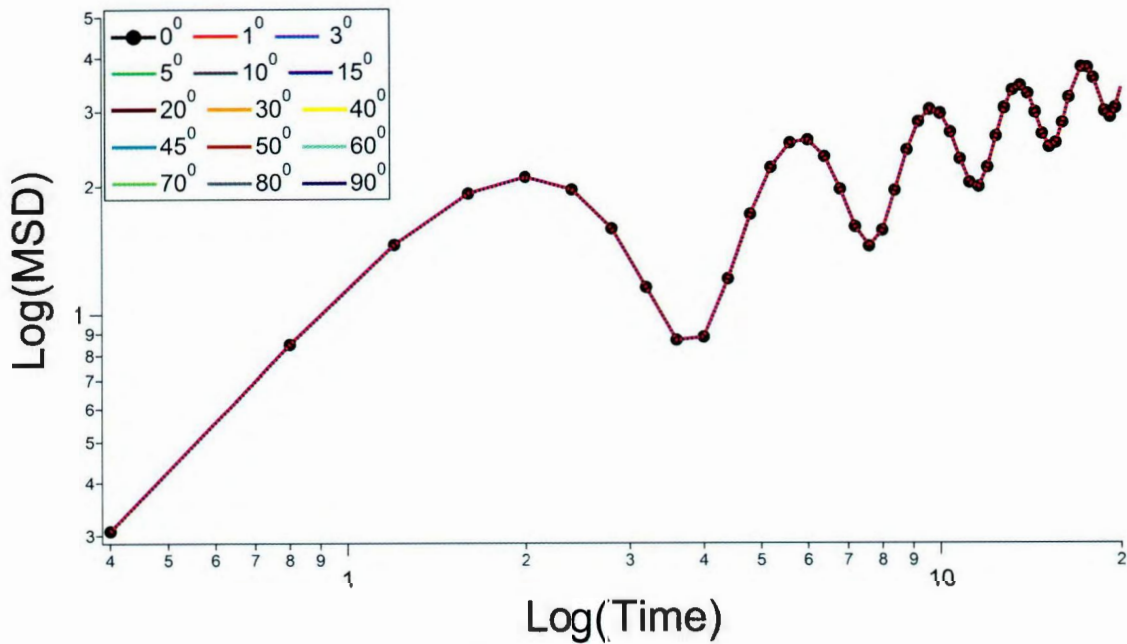


Figure A.2: Plot of $\log(\text{MSD})$ vs $\log(\text{time})$, where all the data sets lie on top of the non-rotated data.

In figure A.3(a) there is a plot of the $\text{Log}(\langle x^2 \rangle)$ versus $\text{Log}(\text{time})$ for the x component for a list of angle including both the positive (solid lines) and the negative (dash lines) rotation of that angle with the the insert as the blown up area of the black square. Similar for the y component in figure A.3(b). In figure A.3(a) as the angle increases the strength of $\langle x^2 \rangle$ decreases but the overall shape stay the same. Similar for figure A.3(b) as the angle increases the strength of $\langle y^2 \rangle$ increases while the overall shape stay the same.

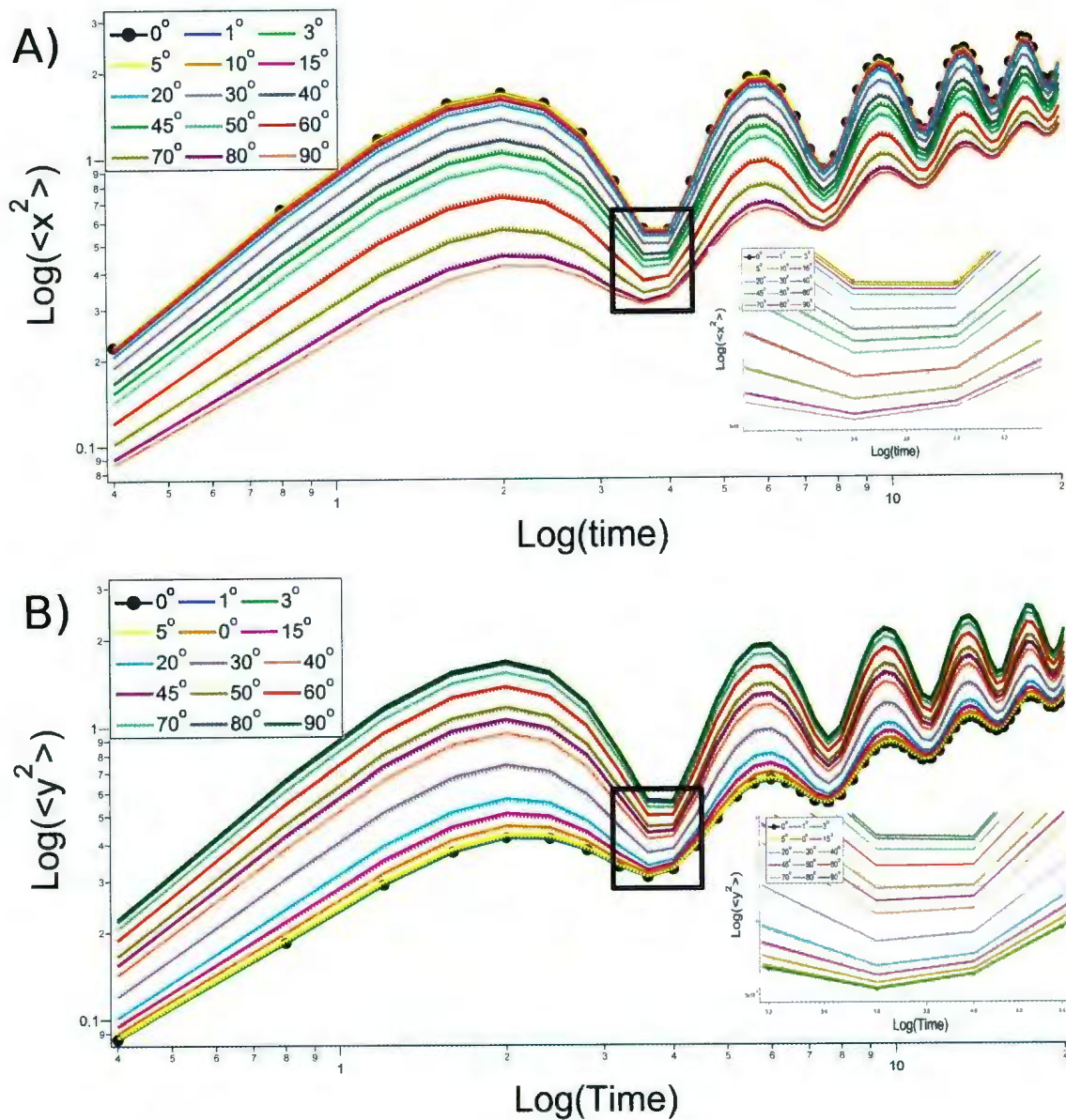


Figure A.3: In principle, the electric field (E) should be parallel to \hat{x} , but could be rotated by a small amount. A test to determine the true direction of the E , by a rotating the frame of reference. The data that was used was at a frequency of 250mHz at 20 voltages. The inserts in both (A),(B) are blown up areas of the black squares. The dotted lines corresponds to negative of the degrees. A) As the degree increases, MSD along x decreases. B) As the degree increases, MSD along y increases.



